ScuDo
Scuola di Dottorato ~ Doctoral School
WHAT YOU ARE, TAKES YOU FAR

Doctoral Dissertation
Doctoral Program in Electrical Engineering (31th Cycle)

ADVANCED CHARACTERIZATION AND THEORETICAL ASSESSMENT OF THE BROADBAND MAGNETIC LOSSES OF SOFT MAGNETIC MATERIALS

By

Hanyu Zhao

******

Supervisor(s):
Prof. Carlo Stefano Ragusa (Politecnico di Torino)
Prof. Youhua Wang (Hebei University of Technology)
Dr. Carlo Appino ((INRiM)Istituto Nazionale di Ricerca Metrologica)

Doctoral Examination Committee:
Prof. Xiaoming.liu , Referee, Tianjin Polytechnic University
Dr. Vincenzo.Cirimele , Referee, Politecnico di Torino
Prof. Aldo.Canova, Referee, Politecnico di Torino
Prof. Fengyi.Guo , Referee, Liaoning Technical University
Prof. Jingqin.Wang, Referee, Hebei University of Technology

Politecnico di Torino
2019

Declaration

I hereby declare that, the contents and organization of this dissertation constitute my own original work and does not compromise in any way the rights of third parties, including those relating to the security of personal data.

Hanyu Zhao

2019

I would like to dedicate this thesis to my loving parents and my husband for their support.

Acknowledgment

Nearly five years of Ph.D. study and research work is about to be completed. I am grateful for the growth that this experience has brought to me, and I am grateful to the teachers, classmates and supporters who helped me during this period.

First, thanks to my domestic tutor, Professor Youhua Wang, he had been very supportive of my willingness to study abroad from the beginning to the end. From master to doctor, it has been nearly six years, Professor Youhua Wang has repeatedly pointed out right direction for me and encouraged me. At the same time, Professor Youhua Wang's scientific research is rigorous and realistic, and the meticulous attitude guide me for life. Here I would like to express my sincere gratitude to him.

Thanks to my Co-supervisor, Professor Carlo Ragusa, I went to a foreign country to study abroad, the task is heavy, the support and companionship is not so much. But thanks to Professor Carlo Ragusa's encouragement, I can make mistakes, grow and progress. He is not only my mentor but also a friend, sincerely thanking him for his selfless care and help.

I am grateful to Dr Carlo Appino from the Italian National Metrology Institute(Istituto nazionale di ricerca metrologica). From him, I learned a lot of principles that should be followed and how to establish complete and

comprehensive experimental data. He is also a partner who spends almost every day in the lab with me. I am benefit from a lot of experiences with him.

Thanks to the scientist Dr Fausto Fiorillo, who is over 70 years old and still active in the front line of research. No matter when I have any problems, as long as Dr Fausto Fiorillo is in the laboratory, he will carefully help me and answer the questions I encountered in the experiments. It is my great honor to be able to learn from him. Sincerely thank you.

I would like to thank all the teachers and classmates of the research team.And thank Professor Yongjian Li for his help in the research of the subject. Thanks to Dr Chengcheng Liu, Dr Long Chen and Dr Mhamood Khan for their help.

Finally, I sincerely thank my parents and my husband for their support and encouragement.

Abstract

The efficient use of electrical energy is crucial for the industrial development worldwide and, in particular, for the emerging countries. Generation, transmission, and conversion of the electrical energy all require the use of soft magnetic cores. At the same time, a dramatic increase of the electrical and electronic applications in the car industry, including hybrid and electric cars, and trends towards the more electric aircraft are posing compelling requirements on the efficiency of the cores, be their used as nuclei in a variety of devices and drives or as stators/rotors in electrical motors. In order to design highly efficient components and machines, it is necessary to achieve excellent understanding of the magnetization process and good predicting capabilities of the behavior of the soft magnetic materials, with special attention devoted to the phenomenology of energy losses, under conventional and non-conventional excitation conditions.

This thesis lays a foundation for the analysis of the National Nature Science Foundation of China project. It provides systematic, physically based, and quantitative investigation of the broadband loss behavior of different types of soft magnetic materials, ranging from the conventional non-oriented Fe-Si sheets to nanocrystalline ribbons.

A few main innovative points can be highlighted:

(1) The definite demonstration, against recent criticism in the literature, of the general validity of the loss decomposition method formulated with the Statistical Theory of Losses (STL). It regards, in particular, the role of the classical loss and its formulation below the limit for the skin effect. Wide-band experimental characterizations on a variety of non-oriented silicon steel sheets and low carbon steels are fully and consistently described by the STL. This occurs, in particular, for high-induction values and near-squared hysteresis loops, a predictable condition for adopting the alternative Saturation Wave Model (SWM), which fails instead to account for the experiments

(2) The analysis of magnetic losses under nonconventional magnetic induction waveform, such as PWM, symmetric and asymmetric triangular wave, is performed over a broad range of frequencies. It is shown that, by generalized application of the Statistical Theory of Losses and the related concept of loss separation, an accurate prediction can be made starting from standard results obtained with sinusoidal induction. This is a quite unique and general feature of our approach, because the prediction is done by simple analytical physically based methods, in contrast with the persisting use of empirical numerical methods in the present-day literature. Non-oriented Fe-Si and Fe-Co sheets, nanocrystalline Finemet–type ribbons, and Mn-Zn ferrites have been investigated up to $f = 1$ MHz and duty cycles ranging between 0.5 and 0.1. The intrinsic shortcomings of the popular approach to loss calculation of inductive components in power electronics, based on the empirical Steinmetz equation and its numerous modified versions, are overcome by the here described method.

(3) The effect of cutting on magnetization curve and losses in non-oriented Fe-Si sheets is measured from DC and 400 Hz and assessed by a simple model, considering the evolution of the magnetic properties on the width of the cut strips (30 mm – 5 mm). The analysis shows that the normal magnetization curve and the quasi-static magnetic losses evolve with the width of the strip according to a

hyperbolic law. This permits one to predict, using minimum pre-emptive information, the evolution of curve and hysteresis loss from indefinitely wide to narrow fully degraded strip.

KEYWORDS: Soft Magnetic Material; Broadband Frequency analysis; Magnetic Characterization; Loss Separation; The Statistical Theory of Losses

.

Contents

List of Figures

List of Tables

Nomenclature

Acronyms / Abbreviations

B	Magnetic Flux Density
H	Magnetic Field
INRIM	Istituto nazionale di ricerca metrologica
LCS	Low Carbon Steel
e.m.f	Electromotive force
MO	Magnetic Objects
MSE	Modified Steinmetz Equation
SE	Steinmetz Equation
SST	Single Sheet Tester
STL	Statistical Theory of Loss
SWM	Saturation Wave Magnetization
SMC	Soft Magnetic Composite
VNA	Vector Network Analyzer

PWM	Pulse Width Modulation

Chapter 1

Introduction

The global climate change is proofed by global temperature rise, warming oceans, shrinking ice sheets, declining arctic sea ice and so on. But the most compelling evidence is the CO_2 level. As the data provided by NASA showed in Figure 1.1, the current warming trend is significance because most of it is extremely likely (greater than 95% probability) to be the result of human activity since the mid-20th century and proceeding at a rate that is unprecedented over decades to millennia [1]. And according to the International Energy Outlook 2016 [2], CO_2 emissions related to energy tends to increase from 32.3 billion Mt in 2012 to 35.6 billion Mt and is expected to reach 43.2 billion Mt in 2040. According to 2011 International Energy Agency [3] reports about 70% of electricity is produced from fossil fuels and almost 46% electrical energy is supplied to electrical motors driven systems.

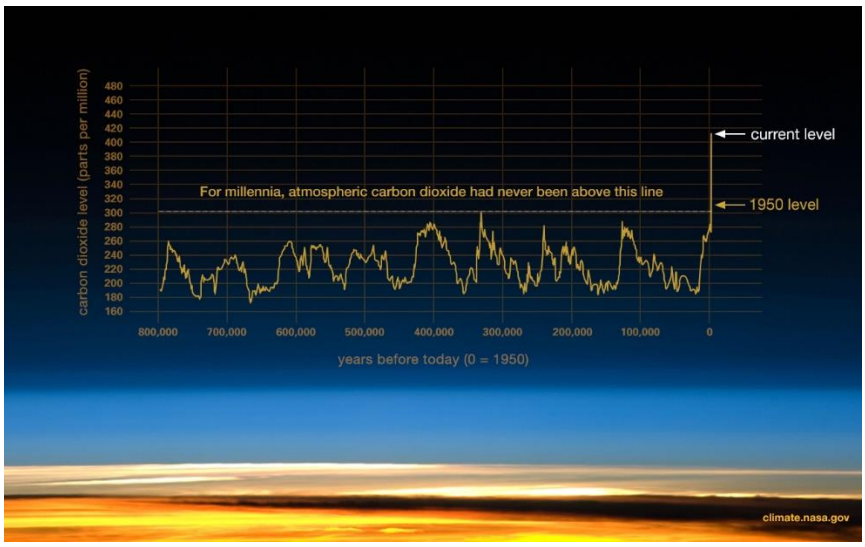

Figure 1.1: This graph, based on the comparison of atmospheric samples contained in ice cores and more recent direct measurements, provides evidence that atmospheric CO_2 has increased since the Industrial Revolution.

In order to control the CO_2 emission and slow down the global warming, the key is to increase the efficiency of the electrical machines and motors. As we all know, the core of these electrical machines is magnetic material. For instances, regarding traditional magnetic materials, low-carbon laminations steels, non-oriented and grain-oriented Fe-Si laminations steels and Fe-Co laminations are still maintaining as the major material for the yoke of motor, generator and transformer. Even though the main trends still focus on the reduction of magnetic loss, the condition and regime change to higher base frequencies due to electric machines high speed and increased time harmonics from the drive systems. As for nonconventional magnetic material, amorphous, nanocrystalline, Soft Magnetic Composites (SMC) and ferrites, these materials are finding their way into the core of specialized electrical machines. Applications of these materials not only decrease the magnetic loss, but also reduce the machines footprint. However, the characterization of these materials is still not fully understandable. The quantitative prediction of the magnetic loss is still under debate. To improve the

efficiency of electric machines, investigating the energy loss behavior of these magnetic materials applied in the electrical machines and motors is essential.

For centuries, the process of physical modelling and magnetic characterization of materials has been addressed. To summarize, there are two main approaches: empirical models and physical models. To build a solid theory, one-dimensional measurement standard has been established. And two-dimensional and three-dimensional measurement are still developing. However, from the developing point of view, as the optimization of the magnetic material, inventions of new electrical machine device and the increasing domain of applications, both experiments and theory are challenged in these new conditions.

1.1 Aim, Scope and the significance of the thesis

The aim of this thesis is to fully investigate energy loss behavior of both conventional magnetic material and nonconventional magnetic material responding broadband frequency through suitable experiments and developing their analytical theory through loss separation theory and statistical theory of loss. I have investigated broadband frequency energy loss behavior of conventional magnetic material, Fe-Si and Fe-Co, and nonconventional magnetic material, nanocrystalline and Ferrite using Epstein frame, Single Sheet Testers, ring sample and Vector Network Analyzer (VNA)setup. To meet the needs of electrical machines application, different conditions are considered such as low and high induction level, different induction waveform and so on. Limits to the research are noted from the start. The experiments are conducted using one-dimensional measurement systems. And the main magnetic loss model has been exploited to develop according to the Statistical Theory of Loss (STL). One intended outcome of the study, on a theoretical level, is to develop the analytical theory to predict the energy loss of magnetic materials responding a broadband frequency, from DC to radiofrequency range. On a practical level, a second intended outcome of the study is to bridge the gap between theory and practice by providing the data under quasi-practical conditions.

1.2 Overview of the thesis

This thesis consists of nine further chapters within two main parts. In PART I(Chap.2 &3&4), I situate the current study in related literature and establish the research methodology. In Chap.2, it includes a critical review of the ferromagnetism, ferrimagnetism, soft and hard magnets and magnetic energy terms, domain structures and magnetization process. Deep understanding of the magnetic properties of magnetic material builds a foundation of the magnetic loss model. Chap.3 introduces the core magnetic loss model ----loss separation theory and statistical theory of loss and related constitute law. In Chapter 4, I give a brief introduction of the experimental technique and measurements setups regarding the experiments in this thesis. Secondly, PART II(Chap.5&6&7&8) is the main part of my thesis. In this part, I present all the experimental results, data analysis, discussions and conclusions. In Chapter 5, the discussion focuses on different classical loss models, their application conditions and the experiments validation regarding non-oriented steel sheets. Chapter 6 presents measurements and prediction of the magnetic loss with minor loop under PWM regime and explores the limits of the analytical approach. Chapter 7 contains energy loss in soft magnetic material under symmetric and asymmetric induction waveform. Chapter 8 discusses the effect of punching and water-jet cutting methods on magnetization curve and energy losses of non-oriented magnetic steel sheets. Finally, in Chapter 9, I present all the conclusions and reflective evaluation of the study and suggest further research agendas.

1.3 List of publications

Journal Publications:

1 Carlo Ragusa, **Hanyu Zhao**, Carlo Appino, Mahmood Khan, Olivier de la Barriere, and Fausto Fiorillo, "Loss decomposition in non-oriented steel sheets:

the role of the classical losses," IEEE Magnetics Letters, vol. 7, no. 1 (2016), 7556414

2 **Hanyu Zhao**, E. Ferrara, V. Manescu Paltanea, G. Paltanea, H. Gavrila, F. Fiorillo, “Effect of punching and water-jet cutting methods on the hysteresis and excess loss components in non-oriented magnetic steel sheets”, Int. J. Appl. Electromagnetics Mech., 55 (2017) pp. 69-76

3 **Hanyu Zhao**, C. Ragusa, M. Khan, C. Appino, O. de la Barrière, F. Fiorillo, “Magnetic loss versus frequency in non-oriented steel sheets and its prediction: minor loops, PWM, and the limits of the analytical approach,” IEEE Trans. Magn. 53 (2017), pp. 2003804.

4 **Hanyu Zhao**, Carlo Ragusa, Carlo Appino, Olivier de la Barrière, Fausto Fiorillo, “Energy losses in soft magnetic materials under symmetric and asymmetric induction waveforms,” IEEE Trans. Power Electronics, regular, to be published.

5 Long Chen, Youhua Wang, Zhenghan Zhao, **Hanyu Zhao**, et al. Measurement of Rotational Magnetic Properties of Nanocrystalline Alloys by A Modified B-H Sensor[J]. AIP Advances, 2017, 17(5): 056614. (SCI: 000402797100335, EI: 20170203226525)

6 Long Chen, Youhua Wang, Zhenghan Zhao, **Zhao Hanyu**, et al. A New Magnetizer for Measuring the Two-Dimensional Magnetic Properties of Nanocrystalline Alloys at High Frequencies [J]. IEEE Magnetics Letters, 2017,8: 6501705 (SCI: 000416514800001, EI: 20170503312668).

7 陈 龙，汪友华，**赵洽宇**(Hanyu Zhao)等. 超微晶合金旋转磁特性测量用激磁装置的设计与优化[J]. 电工技术学报， 2016, 31 (22): 19-27. (EI: 20164903102024)

8 Xinliang Zhang, Youhua Wang, Long Chen, **Hanyu Zhao** and Miao Wang, Shielding effectiveness analysis in a two-dimensional magnetic measurement system, 2016 Asia-Pacific International Symposium on Electromagnetic Compatibility (APEMC), Shenzhen, 2016, pp. 629-631.

Conference Publications:

1 C.Appino, **H.Zhao**, C.Ragusa, M.Khan, Olivier de la Barrière, and Fausto Fiorillo," The classical losses in non-oriented steel sheets.",1&2dm,2016,Tianjin

2 C.Ragusa, **H.Zhao**, M.Khan, O.de la Barriere, C.Appino and F.Fiorillo, "Magnetic losses versus frequency in non-oriented steel sheets and their prediction: the limits of the analytical approach", Magnetics Conference (INTERMAG), 2017 IEEE International

3 **H.Zhao**, C.Appino, O.de la Barrière, F.Fiorillo, C.Ragusa, "Broadband characterization and modelling of magnetic loss in soft magnets", 5th Italian Conference on Magnetism,2017.

Chapter 2

Ferromagnetic materials and magnetization process

2.1 Soft and hard magnets, Ferromagnetism, ferrimagnetism, magnetic energy terms

2.1.1 Magnetic materials categories

Magnetic materials are widely used in life, industry and military. Generally, according to the magnitude and direction of permeability of magnets, the magnetic properties of materials are divided into five categories: diamagnetic, paramagnetic, ferromagnetic, antiferromagnetic and ferrimagnetic material [4]. Figure 1.1 shows the diagrams of magnetic dipole moments in paramagnetic, ferromagnetic and ferrimagnetic magnets. Most of the magnetic materials used in electromagnetic and power electronic devices in real life are ferromagnetic and ferromagnetic materials. These materials can be divided into four categories according to their magnetic properties or application fields: soft magnetic

materials, hard magnetic materials, signal magnetic materials and special magnetic materials [4-6].

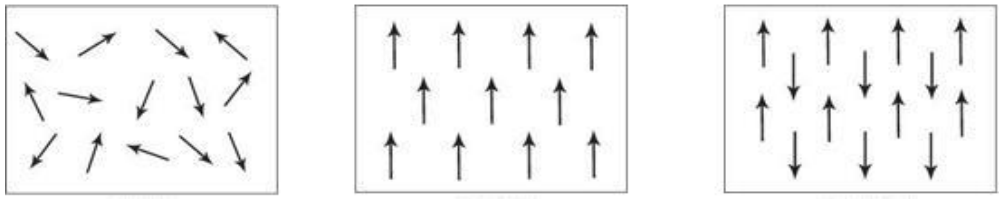

Figure 2.2: Directional diagrams of magnetic dipole moments in paramagnetic, ferromagnetic and ferromagnetic materials

2.1.2 Ferromagnetism

Ferromagnetism is a form of magnetic ordering in which the intrinsic magnetic dipole moment, or spin, of electrons on each crystal-lattice site all align in the same direction. It is the phenomenon that gives materials such as iron, cobalt and nickel their magnetic properties.

Ferromagnetic materials possess a permanent magnetic moment in the absence of an external field and exhibit very large, permanent magnetizations. The spontaneous magnetization is not apparent in materials which have not been exposed to an external field, because of domains in the material. Each domain has its own direction of magnetization. When a field is applied, the domains in which the magnetization is more nearly parallel to the field grow at the expense of the domains with less favorable alignments. Since the spontaneous magnetization may be several orders of magnitude greater than the applied field, ferromagnetic materials have very high permeabilities, e.g., as high as 10^6.When the applied field is removed, a part of the induced domain alignment may be preserved so that the body acts as a permanent magnet. Spontaneous magnetization is due to the alignment of uncompensated electron spins by the strong quantum-mechanical "exchange" force [7]. In **antiferromagnetic** materials, the uncompensated

electron spins associated with neighboring cations orient themselves, below a temperature known as the Néel temperature, in such a way that their magnetizations neutralize one another so that the overall magnetization is zero. Metallic manganese, chromium, and manganese oxide (MnO) are some of the materials exhibiting this behavior.

The susceptibilities of these materials are low ($\sim 10^{-3}$) except when the temperature is close to the Néel point when the antiferromagnetic coupling breaks down and the materials become paramagnetic [8]

2.1.3 Ferrimagnetism

Ferrimagnetism, type of permanent magnetism that occurs in solids in which the magnetic fields associated with individual atoms spontaneously align themselves, some parallel, or in the same direction (as in ferromagnetism), and others generally antiparallel, or paired off in opposite directions (as in antiferromagnetism). The magnetic behaviour of single crystals of ferrimagnetic materials may be attributed to the parallel alignment; the diluting effect of those atoms in the antiparallel arrangement keeps the magnetic strength of these materials generally less than that of purely ferromagnetic solids such as metallic iron. Ferrimagnetism occurs chiefly in magnetic oxides known as ferrites. The natural magnetism exhibited by lodestones, recorded as early as the 6th century BC, is that of a ferrite, the mineral magnetite, a compound containing negative oxygen ions O^{2-} and positive iron ions in two states, iron (II) ions, Fe^{2+}, and iron (III) ions, Fe^{3+}. The oxygen ions are not magnetic, but both iron ions are. In magnetite crystals, chemically formulated as Fe^3O^4, for every four oxygen ions, there are two iron (III) ions and one iron(II) ion. The iron (III) ions are paired off in opposite directions, producing no external magnetic field, but the iron(II) ions are all aligned in the same direction, accounting for the external magnetism.[9]

In this thesis, the research is focus on soft magnetic materials.

2.1.4 Magnetic energy terms

The hysteresis of magnetic materials [10-11] is a macroscopic phenomenon arising from the evolution of micro-magnetic structure. To understand the magnetization process of magnetic materials, we need to understand this process from the perspective of energy. As an energy system, magnetic materials will obey the general principle of minimizing free energy under the excitation of an external magnetic field related to time. The main energy source of magnetic materials here is the domain structure, so the magnetic energy term is introduced in this section, and the domain structure will be discussed briefly in the next section.

For magnetic materials, Helmholtz free energy **F** can be assumed as a complex function of magnetization *M*. Magnetization *M* (*r*) is used to express the magnetization at any point in the sample volume. Energy can be expressed as a multi-valley random structure, and when the applied magnetic field H_a changes, energy will begin to traverse. In principle, according to the minimum condition applied to Gibbs free energy ***G*** principle, the system will search for the magnetic structure that can make the sample energy reach local equilibrium, and the following formula can be obtained at equilibrium.

$$G = F - \mu_0 \int_V H_{\mathrm{a}} \cdot M(r) d^3 r \tag{2.1}$$

Here *V* refers to the volume of the sample. The right integral term is the energy of the interaction between the magnetic field and the magnetization of the magnetic material, which is usually called Zeeman energy. If we generalize this energy, we can get M_i is a general expression of magnetic moment in magnetic material under the excitation of magnetic field intensity H_a. According to the energy relationship of the system:

$$F = U - TS \tag{2.2}$$

Here ***U*** represents the sum of internal energy exchanges, ***T*** stands for temperature, ***S*** is entropy. The introduction of micro-magnetism is to find the magnetization M (r) at any position in the sample when the energy of ***G*** is the smallest when the sample is regarded as a homogeneous medium and the magnetization intensity is equal everywhere. In fact, under this condition, there are more than one magnetization intensity M (r) satisfying the minimum condition of ***G*** in real materials, which is the unique property of magnetic hysteresis. Although the micromagnetic equation is very complex, it is possible to solve the micromagnetic equation under several ideal conditions and has some practical significance. However, in practice, to solve this problem, we usually use experience to assume a variety of micro-magnetic structures and calculate the energy associated with them, and then compare one by one to find the minimum energy. Experiments show that the magnetic sample with larger than a certain size is composed of domain structure, which can minimize the Gibbs energy ***G*** of the magnetic sample, and the magnetization intensity M (r) in the domain is uniform and has a definite direction. But the direction of magnetization in different domains is different. The transition between two adjacent domains is connected through a continuous interface, which is called domain wall. Domains and domain walls are the basis for describing the magnetization process of materials. The magnetic energy terms are given below.

(1) Magnetostatic energy

Because of the hysteresis, the ferromagnet remains magnetized after the external magnetic field disappears. This magnet with remanence has a certain energy, which is called magnetic static energy and is generally expressed as

$$U_{\mathrm{ms}} = -\frac{1}{2}\mu_0 \int_V H_d \cdot M dV \tag{2.3}$$

Here H_d is the demagnetization field, the integral is the volume of the whole sample, and the coefficient of 1/2 indicates the interaction between the magnetic moments. H_d can be solved by Maxwell's equation when the shape of the magnet is special.

(2) Exchange energy

The spontaneous magnetization of ferromagnets originates from quantum exchange forces, which keep each magnetic moment in the same direction below Curie temperature. From a phenomenological point of view, this effect is generated by an internal magnetic field, namely the Weiss molecular field, which also becomes the exchange magnetic field H_{ex}. Exchange interactions are often considered to occur at adjacent spin electrons. Based on the Heisenberg model, the exchange energy is expressed as follows:

$$\mathcal{H} = -\sum_{i,j} J_{ij} S_i \cdot S_j \tag{2.4}$$

Among them, S_i and S_j are electron spin magnetic moments of two adjacent ions. In ferromagnets, J_{ij} is a positive number. So the minimum energy is when the spin magnetic moments of any two adjacent ions are parallel and in the same direction. If S_i and S_j are not parallel, the product of the two decreases and the energy increases. For this energy increase, it can be expressed by Taylor expansion of Heisenberg model. For a cubic lattice structure, the exchange energy density is approximately expressed as follows:

$$u_{ex} = \frac{1}{V} \cdot \frac{A}{M_s} \int_V (|\nabla M_x|^2 + |\nabla M_y|^2 + |\nabla M_z|^2) d^3 r \tag{2.5}$$

A is the exchange stiffness constant, which is related to J_{ij}' integral. M_s is saturation magnetization.

(3) Anisotropic energy

The macroscopic behavior of ferromagnetic materials is usually not isotropic, but anisotropic. To change the magnetic moments of internal atoms, which need to consume energy, this part of energy is anisotropic energy. Anisotropy can usually be divided into the following categories: lattice anisotropy, stress-induced anisotropy and shape or other anisotropy.

The main mechanism of lattice anisotropy is the coupling of spin magnetic moment S, which interacts with electron orbital angular momentum L by exchanging magnetized carriers. The orbital angular momentum L of an electron cannot be arbitrarily oriented. It is bound to the lattice by the crystal field. Therefore, the response of material to external magnetic field depends not only on the interaction between electron spin magnetic moment and orbital angular momentum (L-S), but also on the interaction between orbital angular momentum and crystal field. This explains why some natural easy-to-magnetize axis directions are determined by the symmetry of crystal field. Based on symmetry, the spatial dependence expressions of anisotropic energy density can be derived for uniaxial or cubic lattice materials.

$$\text{In cubic crystals: } u_{an} = K_1(\alpha_1^2\alpha_2^2 + \alpha_2^2\alpha_3^2 + \alpha_3^2\alpha_1^2) + K_2\alpha_1^2\alpha_2^2\alpha_3^2 \tag{2.6}$$

Among them, α_1, α_2, α_3 represent the direction cosine of magnetization and the edge of cubic lattice, and K_1 and K_2 represent the anisotropic coefficient.

$$\text{In hexahedral crystals: } u_{an} = K_1 \sin^2\theta + K_2 \sin^4\theta \tag{2.7}$$

θ is the angle between the magnetization and the axis of easy magnetization, and K_1 and K_2 are the anisotropic coefficient. The lattice structures of different elements are different, and the corresponding easy magnetization axes are different.

Stress-induced anisotropy refers to the lattice elastic distortion caused by stress, which affects the effect of the crystal field on the orbit, thus causing the anisotropy of magnetic materials. The anisotropy of real materials is also closely related to the magnetostriction of materials.

Shape anisotropy is related to the demagnetization field mentioned above. In addition to these anisotropies, in practice, magnetic anisotropy can also be introduced by promoting or freezing the arrangement of atomic structures in alloys, mainly including introduction methods: first, magnetic annealing; second, stress annealing; third, plastic deformation; fourth, magnetic radiation and so on.

It is pointed out that the above energies are not independent of each other, but the magnetic energy terms minimize the Gibbs energy of the whole system, and then determine the magnitude and direction of the magnetization intensity of each point in the sample, which is the actual domain structure.

2.2 The domain structures

The shape, size, type and thickness of domain wall are called domain structure. It has been stated above that the formation of magnetic domains is to reduce the energy of materials, so the domain structure in material should minimize the sum of magnetic static energy, exchange energy and other energy.

(1) Domain Wall

If the domain walls are classified according to the angle of the domain magnetization vectors on both sides of the domain walls, the domain walls can be divided into 180-degree and 90-degree domain walls, as shown in Figure 2.2.

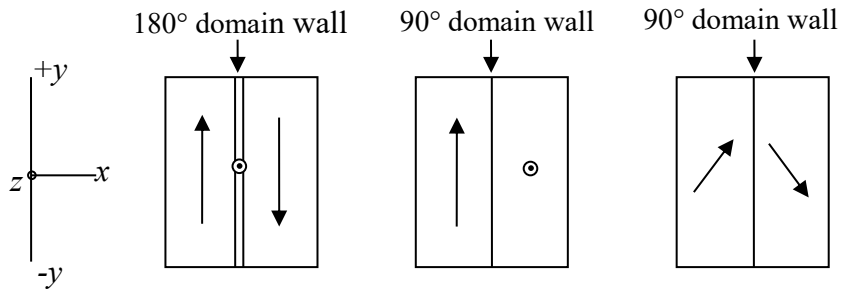

Figure 2.3: 180° domain wall and 90° domain wall

The direction of the magnetic moment in the domain wall gradually changes. According to the mode of the magnetic moment transformation, the domain wall can be divided into Bloch domain wall [12] and Neel domain wall [13]. As shown in Figure 2.3, the characteristic of Bloch domain wall is that the magnetic moment rotation in the domain wall is always parallel to the plane of the domain wall. When the thickness of the ferromagnet is reduced to the same as that of the domain wall, the domain wall is Neel domain wall. The transformation of magnetic moment is always parallel to the surface of the sample. The domain wall in the nanocrystalline material mentioned in this thesis is an example.

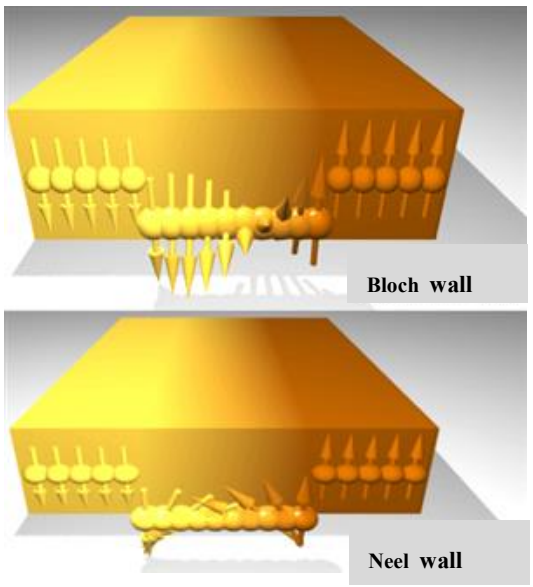

Figure 2.4: Diagram of magnetic moment rotation of Bloch domain wall and Neel domain wall

2.3 The magnetization process in soft magnetic materials: static and dynamic response

The static and dynamic response correspond to rate-independent and rate - independent hysteresis from micromagnetic point of view. Rate-independent hysteresis applies when Barkhausen jumps develop in times much shorter than the time scale fixed by the field rate of change. Under this approximation, a Barkhausen jump appears as an instantaneous event, of which we do not see the internal structure. Yet, a system always needs a certain time to react varying external actions. This is the case, for example, in metallic ferromagnets, where magnetizations changes are damped by the production of eddy currents. When the spontaneous evolution of the system through Barkhausen jumps and the forced evolution driven by the external field take place on comparable time scales, rate-independent approximations are no longer applicable, and more general frames of description are needed. So practically, when soft magnetic material is magnetized

by very slow changed of field, we call this static response. When material is magnetized by alternating field, the magnetic hysteresis occurs which it is dynamic response. One of the most important phenomena causing the magnetic hysteresis is interaction of magnetic domain structure with material's crystalline structure [10]. Due to magnetic domain walls pinning on the grain boundaries, irreversible part of magnetization is observed, causing magnetic hysteresis [11].

Chapter 3

The magnetic losses

3.1 Introduction to the phenomenology of magnetic losses

Magnetism loss refers to the irreversible transformation of some energy into heat in the process of magnetization and demagnetization of magnetic materials. The energy loss is called magnetic loss. Magnetic hysteresis is equal with energy dissipation. Research on the magnetization process and predictive efforts regarding its dependence on the nature of the material and the type of external excitation are in many cases directed at assessing the phenomenology of magnetic losses. In particular, soft magnetic materials are ubiquitously found. The physics of magnetic hysteresis is central to the problem of core efficiency and methods for the prediction of the energy loss based on the previously discussed concepts of magnetism and magnetization processes exist. We shall discuss such methods in the following, with special emphasis devoted to the principle of loss separation

3.2 Losses in metallic and in insulating magnetic material

At first Bertotti only applied statistical loss theory to eddy current loss mechanism, because this loss mechanism is the only important mechanism for metals in low and intermediate frequencies. The eddy current loss is dominant in general, but in fact other energy dissipation mechanisms exist at the same time, but Bertotti did not consider other dissipation mechanisms when he put forward his theory. With the development of the future, the statistical loss theory can be generalized, and can also be applied to insulating/semi-insulating ferrites after appropriate adjustment. It was first applied and developed from Dillon and Earl's experiments on manganese-zinc ferrites [14]. Here, the mechanism of electron spin wave attenuation energy dissipation is introduced. In fact, other loss mechanisms exist, such as friction mechanisms on domain walls (e.g., post-diffusion and post-relaxation effects), magnetic coupling and sound generation, etc., but these mechanisms are usually important only for a few alloys and for specific temperature ranges. In metal alloys, eddy current loss mechanism is still dominant. In amorphous and ultramicro-crystalline tapes, only at very high frequencies can the energy dissipation mechanism of electron spin-wave attenuation become the main dissipation mechanism. By introducing the Landau-Livschitz formula of domain dynamics as the constitutive equation describing magnetic materials, Bertotti's theory can also be used for loss separation and prediction [15]. The theory of loss separation and statistical loss will be elaborated in detail below.

3.3 Magnetic loss modelling

Magnetic loss modelling as magnetic cores can be divided into three main categories: first, empirical Steinmetz formula and its improved method [16-18]; second, numerical calculation method of hysteresis model based on physical

properties of materials [19-21]; third, analysis method based on physical model of loss separation and statistical loss theory [22]. In addition to these three main methods, there are also various methods of improvement and combination modelling. The first method uses experimental data to fit the loss coefficient in Steinmetz formula. It is widely used by engineers because of its concise expression. However, it cannot be applied to complex working conditions and wide frequency range because it is not a physical model of magnetic material loss. The hysteresis models in the second method include Globus [23], Preisach [19], Stoner-Wohlfarth [24], Jiles-Atheton (J-A) [25,26] and so on. Most of these models are based on material physical modelling, but numerical methods are usually used to solve the dynamic loss part, which requires a large amount of calculation and is mainly suitable for application in simulation software. Based on the mechanism of magnetic loss, the third method separates the loss by using the micro, meso and macro scale of space-time, and divides the magnetic loss into hysteresis loss, excess loss and classical loss (also known as eddy current loss). On this basis, Bertotti put forward the concept of magnetic objects (MO), deduced the method of calculating the excess loss, and then established a complete set of basic models for predicting the loss of magnetic materials, namely the Statistical Theory of Loss (STL) [22]. This method only needs less experimental data to establish a more universal calculation method, which has high accuracy and moderate computational complexity. Because this paper does not involve complex numerical calculation methods, the hysteresis model will not be analysed in detail, only the Steinmetz formula, which is also applicable to engineering applications, will be analysed and the statistical loss theory will be introduced in detail.

3.3.1 Steinmetz formula

In 1892, Engineer Steinmetz proposed the famous Steinmetz formula to calculate the total loss of magnetic materials [16]:

$$P_{\text{tot}} = C_{SE} f^{\alpha} B_p^{\beta} \tag{3.1}$$

C_{SE}、α、β are the fitting constants, depending on the material. At very low frequencies, the total loss is only attributed to hysteresis loss, when β=1.6. At high frequencies, these three constants can be obtained by fitting experimental data. It should be noted that the standard equation is only applicable to sinusoidal wave. With the wide application of power electronic equipment, a lot of harmonics are introduced into motor and transformer equipment. To predict the loss caused by non-sinusoidal wave excitation, many modified Steinmetz formulas are proposed by researchers. One of the methods is to decompose the waveform of magnetic induction intensity by Fourier series and calculate the loss of each harmonic wave. However, this method is accurate only when the magnetic induction intensity is in unsaturated state. Subsequently, the standard Steinmetz equation is extended to predict losses under arbitrary magnetic induction waveforms [17,27]. The formulas are as follows:

$$P_{\text{tot}} = C_{SE} f_{\text{eq}}{}^{\alpha-1} B_p^{\beta} f \tag{3.2}$$

Here the equivalent frequency is:

$$f_{\text{eq}} = \frac{2}{\pi^2 \Delta B^2} \int_0^{1/f} (dB/\mathrm{d}t)^2 dt \tag{3.3}$$

Among them. When the peak value of sinusoidal magnetic induction intensity is B_{p} excitation, it can be deduced that:

$$f_{\text{eq}} = \frac{2}{\pi^2 4 B_{\text{p}}^2} \int_0^{1/f} (\omega^2 B_{\text{p}}^2 \cos^2 \omega t) dt = f \tag{3.4}$$

It coincides with Formula (3.2). Later, a generalized modified Steinmetz formula was proposed (GSE) [28]. The loss is given as a function of the derivative of magnetic induction intensity and magnetic induction intensity.

$$P_{\text{tot}} = \frac{1}{T}\int_0^T C_{SE}\left|\frac{dB}{dt}\right|^{\alpha}\left|B(t)\right|^{\beta-\alpha} dt \tag{3.5}$$

Although Steinmetz and its improved method are very simple, there are some limitations related to this method. Because it is not based on physical principle, the coefficient of Steinmetz is very dependent on frequency. When the frequency changes, the coefficient changes sharply. It is worth pointing out that the Steinmetz equation cannot realize the broadband prediction of material loss.

3.3.2 The Jiles-Atherton Modeling

The principles of Jiles-Atherton model is connected with the analysis of the total free energy of the magnetic material [29]. In the Jiles-Atherton model it is assumed that the energy term can be expressed in terms of the anhysteresic curve $M_{\text{an}}(H_{\text{a}})$. The hypothesis is that the stored energy should coincide with the work that would be performed on the system in the absence of hysteresis. The other term δQ corresponds to the dissipated energy, is taken proportional to the change in magnetization dM, with a factor k. This factor is proportional to the number of pinning sites seen by a moving domain wall. Each pining event will give rise to a Barkausen jump, and when integrated over the entire specimen, it will produce a dissipation contribution proportional to the pinning field k. Using these assumptions Jiles and Atherton derived the following expression for the differential susceptibility along a saturation loop under increasing field

$$\frac{dM}{dH_a} = \frac{M_{an}(H_a) - M(H_a)}{k} \tag{3.6}$$

This equation represents the simplest case, where internal coupling fields are absent.

3.3.3 Preisach Model

Quantitative model of magnetization process proposed by Ferenc Preisach in 1935[30] is still one of the most popular and commonly used model of magnetic hysteresis loop. This model is based on the concept of hypothetical elementary Preisach particle (so called "hysteron") with square shaped hysteresis loop and saturation magnetization $\boldsymbol{m}$. The M-H hysteresis loop of such elementary Preisach particle is presented in the Figure 3.1. As it is presented in the Figure 3.1, the elementary Preisach particle is described by saturation magnetization $\boldsymbol{m}$, switching magnetizing fields a and b and its coercive field H_c and interaction field H_u [48]. It should be highlighted, that hysteresis loop of elementary particle is not symmetric. This effect is caused by the influence of neighbouring domains. The macroscopic properties of magnetic material are described by the probability density function n(a, b), which for very large number of elementary Preisach particles tends to continuous density function lP(a, b). In his original works Ferenc Preisach proposed the method of determination of magnetic hysteresis loops on the base of graphical diagrams. Basing on these ideas, in 1955, Douglas Hugh Everett proposed the function [31] enabling numerical calculation for the Preisach model, known as Everett function. It should be stressed that modifications of Everett function are the key elements of development of Preisach model [32].

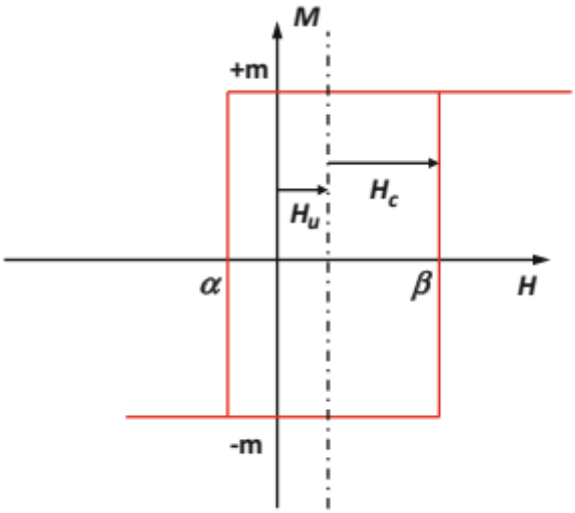

Figure 3.1: Hysteresis loop of hypothetical elementary Preisach particle

3.4 The Statistical Loss Model and the physically based concept of loss separation

Because of the viscous dynamic effect of eddy current in metals, hysteresis occurs even at very low magnetization frequencies, which leads to magnetic loss. The calculation of loss should be derived from a general hysteresis model, which should be able to predict the magnetization curve and hysteresis loop, thereby calculating the area of hysteresis loop, and then get the loss. However, in fact, the current research shows that there is no such wideband universal hysteresis model. How to solve the loss problem directly without detailed description of the magnetization process has become the focus of research. In fact, the magnetization of magnetic materials occurs on a widely distributed time and space scale, so the total eddy current loss is calculated from the statistical average values of many randomly distributed parts. These statistical averages show some main characteristics, and many details about the magnetization process are proved to be totally unrelated to the total loss after average, so it is not necessary to

consider them. And some main characteristic attributes are particularly important when calculating the loss [33]. These loss parts separate the total loss, which is a widely used loss separation method. According to the principle of loss separation, the total loss can be divided into hysteresis loss W_{hyst}, classical loss W_{class} and excess loss W_{exc}. Then the total loss expresses as follow:

$$W_{\text{total}} = W_{\text{hyst}} + W_{\text{class}} + W_{\text{exc}} \tag{3.7}$$

The existence of viscous damping mechanism in metallic materials leads to the introduction of a characteristic time scale in the magnetization process. When the external magnetic field varies in a certain extent in this time scale, the area of the hysteresis loop increases. To quantitatively describe this effect, the evolution of domain structure of magnetic materials under variable magnetic fields should be calculated in principle. However, the evolution of domain structure is a very complex micro magnetism problem. If the Maxwell equations are coupled by Brown equation, the spatial and temporal distributions of magnetization $M(r, t)$ and eddy current density $j(r, t)$can be obtained by this solution. Under periodic excitation of frequency f, the average loss per unit volume per unit time can be expressed as follows

$$P = f\int_V \frac{d^3r}{V}\int_0^{1/f} \frac{\left|\overrightarrow{j(r,t)}\right|^2}{\sigma} dt \tag{3.8}$$

V is the volume of the sample. In most cases, however, the solution given by this formula is only formal, because it is extremely complex to attempt to solve the problem with the dynamic micro magnetism method. The complexity of the overall energy of the system results in the instability of the wide distribution in space and duration. In addition, the eddy current tends to concentrate around the moving domain wall, which leads to the complexity of the domain structure. In addition, the whole problem depends heavily on the geometric size of the sample, because the eddy current is not only determined by the local properties of the

material, but also by the overall geometric shape of the sample. It can be concluded from the analysis that the eddy current density function $j(r, t)$ has a very complex spatial and temporal distribution and can only be quantified in a statistical way. Therefore, the focus of the study will no longer be on calculating the specific value of formula (3.8), but on identifying which main features may exist completely independent of the specific details.

In order to quantify and solve the formula (3.8), we will make some simplifications which are approximately equivalent to the actual situation. First, assuming that the material sample is infinitely long, the demagnetization field can be ignored. The applied magnetic field intensity H_a is uniform in space and applied along the longitudinal axis of the sample, which is z axis. Magnetization M and magnetic induction B are perpendicular to the cross section of the sample everywhere, and they are independent of z. In other words, only the change of magnetization M along the infinite cylindrical element of the sample is considered. Under these assumptions, according to the translation invariance along z, the problem described can be simplified to a two-dimensional problem in the dy plane. External magnetic field intensity H_a, sample magnetic field intensity H, sample magnetization intensity M, magnetic induction intensity B can be regarded as scalar. The electric field strength E and eddy current density j ($j=\sigma E$) can be used as vectors on the xy plane and expressed by the fractions on the x and y axes respectively. The total sample magnetic field strength $H= H_a +H_{\text{eddy}}$, H_{eddy} which is generated by eddy current.

According to Poynting's theorem, the energy inflow of the whole system follows the direction of the magnetic field intensity H along the z axis. In addition, the tangential component of the magnetic field is continuous on the sample surface, that is, the sample magnetic field strength H on the sample surface is equal to the external magnetic field strength H_a. Because the electric field

intensity is in the *xy* plane and the direction is tangent to the sample surface, the energy of injected sample per unit volume per unit time is obtained as follows:

$$\oint_{S}(E\times H)dS=\frac{H_{a}}{S}\oint_{C}E\cdot dl=\frac{H_{a}}{S}\frac{d\Phi}{dt}=H_{a}\frac{d\langle B\rangle}{dt} \tag{3.9}$$

The line integral is the integral along the contour path *C* of the sample cross-section area, and *S* is the *xy* cross-section area. The flux through the cross-section area is expressed by Faraday's law of electromagnetic induction. $\langle B\rangle=\Phi/S$ represents the average magnetic induction intensity of the cross-sectional area of the sample, and $d\Phi/dt$ is the voltage value measured by the coil wound around the sample. The conclusion is that if the magnetic induction intensity $\langle B\rangle$ is expressed by the external magnetic field intensity H_a and the figure is drawn, this is the hysteresis loop, and the area of the hysteresis curve represents the energy loss per unit volume of a magnetization period. The integral of hysteresis curve area to time calculated by formula (3.9) is equal to the loss calculated by formula (3.8), if eddy current loss is the only important dissipation mechanism. Thus (3.8) can write:

$$P=f\int_{s}\frac{d^{2}\mathrm{r}}{S}\int_{0}^{1/f}\frac{\left|j(r,t)\right|^{2}}{\sigma}dt \tag{3.10}$$

In order to study the properties of this integral, a specific cross-sectional area is selected. In this paper, we take a sample with thickness d as shown in Figure. 3.2. On the one hand, this geometric shape produces relatively simple mathematical expressions, on the other hand, it is also the most commonly encountered geometric shape in applications, such as silicon steel sheets. If the width of the plate is large enough, here the demagnetization effect can be neglected.

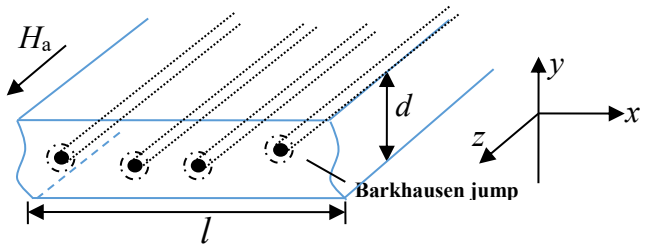

Figure 3.2: Sample Simplified Diagram with Thickness *d* and Principle Simplified Diagram of Barkhausen jump

1) Barkhausen jump sequence

In order to explore the general loss properties, we will focus on the qualitative aspects as much as possible. The complexity of the magnetization process can be easily explained by the magnetization inversion associated with a random Barkhausen jump sequence. Each jump is the result of some local instability, such as the sudden release of the domain wall in pinning and the reversal of magnetic flux in the cylindrical element shown in Figure. 3.2. The transient eddy current around the jump is the cause of energy loss. The jump sequence is represented by the flux change, and it is assumed that all jumps cause the same flux change, which is that all jumps produce the same flux change rate. Once the local flux inversion is concretized, the spatial-temporal eddy current distribution around a single jump can be calculated by Maxwell's equations.

If $j(r, t; r_p, t_p)$ is used to denote the eddy current density associated with the jump at the spatial position r_p and the time t_p. r_p and t_p are random variables. The characteristics of magnetization are summarized by summarizing the statistical properties of (r_p, t_p) sequences. When passing through an eddy current ring, the magnetization of the material changes from $-M_{max}$ to $+M_{max}$ in each half cycle, i.e. $1/2f$. It is assumed that N random Barkhausen jump sequences are completed,then

$$N = \frac{2SM_{\max}}{\Delta\Phi} \tag{3.11}$$

The same completely similar analysis applies to the second half of the cycle. According to the linear property of Maxwell equation, the total eddy current density $j(r, t)$ generated by Barkhausen jump sequence is the sum of the single eddy current density generated by a single jump:

$$j = \sum_{\mathrm{p}=1}^{N} j_{\mathrm{p}} \tag{3.12}$$

According to formula (3.10), the loss problem is simplified to the square of formula (3.12):

$$\left|j\right|^2 = \sum_{\mathrm{p}} \left|j_{\mathrm{p}}\right|^2 + \sum_{\mathrm{p}\neq\mathrm{q}} j_{\mathrm{p}} \cdot j_{\mathrm{q}} = N\left\langle \left|j_{\mathrm{p}}\right|^2 \right\rangle + N^2 \left\langle j_{\mathrm{p}} \cdot j_{\mathrm{q}} \right\rangle \tag{3.13}$$

Angular brackets denote the statistical average of all jump or jump pairs, and assume that N is very large, so $N(N\text{-}1) \approx N^2$. Formula (3.13) is the sum of two terms, and the total loss is naturally expressed as the sum of two contributions, namely, hysteresis loss and dynamic loss.

2) Hysteresis Loss

Firstly, the term of coefficient N in formula (3.13) is considered. When this term is inserted into the formula (3.10) and integrated in time and space, the average energy loss E_{BJ} at unit length z of $2fN/S$ times is obtained. If other circumstances are not considered, this energy is the energy produced by a single Barkhausen jump. When formula (3.11) is introduced, it becomes as follows:

$$P_{\mathrm{hyst}} = 4fM_{\max}\frac{E_{\mathrm{BJ}}}{\Delta\Phi} \tag{3.14}$$

This loss part is called hysteresis loss. The calculation of hysteresis loss is related to the ability to solve a single Barkhausen jump. However, it is usually more convenient to solve this problem on a relatively rough spatial scale, so that the detailed information will be ignored. In this rough scale, the information of small-scale eddies generated around a single jump will be ignored and only the large-scale eddies will be considered. If the description problem is not properly corrected, this method will completely change the loss estimate. Loss separation provides a reliable solution because it allows for the representation of hysteresis by covering eddy current effects at fine scales with a rough constitutive relation B (H). This law provides a background for correctly dealing with macro-scale effects. This is what will be discussed in the next section. It is noteworthy that all the information of energy dissipation is concentrated in the constitutive relation $\Phi(H_a)$. However, the cost of such a sharp simplification is that the constitutive relationship becomes rate-dependent. Usually, rough constitutive relation should be avoided when Barkhausen jump and rate-independent hysteresis are in fine scale.

3) Dynamic loss

Consider again the term proportional to N^2 in formula (3.13). This depends on the correlation of jump sequences. It produces a loss part which is stronger than the simple proportional relation but relatively dependent on frequency f, which is called dynamic loss. In this regard, the simplest case is, of course, that each Barkhausen jump is statistically independent of each other. In this case, $N^2\langle j_p \cdot j_q\rangle = \langle Nj_p\rangle^2$. However, due to the linearity of Maxwell's equations, the average current density is only the current density generated by the average magnetization rate on the cross-sectional area of the sample. In other words, if P(r, t) is the probability of Barkhausen jump at position r and time t, $\langle Nj_p\rangle$is the eddy current density obtained by solving Maxwell equations whose magnetization rate is

proportional to probability P(r, t). Usually P(r, t) is a smooth function of r and t. The domain wall sweeps across the cross-sectional area of the material and tends to periodically aggregate at any position. Generally, if the medium is homogeneous, the probability of magnetization inversion occurring at any point in the cross section of the material is the same. In this case, P(r, t) is independent of position r, and can be simply seen as proportional to the total flux change rate $d\Phi/dt$. The discrete jump structure disappears in the mean value, and the loss is for a completely smooth medium without magnetic domains. This part of loss is called classical loss. Many Chinese literatures also call it eddy current loss. But in order to distinguish it from the loss mechanism, this part of loss is called classical loss in this paper. This part will be discussed in detail in the thesis. Generally speaking, jumps are not statistically independent, even if they are anywhere in space. Because once a Barkhausen jump occurs in a domain wall, there will be a high probability that the next jump will occur at another point in the same domain wall, or in some related regions, including simultaneous active domain walls or other situations. The important point is that the existence of these correlation effects is the direct result of the existence of domain structure. This formula (3.13) should be rewritten as follows

$$|j|^2 = \sum_{\mathrm{p}} |j_{\mathrm{p}}|^2 + \sum_{\mathrm{p}\neq\mathrm{q}} j_{\mathrm{p}} \cdot j_{\mathrm{q}} = N\left\langle |j_{\mathrm{p}}|^2 \right\rangle + \left\langle N j_{\mathrm{p}} \right\rangle^2 + N^2 \left(\left\langle j_{\mathrm{p}} \cdot j_{\mathrm{q}} \right\rangle - \left\langle j_{\mathrm{p}} \right\rangle^2 \right) \tag{3.14}$$

By substituting this formula into formula (3.10), three different loss components are obtained:

$$P = P_{\mathrm{hyst}} + P_{\mathrm{class}} + P_{\mathrm{exc}} \tag{3.15}$$

In addition to the hysteresis loss and classical loss discussed earlier, the third term P_{exc} is generated due to the correlation effect, which is the excess loss. Formula (3.14) shows that loss separation is a general result of the random nature of the magnetization process. Therefore, it should be noted that when randomness

is no longer the dominant factor, loss separation will no longer be applicable. For example, a single 180° domain wall in a framed single crystal is certainly not the best target for statistical processing. In small-amplitude hysteresis cycles, small oscillations occur in the domain wall at a fixed position, and the statistical mean discussed previously is no longer applicable. However, stochastic characteristics are ubiquitous and provide a strong support for the hypothesis of loss separation, which can be dealt with in most cases. This theory is of great significance in predicting the relationship between loss and frequency f and peak magnetic polarization intensity.

3.5 Quantitative Formulas and Procedures of Loss Separation using the Statistical Theory of Loss

Taking 0.194mm silicon steel sheet as an example, the physical model is simplified as shown in Figure 3.2 under the excitation of 1T peak magnetic induction intensity.

1) Hysteresis loss

The cause of hysteresis loss has been analysed in last part. In practical, it is generally considered that the static loss is independent of frequency. By measuring the loss under quasi-static (2-20Hz), the total loss when linear extrapolation f is 0, that is hysteresis loss.

2) Classical Loss

This section gives specific analysis in the following specific chapters. This will not be repeated here.

3) Excess loss

Excess loss is the loss at domain scale. Different calculation models are obtained according to different domain models. Weiss first proposed the concept of magnetic domain in magnetic materials [34], which magnetizes in different directions and minimizes energy in a specific arrangement. When such a domain structure is placed in an external variable magnetic field, the motion of the domain wall changes the eddy current path around the domain wall, resulting in excess loss [35]. The earliest excess loss model was proposed by William, Shokley and Kittel for single domain wall model [36]. Later, the periodic domain wall model was proposed by Pry and Bean [37], and the excess loss of a series of 180-degree domain walls in magnetic materials in an infinite plate was studied. However, in real materials, the size and shape of magnetic domains are not fixed and change with position and time. In order to consider this random domain structure, Bertotti introduced a statistical method to overcome the obstacle of describing this loss, proposed a random domain wall model, and finally gave the expression of excess loss. First, the power loss of random domain wall is shown as follows:

$$P_{RW}(t) = P_{\text{class}}(t) + \frac{\lambda}{d}\langle P_{\text{w}}(t)\rangle \tag{3.16}$$

The total dynamic loss is divided into two parts. The second term at the right end is the expression of excess loss power. $P_{\text{W}}(t)$ is the average dissipation power of each domain wall, and λ is the average density of the domain wall. $2L = 1/\lambda$ is the distance between the domain walls. Firstly, the excess loss domain can be expressed as:

$$H_{\text{exc}} = P_{\text{exc}} / (d\Phi / dt) \tag{3.17}$$

If only the effect of excess magnetic field on a single domain wall is considered:

$$H_{\text{exc}} = \sigma G \frac{d\Phi^{(\text{W})}}{dt} \tag{3.18}$$

For a case where the number of domain walls is n, the total flux change should be equal to the overall flux change of the material:

$$n\frac{d\Phi^{(\mathrm{W})}}{dt} = S\frac{dJ}{dt} \tag{3.19}$$

Then the excess loss can be expressed as:

$$H_{\mathrm{exc}} = \frac{\sigma GS}{n}\frac{dJ}{dt} \tag{3.20}$$

This formula can only be applied to the case where the domain wall spacing (2L) is much larger than sample thickness d [38]. This energy is described from the Barkhausen jump sequence:

$$P_{\mathrm{exc}} = \sigma G^{(\mathrm{is})}\frac{d\Phi^{(\mathrm{cl})}}{dt}\frac{dJ}{dt} \tag{3.21}$$

$G^{(\mathrm{is})}$ is an internal structure function, which is the average flux change related to the Barkhausen jump sequence. At the domain scale, there is still a high probability that the domain walls are surrounded by many other domain walls, forming a unit. A concept introduced here, the unit is called magnetic object (MO), and it randomly distributed. For a hypothesized internal structure of $G^{(\mathrm{x})}$, the flux change rate $d\Phi^{(x)}/dt$ satisfies the random distribution. For a hypothesized N magnetic objects, the excess magnetic field can be deduced as follows:

$$H_{\mathrm{exc}} = \frac{\sigma G^{(x)}\mathrm{S}}{n}\frac{dJ}{dt} \tag{3.22}$$

Here introduce $\tilde{n} = nG/G^{(x)}$, substitute this equation to formula (3.22), we can get:

$$H_{\mathrm{exc}} = \frac{H^{(\mathrm{x})}}{\tilde{n}} \tag{3.23}$$

It represents the excess magnetic field of a material whose entire flux change is concentrated on a single 180-degree domain wall. When the frequency is low, the magnetization process is very uneven, because the sample correlation activity is very little. With the increase of the frequency, the related active areas gradually increase, and the magnetization process becomes more and more uniform. It can be seen as a general equation expressed by H_{exc}, which increases with the increase of H_{exc}. In order to express this process, parameters n_0 and V_0 are introduced [10].

$$\tilde{n}(H_{\text{exc}}) \cong n_0 + H_{\text{exc}} / V_0 + \ldots\ldots \tag{3.23}$$

n_0 is the number of magnetic object (MO) in the sample when the frequency is close to zero, and V_0 is the statistical parameter for aligning other magnetic objects in the same direction. Formula (3.23) shows that the excess magnetic field decreases with the increase of the number of active magnetic units. On the other hand, formula (3.23) shows that the number of active regions increases with the increase of residual magnetic field. When the formula (3.23) is established, it is brought into the formula (3.22), and the quadratic equation about H_{exc} is solved.

$$H_{\text{exc}} = \frac{n_0 V_0}{2}\left(\sqrt{1 + 4H^{(x)} / n_0^2 V_0} - 1\right) \tag{3.24}$$

$$\begin{aligned} H_{\text{exc}} &\cong H^{(x)} / n \equiv \frac{nGS}{n_0}\frac{dJ}{dt} && \text{当 } 4H^{(x)} / n_0^2 V_0 << 1 \\ H_{\text{exc}} &\cong \sqrt{H^{(x)} V_0} / n \equiv \sqrt{\sigma GSV_0}\left(\frac{dJ}{dt}\right)^{1/2} && \text{当 } 4H^{(x)} / n_0^2 V_0 >> 1 \end{aligned} \tag{3.25}$$

The whole problem is solved by determining two parameters n_0 and V_0:

$$P_{\text{exc}}(t) = H_{\text{exc}}\frac{dJ}{dt} = \frac{n_0 V_0}{2}\left(\sqrt{1 + 4H^{(x)} / n_0^2 V_0} - 1\right)\frac{dJ}{dt} = \frac{n_0 V_0}{2}\left(\sqrt{1 + \frac{4\sigma GS}{n_0^2 V_0}\frac{dJ}{dt}} - 1\right)\frac{dJ}{dt} \tag{3.26}$$

For soft magnetic materials, the magnetic induction intensity is almost equal to the magnetic polarization intensity, that is, a certain simplification can be obtained:

$$P_{\text{exc}} \cong \sqrt{\sigma GSV_0}\left(\frac{dB}{dt}\right)^{3/2} \qquad \text{when} \quad \frac{4\sigma GS}{n_0^2 V_0}\frac{dJ}{dt} >> 1 \tag{3.27}$$

Excess energy loss is:

$$W_{\text{exc}} = P_{\text{exc}} t \cong \sqrt{\sigma GSV_0}\int_0^{1/f}\left(\frac{dB}{dt}\right)^{3/2} dt \tag{3.28}$$

When the condition cannot satisfied $\frac{4\sigma GS}{n_0^2 V_0}\frac{dJ}{dt} >> 1$ [39]

$$\begin{aligned} W_{exc} &= 2n_0 V_0 B_p \cdot \int_0^{2\pi}\left(\sqrt{1+\frac{8\sigma GS}{n_0^2 V_0}\pi f B_p \cos\theta} - 1\right)\cos\theta d\theta \\ &\cong (8.76/8)\cdot 2n_0 V_0 B_{\text{p}} \cdot \left(\sqrt{1+\frac{16\sigma GS}{n_0^2 V_0} f B_{\text{p}}} - 1\right) \end{aligned} \tag{3.29}$$

The specific steps of loss separation are as follows: firstly, total loss is measured; secondly, hysteresis loss is deduced according to the linearity when the distribution of magnetic induction intensity is not uniform; thirdly, classical loss is calculated according to the appropriate model. Fourthly, according to the experimental results, the most suitable parameters n_0 and V_0 are found according to the method mentioned above, and the excess loss is predicted by using formula (3.28) or (3.29). Figure 3.3 shows the results of loss separation of 0.194 mm thick non-oriented silicon steel sheets under 0.05T excitation. Points are measured and lines are calculated.

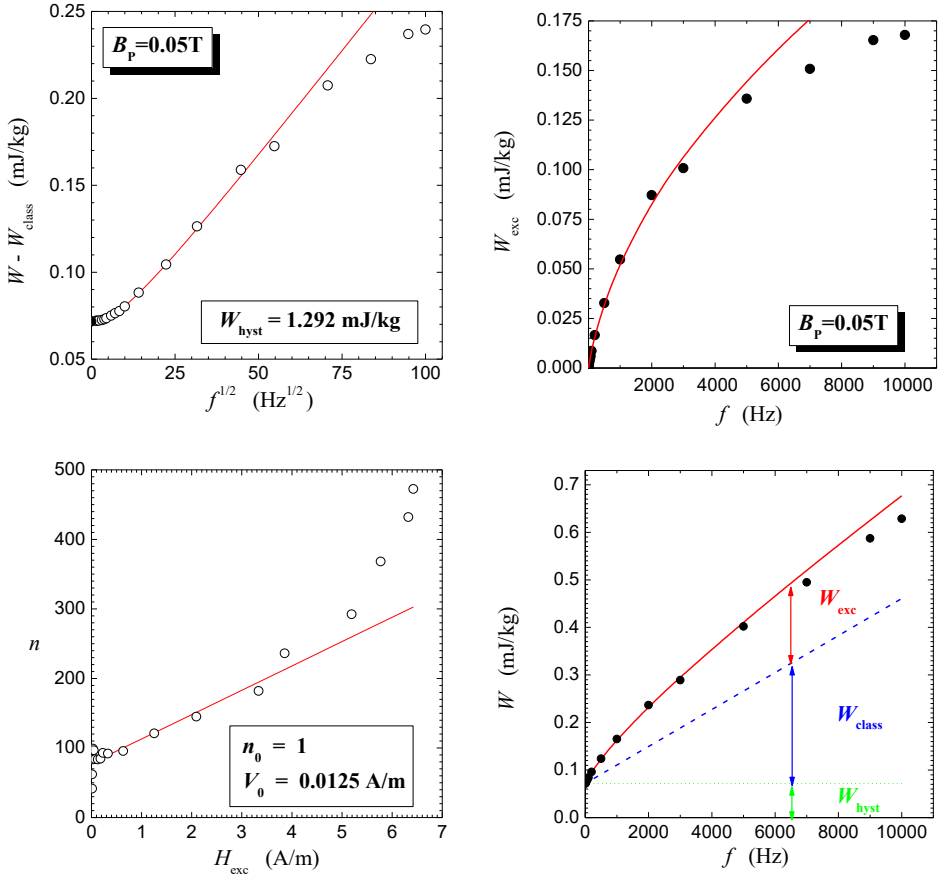

Figure 3.3: Loss Separation Result of 0.194 mm Thickness Non-oriented Silicon Steel Sheet under 0.05T Excitation

Chapter 4

Experimental Techniques and measurements setups

4.1 Measurement Apparatus

Research on magnetic materials magnetic properties require the measurement of magnetic field (H) and magnetic flux density(B). The measurement usually take place in specific apparatus and the classical method is fluxmetric approach. This chapter will introduce experimental techniques and the whole measurement system. Usually, in order to reveal and measure a magnetic field, we should create closed magnetic circuits. According to the Faraday-Maxwell law of electromagnetic induction, electromotive force is detected proportional to the time derivative of the flux. Upon time integration, the magnetization in the core ensuing from a variation of the applied field is computed. In soft magnetic materials, the term $\mu_0 H$ is negiligible with respect to J. So in this thesis, we assume that $B_p \approx J_p$.

The wattmeter-hysteresisgraph apparatus [40] is applied. This set up can be satisfied with different shape of the sample, employed different kinds of magnetizers (Epstein frame, Single sheet Tester, Ring sample). A scheme of the hysteresisgarph is given in Figure 4.1. The input waveform is generated by a functional signal generator (Agilent 33220A). The signal is amplified by a power amplifier (NF-HSA4101). This waveform is driven the primary coil of the magnetizer. The voltage dropped u_H is measured using a calibrated resistor R_H. So, the magnetizing current is $i_H = u_H / R_H$. Then the magnetic field strength is

$$H(t) = \frac{1}{G_H} \frac{N_{in}}{l_m} i_H(t) \tag{4.6}$$

G_H is the low-noise pre-amplifier gain. This pre-amplifier is employed for amplifying the measuring signal and deduce the noise of the output signal. N_1 is the number of the primary coil turns. l_m is the magnetic path length. Different types of magnetizer have different l_m. The flux density B is obtained by the induced voltage in the secondary coil of the magnetizer.

$$B(t) = \int \frac{1}{G_B} \frac{1}{N_2 A} u_B(t) dt \tag{4.7}$$

This signal is amplified by another low-noise pre-amplifier which gain is G_B and fed into the digital oscilloscope (LeCroy4054A) for measurement. N_2 is the number of the secondary coil turns. A is the cross-section area of the sample.

The digital oscilloscope (LeCroy4054A) can obtain simultaneous acquisitions of both signals. The signals are calculated by PC. The energy loss is

$$W = \frac{1}{G_B A N_2} \int_0^T u_B \cdot i_H dt \qquad [J/m^3] \tag{4.8}$$

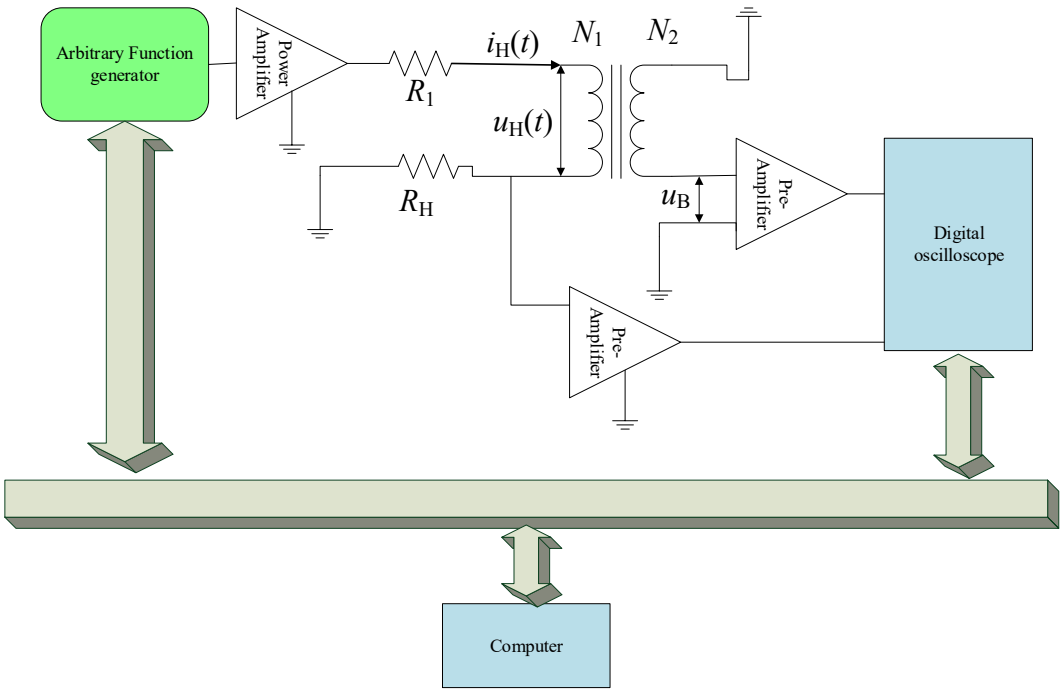

Figure 4.1: The wattmeter-hysteresisgraph developed by Fiorillo and co-workers at INRIM. The system implements digital control of the waveform of dB/dt by an iterative process. Samples such as Epstein strips, SST and ring samples can be employed in the system.

One dimensional measurement standard of soft magnetic material already established. Epstein test method is widely adopted by industry standard. The standard IEC 60404-2 [41] deals with the measurements on steel sheets using the Epstein magnetizer from DC-400Hz. In this thesis, I adopted 200 turns Epstein frame instead of 400 turns Epstein frame according to Standard IEC 60404-10 [42]. The strip/single-sheet tester (SST) is developed for more accurate measurement. Now the SST is adopted in the IEC 60404-3 [43] standard. According to IEC 60404-6 [44], Methods of measurement of the magnetic properties of magnetically soft metallic and powder materials at frequencies in the range 20 Hz to 100 kHz of ring specimens are specified. Figure 4.2, Figure 4.3 and Figure 4.4 show the actual Epstein frame, SST tester and ring sample.

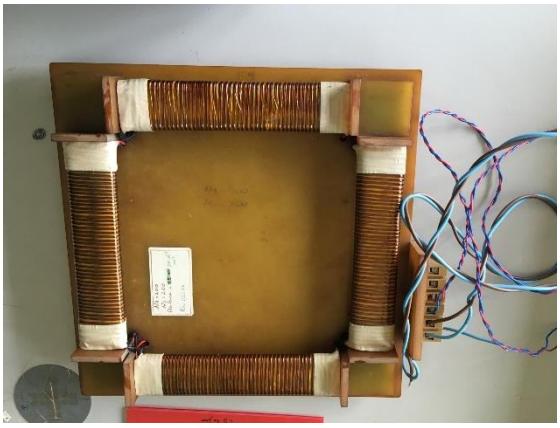

Figure 4.2: 200 turns Epstein frame

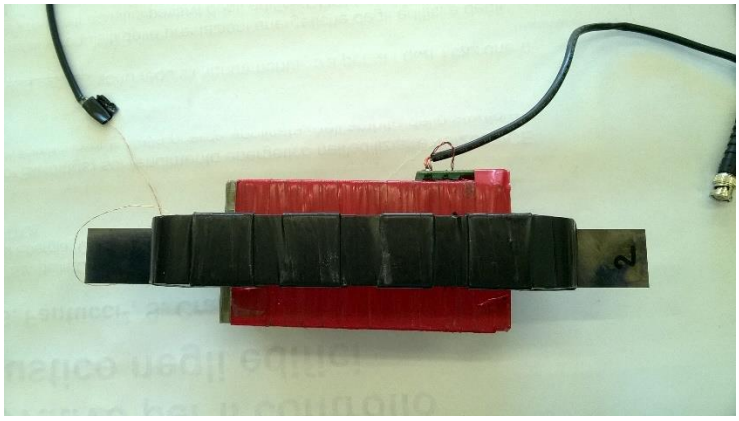

Figure 4.3: The Strip Single Tester

Figure 4.4: The Ring Sample

Two-dimensional and three-dimensional measurement equipment are developing in these years. However, due to the complex of the measurement procedure, there are still no standard. Here is not elaborated apparatus of two and three dimensional, because the main research here evolved only one-dimensional measurement.

These apparatuses are applicable at low and medium high frequency. When the frequency increase to Mhz. The method should change. Here we introduce the transmission line method. The measurement frequency band of transmission line method is from quasi-static to MHz. For accurate measurement of Ferrite and nanocrystalline tape-wound sample. We applied the measurement system shown in Figure 4.5 as much high frequency as it can, then we use transmission line method at very high frequency. It is necessary to pay attention to the minimum spurious parameters guaranteed by the primary and secondary coils, the overall layout and the related wires in order to ensure the accuracy of the experiment. The measurement of high frequency band is from Mhz to 100MHz. This band is measured by transmission line method and vector network analyzer (VNA) Agilent 8753A. The experimental schematic diagram [40] is shown in Figure 4.6.

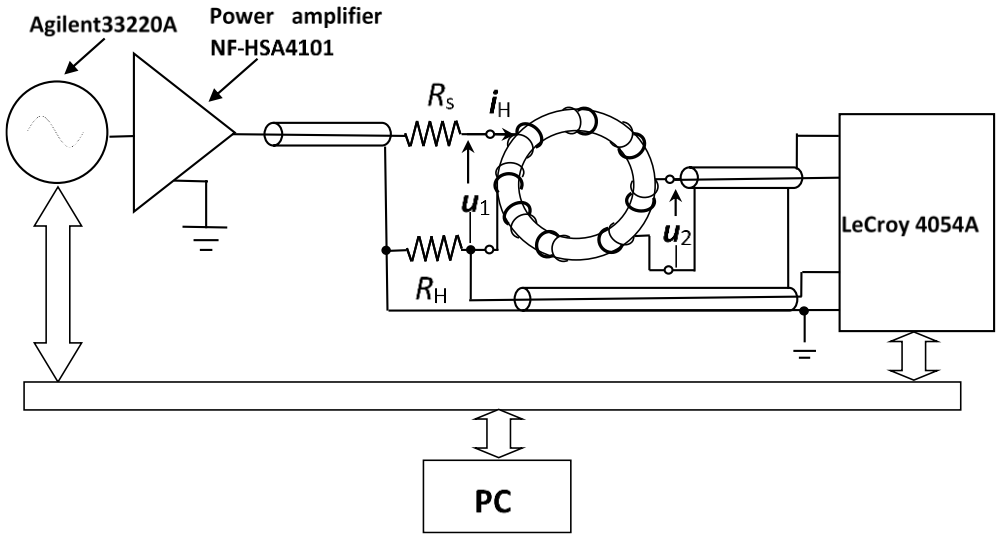

Figure 4.5: The Ring Sample measurement system

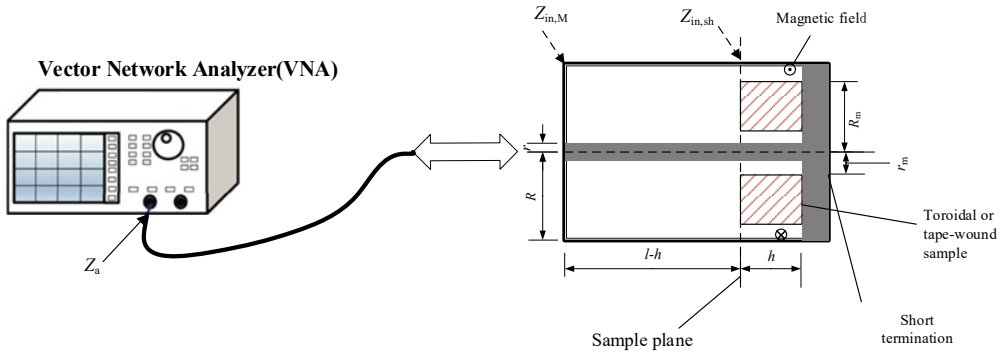

Figure 4.6: High frequency measurement system

The Vector Network Analyzer is both a signal source and a signal collector. Firstly, the reflection coefficient $S_{11}(f)$ of the short-circuit coaxial characteristic resistance Z_0 is measured, and the test sample is placed at the short-circuit end. The relationship between the reflection coefficient $S_{11}(f)$and the resistance $Z_{sh}(f)$ is as follows

$$Z_{\mathrm{sh}}(f) = Z_0 \frac{1+S_{11}(f)}{1-S_{11}(f)} \tag{4.9}$$

If the sample thickness h is less than 1/4 of the electromagnetic field wavelength coefficient $h<<\lambda/4$, the dielectric effect can be neglected, and the relationship between the short-circuit coaxial characteristic resistance Z_0 and $Z_{\mathrm{sh}}(f)$ is

$$Z_{\mathrm{sh}}(f) = jZ_0 \tanh(\beta h) \approx jZ_0 \beta h \tag{4.10}$$

$\beta=\omega\sqrt{LC}$ is the propagation constant of the transmission line (phase change of electromagnetic waves per unit length). Because $Z_0 = \sqrt{L/C}$, so $Z_{\mathrm{sh}}(f) \approx j\omega Lh$,according to Figure 4.6:

$$Z_{\mathrm{sh}} = j\omega \frac{\mu}{2\pi} h \cdot \ln \frac{R}{r} \tag{4.11}$$

If a magnetic ring sample is placed, the complex permeability is: $\mu=\mu_0\mu_r'\text{-}j\mu_0\mu_r''$

$$Z_{\mathrm{sh}} = j\omega \frac{\mu_0}{2\pi} \ln \frac{R}{r} \cdot h \cdot (\mu_r'\text{-}j\mu_r'') \tag{4.12}$$

The resistance portion is related to the magnetic loss. When $R_{\mathrm{m}} \le R$ and $r_{\mathrm{m}} \ge r$, Z_{sh} is the ring sample (Rm, rm) and the resistance of the remaining air. Measure $Z_{\mathrm{in,sh}}$ resistance twice, added and not added the sample respectively. The difference between these two $\Delta Z = \mathrm{re}\{\Delta Z_{\mathrm{sh}}\} + j\mathrm{im}\{\Delta Z_{\mathrm{sh}}\}$ .The the real number and the complex permeability can be obtained:

$$\begin{aligned} \mu_{\mathrm{r}}' &= 1 + \mathrm{im}\{\Delta Z_{\mathrm{sh}}\} \Big/ (\omega \frac{\mu_0}{2\pi} h \cdot \ln \frac{R_{\mathrm{m}}}{r_{\mathrm{m}}}) \\ \mu_{\mathrm{r}}'' &= \mathrm{re}\{\Delta Z_{\mathrm{sh}}\} \Big/ (\omega \frac{\mu_0}{2\pi} h \cdot \ln \frac{R_{\mathrm{m}}}{r_{\mathrm{m}}}) \end{aligned} \tag{4.13}$$

This approximation of the complex permeability can only be limited to a certain power and sinusoidal waveform. However, through the previous measurements, Mn-Zn ferrites excited below 100 mT and nanocrystalline ribbon excited below 500 mT, the complex permeability is independent of the peak of the magnetic induction at a frequency close to the MHz. Fluxmetric method measured permeability overlaps with the magnetic permeability measured by the transmission line at certain frequency range. According to following equation ,we can obtain the magnetic loss:

$$W(B_{\mathrm{p}}, f) = \pi B_p^2 \frac{\mu''}{\mu'^2 + \mu''^2} \tag{4.14}$$

4.2 Control of the induction waveform by digital feedback

There are mainly two methods of implementing digital feedback. One consists of trying to emulate by computation the real-time control of the sample magnetization realized by computation the real-time control of the sample magnetization by means of analogy feedback. The other in programming the suitable time dependence of the magnetizing current by iterative augmentation of the input using an inverse approach. Computing requirements pose the basic limitation to the feedback chain bandwidth in real-time control. The following steps: (1) Acquisition at given instants of time, separated by conveniently small intervals, and A/D conversion of a reference signal, describing the desired dB/dt waveform, and of the actual measured waveform. (2) Comparison of these two signals and computation, by means of a regulation algorithm, of the correct value of the magnetizing current, taking into account the composition of the primary circuit and (3) Digital to analogy conversion and generation of the calculated current. This apparatus can be carried out as shown in Figure. The scheme of the general structure of a computer-controlled digital wattermeter-hysteresisgraph apparatus.

Chapter 5

Loss decomposition in non-oriented steel sheets: Role of the classical losses

5.1 Introduction and Motivation

The fundamental theory of the classical loss is explained in Chapter 3. It influences the whole loss separation based on STL. As the application for the steel sheets are requested in middle high frequency, it is much more important for engineers to predict steel sheet's total loss in a broadband frequency. For the calculation of the energy losses in non-oriented steel sheets, a simple standard formula for the classical loss is under the assumption of ignoring skin effect and uniform magnetization reversal through the sheet cross-section. However, this model has been challenged in the literature. In practical cases, due to the steel sheets laminations and the nearly saturation induction working condition, some researchers[45] proposed that the well-known simplified classical loss expression

is underestimated, which causes the overestimates of the excess loss in non-oriented steel sheets. To validate different models and to summarize the role of the classical loss, I conducted experiments and the whole loss separation analysis on non-oriented Fe-Si and low-carbon steel sheets through a broadband frequency.

5.2 The uniform induction model versus the saturation wave model

The crucial problem is the fact how to accurate proceed the loss separation at broadband frequency. In order to be much clearer about the problem, I summarize the classical loss models as following:

In order to address this problem, there are three important issue involved. One is magnetic material, considering material constitutive law, especially its intrinsic non-linearity. One is the amplitude of the induction and the last one is frequency.

According to STL, the classical loss is associated with the dissipation of regular macroscopic eddy current. It could be deducted from the diffusion of the currents localized at the moving domain walls [33]. The steel sheet sample geometry is showed in Figure 5.1. Under sinusoidal induction of peak value B_p at frequency f in a sheet of conductivity σ and thickness d, we apply Maxwell equation and following boundary conditions, we obtain

$$W_{class}(f)=P_{class}/f=\left(\frac{\pi^2}{6}\right)\sigma d^2 B_p{}^2 f \qquad [\mathrm{J/m^3}] \qquad (5.1)$$

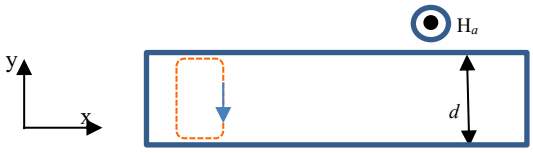

Figure 5.7: the sample geometry parameters. Here d is the thickness along y axis. The sample is assumed infinitely long and the external field is applied along z axis.

The material is considered homogeneous, so ignoring material constitutive law. The formula can only apply before emerging the skin effect. However, at very low induction, there is a linear approximation of the constitutive law ($\vec{B} = \mu\vec{H}$). The solution of Maxwell's equations can be solved without resorting to numerical analysis.

5.2.1 Arbitrary frequency, linear magnetization law, and low induction case

According to Rayleigh law, at low-field magnetization case, a linear approximation of the material constitutive law ($\vec{B} = \mu\vec{H}$) can be accepted, magnetic permeability $\mu = \frac{B_p}{H_p}$ is a constant. Hp is the peak value of magnetic field. For instant, Figure 5.2 shows the hysteresis loop of a non-oriented Fe-(3.2wt%) Si steel sheet at B_p = 0.1 T at 5 Hz, where a constant relative permeability of μ = 5400 can be approximated.

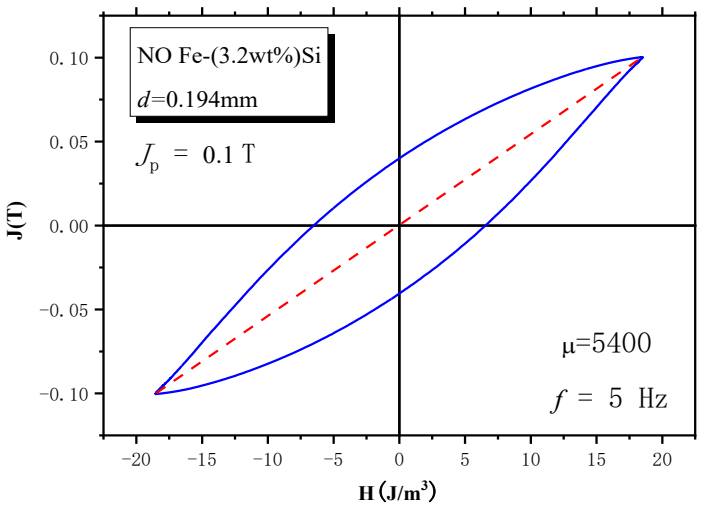

Figure 5.8: B-H loop of a non-oriented Fe-(3.2wt%)Si steel sheet, thickness d=0.194mm, at peak induction 0.1 T and *f*=5Hz.

In this case, we can solve magnetic diffusion equation. Let's deduct this formula from Maxwell equation. The geometry parameter is showed as Figure 5.1. The magnetic field is induced along the z-axis. So Maxwell equation Eq. 5.2 and Eq. 5.3 can be specified to Eq. 5.4 and Eq. 5.5

$$\nabla \times H = J \tag{5.2}$$

$$\nabla \times E = -\frac{\partial B}{\partial t} \tag{5.3}$$

$$\frac{\partial H}{\partial y} = J \tag{5.4}$$

$$\frac{\partial J}{\partial y} = \sigma \frac{\partial B}{\partial t} \tag{5.5}$$

Where σ is the conductivity of the material, and $H = H_z(y,t)$ is the instantaneous magnetic field strength and $B = B_z(y,t)$ magnetic induction, respectively, after deriving Eq. 5.4 and combining with Eq. 5.5, we obtain

$$\frac{\partial^2 H}{\partial y^2} = \sigma \frac{\partial B}{\partial t} \tag{5.6}$$

Approximated constitutive equation $B = \mu H$, we get

$$\frac{\partial^2 H}{\partial y^2} = \sigma\mu \frac{\partial H}{\partial t} \tag{5.7}$$

Under sinusoidal regime, we can introduce complex quantities. $H = |H| e^{jwt}$ We can obtain

$$\frac{\partial^2 H}{\partial y^2} = j\omega\sigma\mu |H| \tag{5.8}$$

The boundary conditions as following

$$\frac{\partial H}{\partial y}|_{y=0} = 0 \tag{5.9}$$

$$\frac{\partial H}{\partial y}\Big|_{y=\frac{d}{2}} = j\omega\sigma \frac{d}{2} |\bar{B}| \tag{5.10}$$

Where $|\bar{B}|$ is the average of the amplitude of B

In this case, we can solve this diffusion equation. The result of the classical loss as

$$W_{\text{class}}(f)=\frac{\pi}{2}\cdot\frac{\lambda B_p^2}{\mu}\cdot\frac{\sinh\lambda-\sin\lambda}{\cosh\lambda-\cos\lambda},\quad [\text{J/m}^3] \tag{5.11}$$

Where we introduce a dimensionless parameter

$$\lambda=\sqrt{\pi\sigma\mu fd^2} \tag{5.12}$$

If $\lambda=d/\delta\approx\leq 2$ Eq.5.12 is reduced to Eq. 5.1. B_p is the peak induction value.

5.2.2 Arbitrary frequency, step-like magnetization, and high induction case (Saturation Wave Model (SWM))

At high induction, the crucial factor, material constitutive law, should be considered. The material constitutive law is quite different from the low induction case. From the observation of the experiments data, we can assume the magnetization law of the material is the step-like as the black dash line in Fig. 5.3,

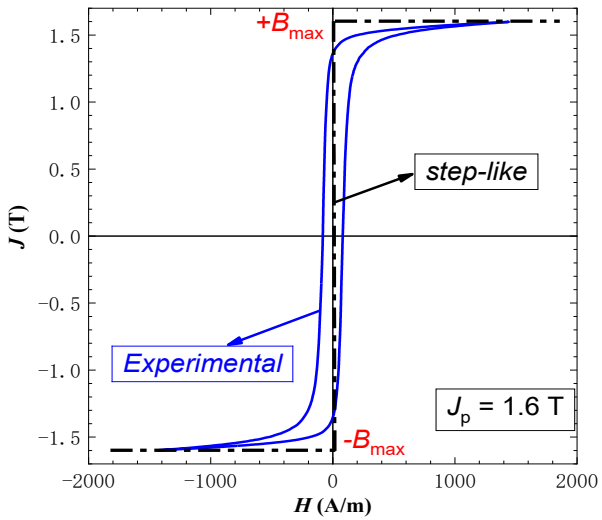

Figure 5.9: Low-carbon steel sheets at 1.6T, J-H loop, and the dash black line is the step-like approximation of the blue one.

$B=\pm B_{max.}$ This approximation of the magnetization is ideal. If *B-H* following this law, the magnetization changes in a certain portion of the slab cross-section only when *H*=0 everywhere inside it. However, this is not possible, because, according to Maxwell equation, *H*=0 means *J*=0, which can only be the case if $\partial B/\partial t = 0$.So, we know that the magnetization can only change in correspondence of one-dimensional fronts propagating across the slab. Due to the symmetry of the problem, these fronts will be parallel to the slab surface, as shown in Fig. 5.4.

It is the layer-by-layer flux reversal originally described in Wolman [46], the

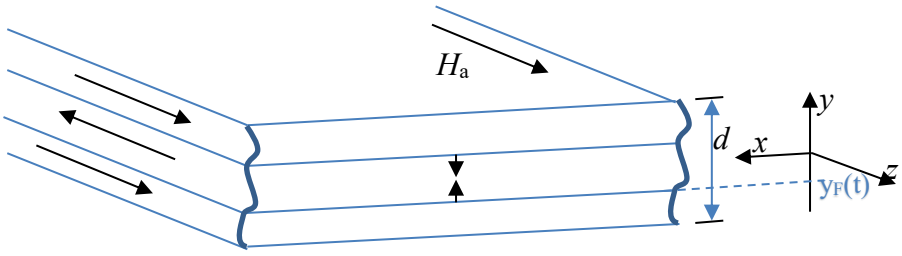

Figure 5.10: Propagating fronts in magnetic materials observing step-like magnetization law.

so-called saturation wave model (SWM). Let deduct the calculation of this model. In each half-period two symmetric fronts originate at the slab surface and propagate inward until they reach the center of the slab, where they annihilated. There is a direct quantitative correspondence between the position $y_F(t)$ of the fronts and the instantaneous value of the average induction *B*(t) in the slab cross-section. Here the analysis is restricted to the case where $B_p=B_{max.}$ In fact $y_F(t) = \pm\frac{d}{4}[\frac{B(t)}{B_{max}} - 1]$, when B is increasing. And $y_F(t) = \mp\frac{d}{4}[\frac{B(t)}{B_{max}} + 1]$, when B is decreasing. Due to the symmetry between the two fronts, we can limit the analysis to the region where ($-d/2 < y < 0$). Applying Faraday's law, we obtain,

$$J(y,t)=\begin{cases}-\dfrac{\sigma d}{2}\cdot\dfrac{dB}{dt} & -d/2\le y\le y_F(t)\\ 0 & y_F(t)<y\le 0\end{cases} \tag{5.13}$$

Integrate Eq.5.13 with respect to y, we obtained

$$H(y,t)=\begin{cases}-\dfrac{\sigma d}{2}\cdot\dfrac{dB}{dt}[y_F(t)-y] & -d/2\le y\le y_F(t)\\ 0 & y_F(t)<y\le 0\end{cases} \tag{5.14}$$

Add boundary conditions

$$H(y,t)\Big|_{y=\pm\frac{d}{2}}=H_{\mathrm{a}}(t) \tag{5.15}$$

Where $H_{\mathrm{a}}(t)$ is the applied field. According to the equations mentioned before, we obtain the following magnetization law:

$$H_{\mathrm{a}}(t)=\frac{\sigma d^2}{8}\left[\left|\frac{dB}{dt}\right|\frac{B(t)}{B_p}+\frac{dB}{dt}\right] \tag{5.16}$$

Energy loss per unit cycle is

$$W_{\mathrm{class}}^{(\mathrm{SWM})}=\frac{P_{\mathrm{class}}^{(\mathrm{SWM})}}{f}=\int_0^{1/f}H_a\frac{dB}{dt}dt \tag{5.17}$$

Under sinusoidal regime Eq.5.17 becomes

$$W_{\mathrm{class}}^{(\mathrm{SWM})}=\frac{\pi^2}{4}\sigma d^2B_{\mathrm{p}}^2f=\frac{3}{2}\cdot\frac{\pi^2}{6}\sigma d^2B_{\mathrm{p}}^2f=1.5W_{\mathrm{class}}(f) \tag{5.18}$$

From observation of this formula, SWM model estimates classical loss much greater than the loss obtained under uniform induction (Eq.5.1).

Up to now, I summarized all the models that I will validate using experiments data of non-oriented steel sheets. To clarify the issue, I performed and analyzed measurements on NO Fe-Si and low-carbon steel (LCS) sheets at low and high B_p amplitude.

5.3 Experiments

The issue here is to explore which model is much more suitable for the classical loss component. The samples I need should have large classical loss material to clarify this problem. Classical loss is the macroscopic eddy current. If classical loss is large, the material should have relatively large resistivity. Energy losses are measured from quasi-static up to 10 kHz at different peak polarization J_p in non-oriented Fe-Si and Low carbon steel sheets listed in Table 5.1. These samples have chosen for their different resistivity and thickness. Especially, the Low carbo steel sample could emulate a step-like response as showed in Fig.5.3.

Table 5.1: The list of non-oriented and low carbon steel sheets

Material	**(NO) Fe-Si-1**	**(NO) Fe-Si-2**	**LCS-1**	**LCS-2**	**LCS-3**
Sample shape	Epstein	Epstein	Epstein	Ring	Epstein
Density(kg/m^3)	7650	7600	7850	7860	7870
Resistivity(Ω•m)	56×10^{-8}	52×10^{-8}	19.2×10^{-8}	15.3×10^{-8}	12×10^{-8}
Thickness(mm)	0.194	0.345	0.506	0.507	0.636

The samples have been measured either as Epstein strips or Ring samples for comparison. These samples have been measured by a calibrated wattmeter-

hysteresisgraph under controlled sinusoidal induction, and experiments procedures are elaborated in Chapter 4.

5.4 Results and discussion

Epstein strips and ring samples, either non-oriented or low carbon steel sheets are tested. I obtained a lot of experimental results and data. Some of them are elaborated and discussed in the following section.

5.4.1 Energy Loss at Low Inductions

The magnetic energy loss has been measured at B_p=0.1T and B_p=0.2T and frequency ranging from quasi-static conditions up to 10 kHz. Let us take 0.194mm Fe-(3.2 wt%)Si sheet at B_p=0.1T case for example. Figure 5.5 shows the total loss decomposed into its three components, hysteresis loss W_{hyst}, classical loss W_{class}, excess loss W_{exc}. The classical loss W_{class} calculated using Eq. 5.1. The hysteresis component W_{hyst} is obtained by extrapolating $W_{total}(f)$ to f = 0.The excess loss W_{exc} is described by the theoretical law [39]. The details are discussed in Chapter 3.

$$W_{exc}(f) = \sqrt{\sigma GSV_o}\int_0^T \left|\dot{J}(t)\right|^{3/2} dt \tag{5.19}$$

$$W_{exc}(f) = 2n_0 V_0 J_p \cdot \int_0^{\pi/2} \left(\sqrt{1+\frac{8\sigma GSV_0}{n_0^2 V_0^2}\pi f J_p \cos\beta} - 1 \right) \cos\beta d\beta \tag{5.20}$$

The total loss obtained from the three components

$$W_{total}(f) = W_{hyst} + W_{class} + W_{exc} \tag{5.21}$$

$W_{exc}(f)$ complies upon the part of the investigated frequency range (before emerging the skin effect)with the theoretically assumed linear dependence $n = n_0$

+ H_{exc}/V_0 of the number n of active magnetic objects (MOs) on the excess field $H_{exc} = W_{exc}/4J_p$ as illustrated in Figure. 5.6. The quantity V_0 lumps the effect of the local coercive fields and the experimental n values are obtained as $n = 4\sigma GSJ_p / H_{exc}$, with G = 0.1356 and S the sample cross-sectional area [33]. With the so-obtained V_0 parameters, the experimental $W_{exc}(f)$ behavior and calculation value are compared in Figure. 5.7.

From the observation of Figure5.5-5.7, 0.194mm Fe-(3.2wt%) steel sheet's skin effect emerge around from f_c=4kHz at B_p=0.1T.

Then let us compare with $n = 4\sigma GSJ_p / H_{exc}$ another classical loss model considering skin effect. The DC hysteresis loop at this low J_p=0.1T value is described by the Rayleigh law, where the permeability $\mu = J_p / H_p$ coincides with the differential permeability averaged upon a loop branch between $\pm J_p$ (relative $\mu_r = 5400$ at J_p=0.1T). So, I can confidently using Eq. 5.11 to obtain $W_{class}(f)$, The hysteresis loss W_{hyst} and W_{exc} are obtained using the same method as before. The loss separation is illustrated in Figure. 5.8. Different from the last calculation, we can remarkably find $W_{exc}(f)$ complied upon the whole investigate frequency band with the theoretically assumed linear dependence $n = n_0 + H_{exc}/V_0$ of the number n of active magnetic objects (MOs) on the excess field $H_{exc} = W_{exc}/4J_p$, as shown in Figure. 5.9. The quantity V_0 lumps the effect of the local coercive fields and the experimental n values are obtained as, with G = 0.1356 and S the sample cross-sectional area. With the so-obtained n_0 and V_0 parameters, the experimental $W_{exc}(f)$ behavior and calculation value are compared in Figure. 5.10.

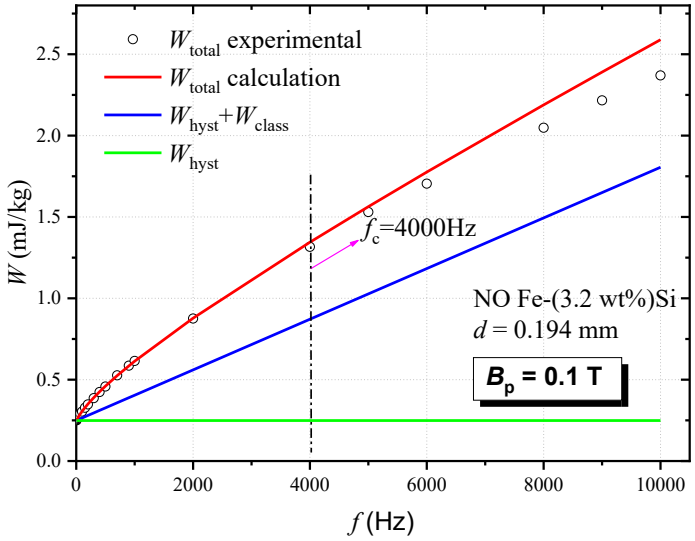

Figure 5.11: NO Fe-(3.2 wt%Si) 0.194 mm thick sheets. Decomposition of the measured energy loss (symbols) at B_p = 0.1 T up to 10 kHz. The classical loss $W_{class}(f)$ is calculated with Eq. 5.1, skin effect emerge around 4kHz.

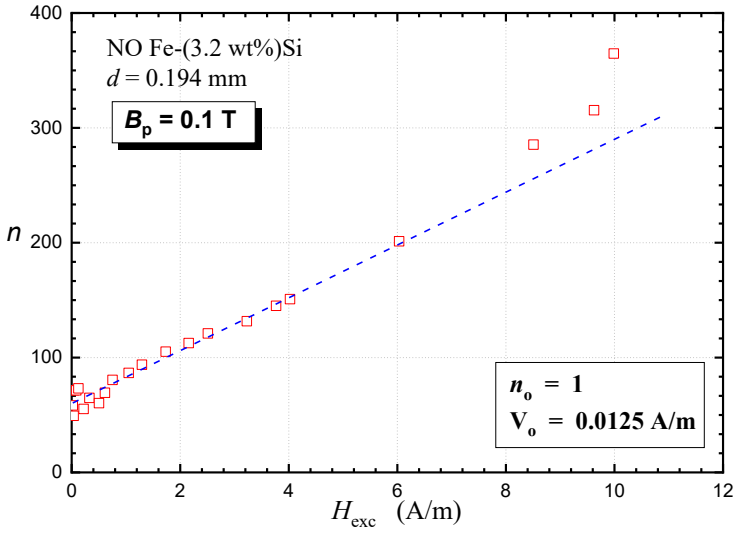

Figure 5.12: NO Fe-(3.2 wt%Si) 0.194 mm thick sheets. The number n, active magnetic objects (MOs), follows a linear dependence $n = n_0 + H_{exc}/V_0$ on $H_{exc} = W_{exc}/4J_p$.

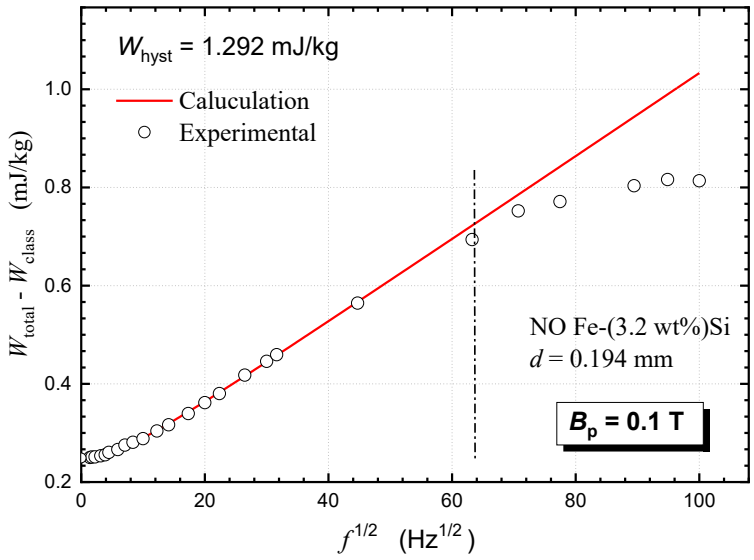

Figure 5.13: NO Fe-(3.2 wt%Si) 0.194 mm thick sheets. The quantity $W_{diff}=W_{total}-W_{class}$ is plotted versus the square root of frequency up to f = 10 kHz (open circles). The same quantity W_{diff} is then computed theoretically as $W_{diff} = W_{hyst} + W_{exc}$, where W_{exc} is obtained through Eq. 5.20 (red lines).

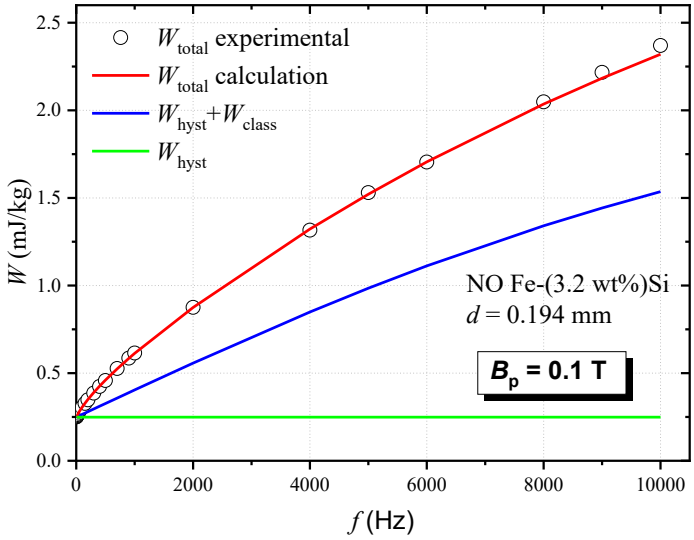

Figure 5.14: Non-Oriented Fe-(3.2 wt%Si) 0.194 mm thick sheets. Decomposition of the measured energy loss (symbols) at B_p = 0.1 T up to 10 kHz. The classical loss $W_{class}(f)$ is calculated with Eq. 5.11, taking into account the skin effect.

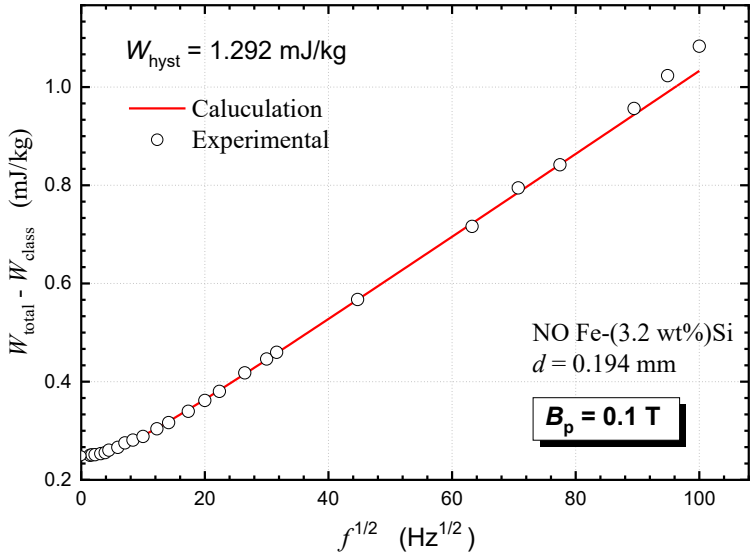

Figure 5.15: NO Fe-(3.2 wt%Si) 0.194 mm thick sheets. The quantity $W_{diff}=W_{total}-W_{class}$ is plotted versus the square root of frequency up to f = 10 kHz (open circles). The same quantity W_{diff} is then computed theoretically as $W_{diff} = W_{hyst} + W_{exc}$, where W_{exc} is obtained through Eq. 5.20 (red lines).

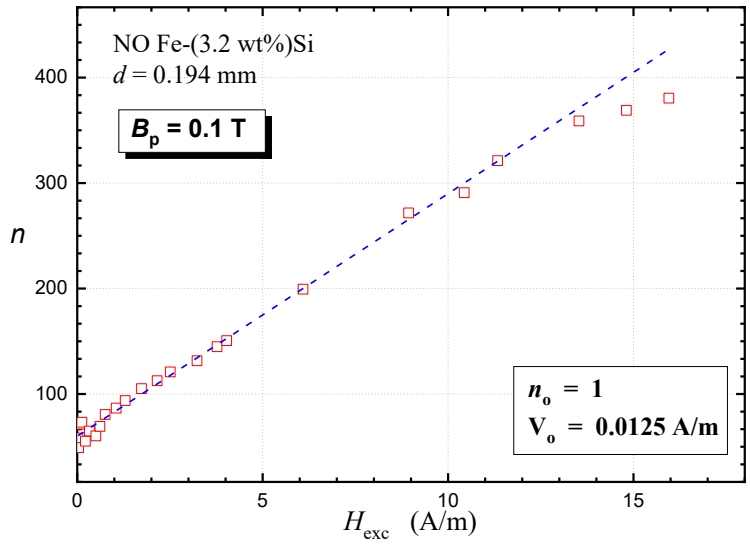

Figure 5.16: NO Fe-(3.2 wt%Si) 0.194 mm thick sheets. The number n, active magnetic objects (MOs), follows a linear dependence $n = n_0 + H_{exc}/V_0$ on $H_{exc} = W_{exc}/4J_p$.

5.4.2 Energy Loss at High Inductions

The three LCS samples are chosen to test at J_p=1.6T to verify the SWM (Eq.5.18). Figure.5.11 shows the quasi-static hysteresis loops in the three investigated LCS samples, where I noted again that for all practical purpose $B_p = J_p$. Because the LCS samples conductivity are high, the excess loss component is much lower than the classical loss. So the application of Eq.5.1 or Eq.5.11 could imply discrepancies between the correspondingly identified excess loss behaviors $W_{exc}(f)$. In order to comparison, all the measurements have been restricted to the region not affect by the skin effect. We cannot obviously make use of Eq.5.11, as previously done in the Rayleigh region. Because at high-induction, its non-linear material constitutive law is showed in Figure.5.11. But the STL provides a unique way to identify incipient skin effect. I apply the usual procedure, by subtracting $W_{total}(f) - W_{class}(f)$ with the classical loss calculated with Eq.5.1, ignoring the

skin effect, to obtain W_{hyst} by extrapolating $W_{total}(f)$ to $f = 0$ and $W_{exc}(f)$. By correspondingly finding the number n of MOs versus $H_{exc}(f) = W_{exc}/4J_p$, I realize that, contrary to the low-induction case shown in Fig.5.10, $n(H_{exc})$ only follow the linear relationship $n = n_0 + H_{exc}/V_0$ below a certain critical H_{exc} value. This translates into a divergence between the prediction of $W_{exc}(f)$ by Eq.5.20 and its actual behavior beyond a certain frequency, where the skin effect makes Eq.5.1 invalidate. The samples given in Figure.5.12, concerning the LCS 1 sample (d =0.506 mm) at J_p = 1.6 T, shows that in this case one can excellently fit the experimental $W_{exc}(f)$ with Eq.5.20 up to about $f \cong 80$ Hz, before emerging the skin effect. Figure.5.13 shows that the skin effect free region is around up to 500Hz in in LCS 2 and the free skin effect region in LCS 3 is around up to 300Hz shown in Figure.5.14. The larger the product of conductivity and permeability, the earlier the appearance of the skin effect. After decided the skin effect regions of the three LCS samples, I proceed the loss separation procedure with the classical loss calculated by using Eq.5.1 and Eq.5.18, where I assume, as before, the term $\mu_0 H_p$ negligible with respect to J_p and $B_{max}=B_p=J_p=1.6$T. The results are shown in Figure.5.15-5.17. All the classical loss calculated by SWM $W_{class}^{(SWM)}(f)$ overestimate the experimental total loss, leaving no room for the excess losses. These results contrast the idea that the very existence of moving domain walls and of the related localized eddy currents should always provide an extra-loss contribution, whatever assumption is made regarding the uniformity of the distribution of the flux density at low frequencies [47]. In other words, the results predicted by following the SWM model are not physical and the hypothesis of a step-like shape Figure.5.11 is not verified.

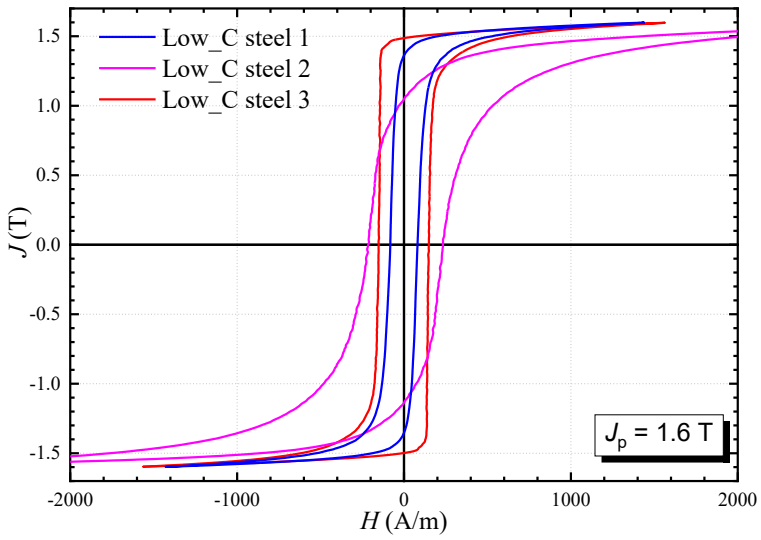

Figure 5.17: DC hysteresis loops at J_p = 1.6 T in the three investigated low-carbon steels (see Table 5.1).

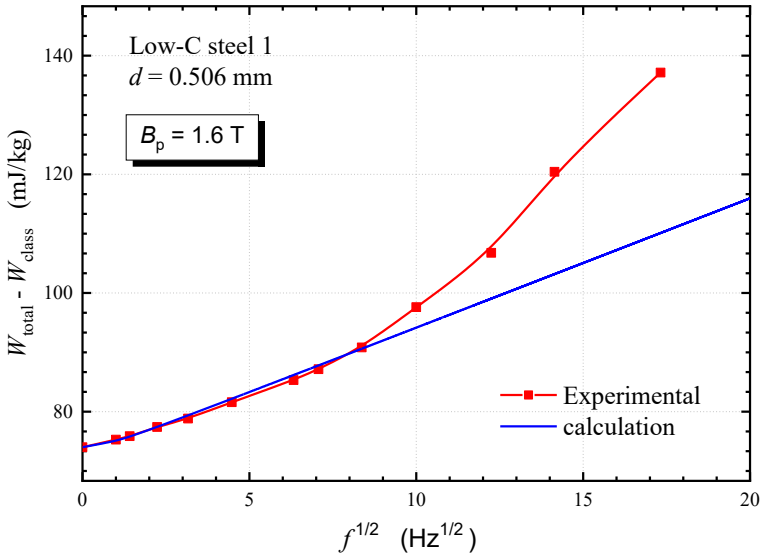

Figure 5.18: The quantity $W_{diff} = W_{total} - W_{class}$ versus $\sqrt{f}$ in 0.506 mm thick LCS-1 at B_p=1.6T (red line) and its theoretical counterpart $W_{diff} = W_{hyst} + W_{exc}$ (blue line) where Eq.5.20 has been applied to compute the excess loss. Deviation between the experimental and the theoretical results is observed at frequencies beyond 80 Hz due to the appearance of skin effect.

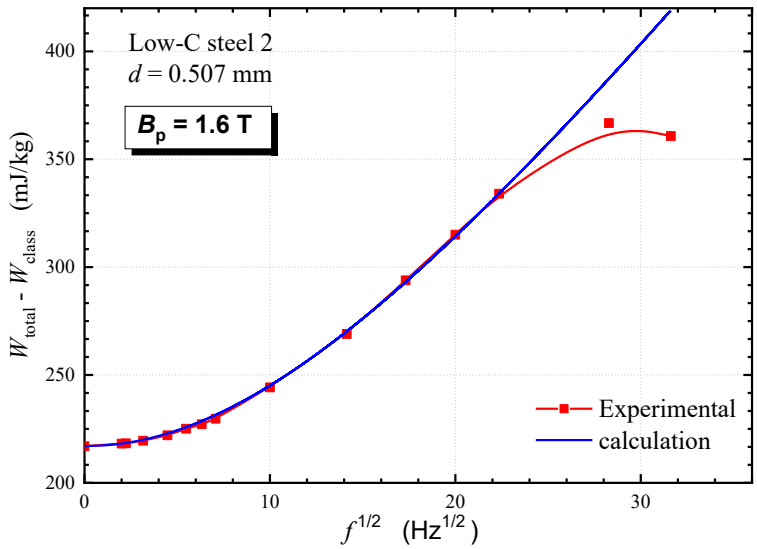

Figure 5.19: The quantity $W_{diff} = W_{total} - W_{class}$ versus $\sqrt{f}$ in 0.507 mm thick LCS-2 at B_p=1.6T (red line) and its theoretical counterpart $W_{diff} = W_{hyst} + W_{exc}$ (blue line) where Eq.5.20 has been applied to compute the excess loss. Deviation between the experimental and the theoretical results is observed at frequencies beyond 500 Hz due to the appearance of skin effect.

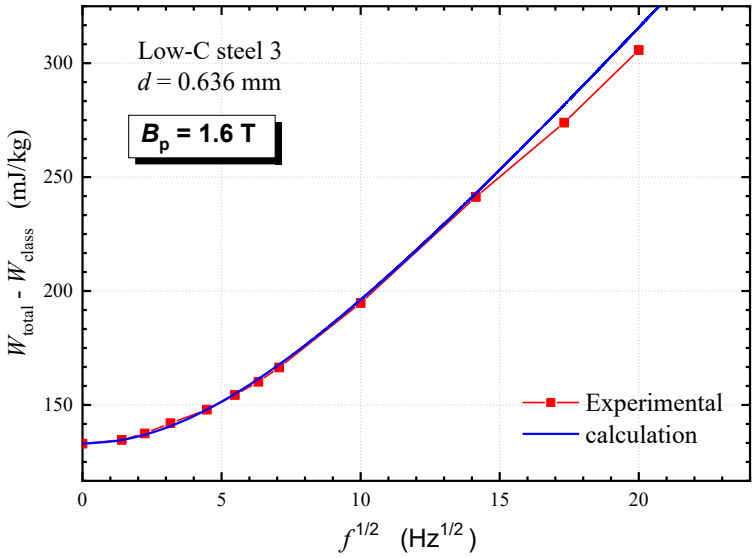

Figure 5.20: The quantity $W_{diff} = W_{total} - W_{class}$ versus $\sqrt{f}$ in 0.636 mm thick LCS-3 at B_p=1.6T (red line) and its theoretical counterpart $W_{diff} = W_{hyst} + W_{exc}$ (blue line) where Eq.5.20 has been applied to compute the excess loss. Deviation between the experimental and the theoretical results is observed at frequencies beyond 300 Hz due to the appearance of skin effect.

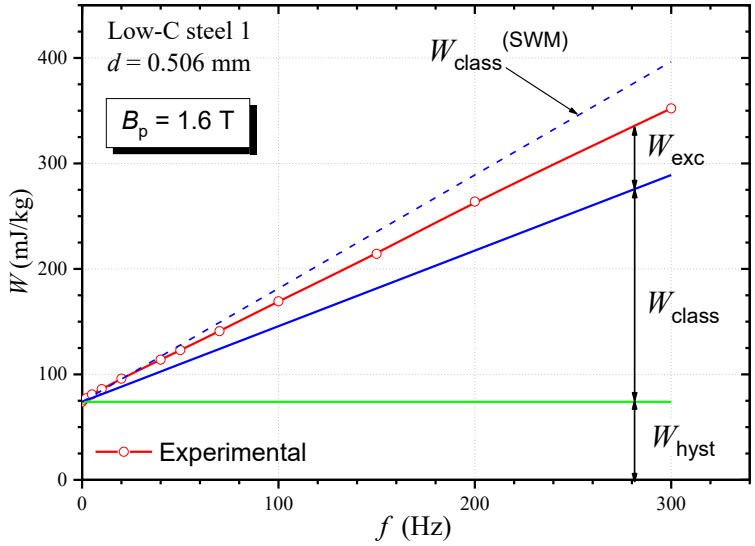

Figure 5.21: Decomposition of the energy loss measured at B_p = 1.6 T in the LCS-1 sample upon the skin-effect free frequency region. The classical loss W_{class} is obtained by (5.1). The dash-dot line is obtained by calculating the classical loss $W_{class}^{(SWM)}$ with (5.18), where $B_{max} = B_p$. $W_{class}^{(SWM)}$ overestimates the measured loss.

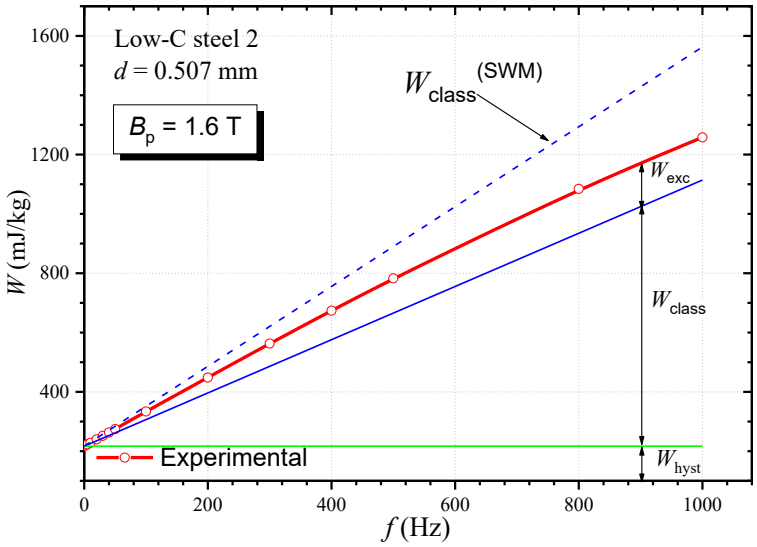

Figure 5.22: Decomposition of the energy loss measured at B_p = 1.6 T in the LCS-2 sample upon the skin-effect free frequency region. The classical loss W_{class} is obtained by (5.1). The dash-dot line is obtained by calculating the classical loss $W_{class}^{(SWM)}$ with (5.18), where $B_{max} = B_p$. $W_{class}^{(SWM)}$ overestimates the measured loss.

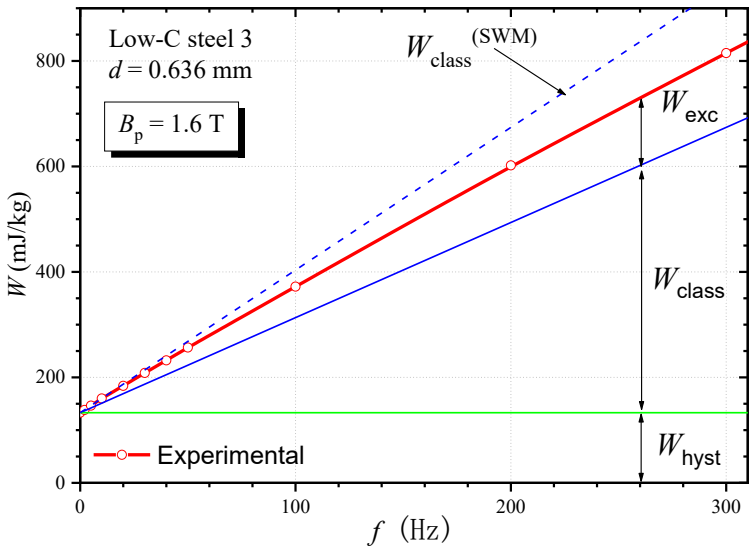

Figure 5.23: Decomposition of the energy loss measured at B_p = 1.6 T in the LCS-3 sample upon the skin-effect free frequency region. The classical loss W_{class} is obtained by (5.1). The dash-dot line is obtained by calculating the classical loss $W_{class}^{(SWM)}$ with (5.18), where $B_{max} = B_p$. $W_{class}^{(SWM)}$ overestimates the measured loss.

5.5 Conclusion

In this chapter, respect to the specific debate on the adoption of the classical loss model, I gave an overall analysis of the classical loss models. In order to validate the models, I conducted the experiments on different type of non-oriented Fe-Si. From the observation of the analysis of the experimental data, it is shown that magnetic energy losses can be assessed accurately at low and high induction using the concept of loss separation using statistic theory of loss (STL). In particular at low induction, Maxwell diffusion equation can be solved Eq (5.11) without resorting to numerical analysis. So considering the skin effect, Eq (5.11) can be verified up to 10kHz in 0.194mm Fe-(3.2wt%)Si. This is, in particular, achieved, within the constraints posed by the skin effect, assuming uniform reversal of the magnetization across the sheet cross-section at the macroscopic scale and corresponding standard formulation for the classical loss component. By making measurements at J_p = 1.6 T in low-carbon steels, one can put in evidence that the previous assumption still holds, although the $B(H)$ constitutive equation tends to emulate a step-like function. This would theoretically imply the occurrence of the magnetization reversal by inward motion of one-dimensional fronts. The ensuing formulation for the classical loss turns however to grossly overestimate the measured losses and can be ruled out.

Chapter 6

Measurement and Prediction of the Magnetic Losses with Minor Loops: two-level PWM Regime and the Limits of the Analytical Approach

6.1 Background and Introduction

Last Chapter, I give an overall description of the classical loss model which under the standard sinusoidal induction waveform. However, in practice, this is not always the case. For electromagnetic devices, magnetic cores or portions of the cores are induced to non-sinusoidal waveform. In some paper, there are discussions about the distorted waveform, which is different from the ideal sinusoidal condition caused by strong material nonlinearity at high inductions, anisotropy (T-joints of transformers), or pulsating waveforms (teeth of stator cores). For this matter, there are detailed solutions in litterateurs [48-49]. On the

other examples, like in high-speed electrical machines or inverters, most likely are supplied by Pulse Width Modulated (PWM) voltages, the driving circuit itself generates non-sinusoidal induction. Hence, magnetic material characterizations are crucial for the designers of electrical machines or power electronic transformers under these practical situations. Let's focus on the latter case, the Pulse Width Modulated voltage supply. This technology is prevalently to supply modern electrical machines because of the advantages offered by power electronics for driving the machines at their maximum efficiency on a wide speed range[39,48] . The fundamental frequency is typical in the kilohertz range, with carrier frequencies of several tens of kilohertz, for instant, the new SiC- or GaAs-based power transistors modules [51-52]. This PWM waveform introduces minor loops in the major hysteresis cycle. It complicates the calculation of the energy loss. Figure 6.1 shows an example of a PWM waveform and the associated major and minor hysteresis cycles, for a frequency modulation index of m_f=5. As shown in Figure 6.1, PWM waveform the minor loops nest in the major loop. Therefore, to calculate the total energy loss, the major loop and minor loops should be all considered. Prediction of the energy loss of soft magnetic loss under such non-conventional supply conditions has been investigated in the past, assuming negligible skin effect [49]. However, the present devices are utilized through a broadband frequency range. Kilohertz range can be found in the fundamental frequencies[50], with several tens of kilohertz carrier frequencies. Under these conditions, the dynamics of both the major loop and the minor loop is strongly influenced by the skin effect. Based on last chapter's approach, the classical loss related to cycles of small amplitude at high frequencies could be computed by assuming a linear magnetic constitutive equation for the material. In this way, the skin effect could easily be accounted for through a linear diffusion model. The loss separation analysis then could be proceeded correctly. And the excess loss versus the square root of frequency is a linear behaviour predicted by STL [33]. It could be suitable up to 10 kHz in non-oriented Fe-Si sheets. On the other hand, as

the frequency goes up, an increase of the hysteresis loss component could be assumed duet to the non-uniform induction profile across the sheet thickness infused by the skin effect. Hence, in order to address the difficulties with PWM supply conditions, I continue to work on loss modelling.

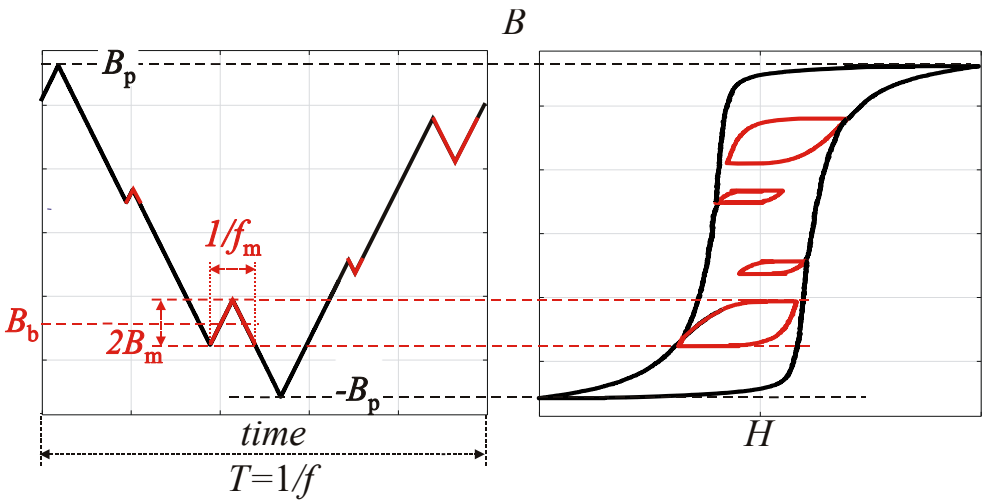

Figure 6.1: Example of PWM waveform and associated hysteresis cycles for a frequency modulation index of $m_f = 5$. The major loop is in black. The nested minor loops are in red and blue.

6.2 modelling the minor loops at high frequency and Experiments

The minor loops introduced by PWM waveforms shown in Figure 6.1 have low amplitude upon high frequencies. As we all know, the classical loss in magnetic sheets under negligible skin effect and sinusoidal induction is calculated by the standard formula Equation 5.1. However, at sufficiently high frequencies, the eddy current centerfield will impose an increasingly non-uniform induction profile across the sheet, and it is no longer a uniform induction. In this case, modelling magnetic loss encounter some difficulties, because it involves the

solution of Maxwell equations considering a strong non-linear magnetic constitutive equation. The solution is generally obtained through numerical method, which do not lead to simple expressions for the energy loss. As minor loops of small relatively small amplitude, laying in the Rayleigh region, we might consider adopting a permeability-based magnetic constitutive equation of the material. This permeability could be introduced in the electromagnetic diffusion equation, achieving induction profile and classical energy loss. Therefore, hysteresis loops at very low frequencies could be assumed as a function of peak induction B_p. To validate the model, three types of permeability have been introduced in the modelling.

1) The same as Chapter 5.2.1, the permeability μ chosen as the ratio of the peak induction B_p and the peak field H_p.
2) The complex permeability $\underline{\mu}=\mu'-j\mu''$ .This permeability considers the phase shift appearing under quasi-static conditions between the sinusoidal B and the first harmonic of H, which increases the hysteresis loss. Its modulus is still equal to B_p/H_p. It is an approximate evaluation of the hysteresis loop as shown in Figure 6.2. As illustrated, the imaginary part is identified in such a way that the hysteresis loss W_{hyst} of the measured loop and that of the equivalent elliptical cycle coincide, according to the equation $\mu''=W_{hyst}/(\pi \cdot H_p^2)$.

3) The Rayleigh law, $J_p = aH_p + bH_p^2$.

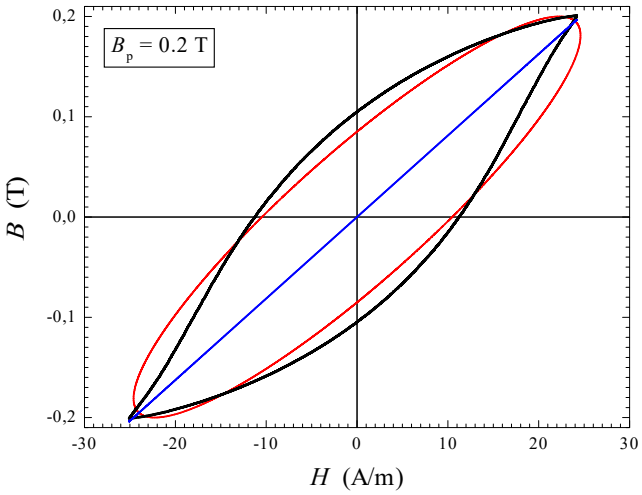

Figure 6.2: Experimental quasi-static loop at peak induction $B_p = 0.2$ T in the NO Fe-Si sheet. It is approximated either by a straight $B(H)$ line ($\mu = 8.13 \cdot 10^{-3}$ Tm/A) or by the elliptic loop of identical area associated with the complex permeability $\underline{\mu} = \mu' - j\mu''$, with $\mu' = 7.35 \cdot 10^{-3}$ Tm/A and $\mu'' = 3.47 \cdot 10^{-3}$ Tm/A

6.2.1 Linear permeability and Complex Permeability

A. Classical Loss Component

The first permeability adoption is elaborated in the last chapter. The following sections describe the loss separation and the statistical loss introduced these two types of permeability.

Considering the minor static loop represented as a first approximation by the modulus of the permeability $\mu = B_p / H_p$, the classical loss is directly obtained by solving Maxwell's diffusion equation and the detailed deduction is in Chapter 5. The result is

$$W_{\text{class}}(f) = \frac{\pi}{2} \cdot \frac{\lambda B_p^2}{\mu} \cdot \frac{\sinh \lambda - \sin \lambda}{\cosh \lambda - \cos \lambda}, \quad [\text{J/m}^3] \tag{6.1}$$

where $\lambda=\sqrt{\pi\mu\sigma fd^2}$ .Here ,introduce the complex permeability $\underline{\mu}=\mu'-j\mu''$ as magnetic constitutive equation, we get

$$\lambda=\lambda'+j\lambda''=\sqrt{\frac{\omega\sigma d^2\left|\underline{\mu}\right|}{2}}\cdot\left(\sqrt{\frac{1+\mu'/\left|\underline{\mu}\right|}{2}}-j\sqrt{\frac{1-\mu'/\left|\underline{\mu}\right|}{2}}\right) \tag{6.2}$$

Then according to these two equations, we obtain the classical loss,

$$W_{\text{class}}(f)=\frac{\pi}{2}\cdot\frac{B_{\text{p}}^2}{\left|\underline{\mu}\right|}\frac{(\lambda'-\lambda'')\cdot\sinh(\lambda'-\lambda'')-(\lambda'+\lambda'')\cdot\sin(\lambda'+\lambda'')}{\cosh(\lambda'-\lambda'')-\cos(\lambda'+\lambda'')} \tag{6.3}$$

B. Hysteresis Loss Component

To consider the hysteresis loss versus frequency behaviour changes due to the frequency evolution of the induction profile across the sheet thickness, we shall take advantage of the local character of the associated dissipation mechanism, which is elementary Barkhausen jumps and extremely localized eddy currents. First step assumed that the hysteresis loss component depends on the peak induction according to a power law

$$W_{\text{hyst}}=K\cdot B_{\text{p}}^{\alpha} \tag{6.4}$$

The parameters K and α can be identified by best fitting of the hysteresis loss measured at B_{p}=0.05T, 0.1T, 0.2T.

Then let's consider the induction profile across the sheet thickness $b_{\text{p}}(x)$, where x is the distance from sheet midplane. Using the adopted model permeability, W_{hyst} is instantly expressed as

$$W_{\text{hyst}}(B_{\text{p}},f)=\frac{1}{d}\int_{-d/2}^{d/2}K\cdot b_{\text{p}}^{\alpha}(x)\text{d}x \tag{6.5}$$

C． Excess Loss Component

V_0 is depend on B_p, so the excess loss is assumed dependent on the measured peak induction B_p, the excess loss component is calculated as

$$W_{exc}(B_p, f) = 8.76 \cdot \sqrt{\sigma GSV_0(B_p) f} \cdot B_p^{1.5} \tag{6.6}$$

where the dimensionless constant G=0.1356, S is the cross-section area of the sheet sample, and the statistical parameter V_0 is an increasing function of B_p. $V_0(B_P)$ is predicted by means of standard loss measurements under sinusoidal induction at frequencies where the skin effect can be ignored.

6.2.2 Experimental results

The magnetic energy loss $W(f)$ has been measured in 0.194 mm thick Fe-(3.2 wt.%)Si sheets. Ring samples of outside diameter 100 mm and inside diameter 80 mm, annealed 2 hours at 760 °C after punching, have been tested at B_p values ranging between 50 mT and 0.2 T up to 10 kHz. The measurements have been performed by means of a broadband calibrated hysteresisgraph-wattmeter with digital control of the induction waveform. Three interpretative models have been applied to the obtained results.

1) A standard model neglecting skin effect and using (1) for the calculation of the classical loss.

2) A linear diffusion model using the quasi-static modulus of permeability $\mu = B_p/H_p$.

3) A linear diffusion model assuming the complex quasi-static permeability $\underline{\mu} = \mu' - j\mu''$ as the material constitutive equation.

Figure 6.3 provides an example of experimental $W(f)$ behaviour obtained up to 10 kHz for B_p = 0.2 T compared with the total loss predictions based on the previous three approaches. It shows how the complex permeability model (3) leads to the best agreement with the measured $W(f)$. The hysteresis $W_{hyst}(f)$ and excess $W_{exc}(f)$ loss components calculated according to (5) and (6) are also provided. It is noted the slight increase of $W_{hyst}(f)$ at the highest frequencies. Similar fitting results are obtained for B_p = 50 mT and B_p = 0.1 T.

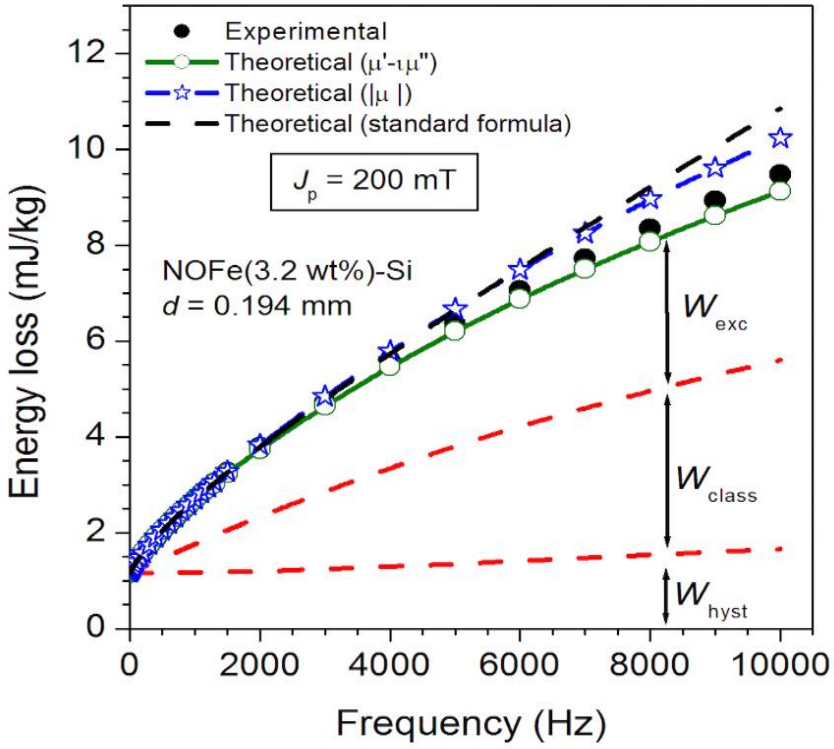

Figure 6.3: Energy loss $W(f)$ measured in a 0.194 mm thick Fe-(3.2 wt%)Si sheet up to 10 kHz at peak polarization J_p = 200 mT. The J_p value is low enough to fulfill the Rayleigh law and the skin effect fully develops above a few kHz. The measured $W(f)$ is predicted best by adopting the quasi-static complex permeability at J_p = 200 mT as the material constitutive equation. To note the increase of the hysteresis loss component W_{hyst} with the frequency.

6.3 PWM Regime Application and Experimental Results

Two-level PWM induction waveforms have been measured in 0.194 mm thick Fe (3.2 wt%)-Si ring sample. An example of the obtained induction waveform and hysteresis loops is shown in Figure 6.1. The waveforms are characterized by the modulation index $m_f = F/f$, the ratio of the switching frequency F to the fundamental frequency f, and the peak induction B_p. To estimate the energy loss, I decomposed the whole PWM induction loop into the major loop (black in Figure 6.1) and the minor loops (red and blue). The period of the major loop is T_M and the equivalent frequency is $f_M = 1/T_M$. The period of each minor loop is T_m and its equivalent frequency is $f_m = 1/T_m$. All the parameters of the PWM waveform are summarized in Table 6.1. I modelled the related energy loss by calculation of the hysteresis, classical, and excess components, each of them resulting from the separate contributions of the major and the minor loops.

A. Loss Associated with the Major loops

The major loop is equivalent to a symmetric cycle of peak value B_p and frequency f_M, obtained under triangular induction waveform. For this case, the skin effect can be neglected. According to literature [53], there is almost no differences arising at intermediate inductions, for instance, B_p =1.3T. And the loss calculation is easily performed.

a. Classical Loss

$$W_{class}(f) = \int_0^T P_{class}(t)\mathrm{d}t = \frac{1}{12}\sigma d^2 \int_0^T J^2(t)\mathrm{d}t \tag{6.7}$$

For triangular magnetization

$$W_{class}(f) = \frac{4}{3}\pi^2 \sigma d^2 B_p^2 f \tag{6.8}$$

b. Hysteresis Loss

In the major loop, ignoring the minor loop, hysteresis energy loss is independent of the induction wave shape. The hysteresis component W_{hyst} is obtained by extrapolating $W_{\text{total}}(f)$ to $f = 0$

c. Excess Loss

$$W_{\text{exc}}(f) = \int_0^T P_{\text{exc}}(t)\mathrm{d}t = \sqrt{\sigma G S V_o}\int_0^T \left|\dot{B}(t)\right|^{3/2}\mathrm{d}t \tag{6.9}$$

For triangular induction

$$W_{\text{exc}}(f) = 8\sqrt{\sigma G S V_o}B_{\text{p}}^{3/2}f^{1/2} \tag{6.10}$$

So

$$W_{\text{total}}(f) = W_{\text{hyst}} + \frac{4}{3}\pi^2\sigma d^2 B_{\text{p}}^2 f + 8\sqrt{\sigma G S V_o}B_{\text{p}}^{3/2}f^{1/2} \tag{6.11}$$

B. Loss Associated with the Minor Loops

Each minor loop, characterized by the bias induction B_{b}, the peak-to-peak amplitude $2\cdot B_{\text{m}}$, and the equivalent magnetizing frequency f_{m}, is separately considered. Since f_{m} can be of several tens of kilohertz, the skin effect cannot be ignored. In addition, the minor loops are not centred, and their shape changes with the bias B_{b}. However, to simplify the matter, the following assumptions are made. Firstly, the minor loops are swept with sinusoidal flux, with the same parameters (B_{b}, B_{m}, and f_{m}). Therefore, it is possible to use the complex permeability formalism to define the Maxwell diffusion equation. Secondly, the minor loops are assumed to be congruent in B, that is, a minor loop with parameters (B_{b}, B_{m}, and f_{m}) starting from the anhysteretic curve, is congruent with the minor loop endowed with the same parameters hanging from the major cycle. Then the static complex permeability $\underline{\mu}(B_{\text{m}}, B_{\text{b}})$ is identified on the anhysteretic curve as a function of B_{m} and B_{b}. This procedure is described in Figure 6.4. Here, the bias polarization is applied by a third winding, wound on the toroid and supplied by a stable DC current. Five values of B_{b}, up to 1.4 T, and $\pm B_{\text{m}}$ values ranging between 50 mT and 0.2 T have been selected. The different loss contributions from the

minor loops at the typical PWM working frequencies have then been calculated as follows.

1) *Classical Loss Component*: The classical loss is calculated applying Equation 6.3, with the complex permeability pertaining to each specific (B_m, B_b) minor loop.

2) Hysteresis Loss Component: Equation 6.5 is calculated, with the coefficients K and α duly considered as a function of B_m and B_b.

3) *Excess Loss Component:* Equation 6.6 is applied, now with V_0 depending on both B_m and B_b. A direct determination of $V_0(B_m, B_b)$ would require measurements and loss separation at each bias induction B_b, a cumbersome procedure. We have, therefore, resorted to an approach, discussed in [39], where V_0 is calculated as a function of the induction bias. The following formula holds:

$$V_0(B_m, B_p) = \frac{1}{c} < \sqrt{1/\mu} >^2 \tag{6.12}$$

where c is a suitable constant introduced in literature [39], μ is the differential permeability, and the brackets indicate averaging of the differential permeability over the given minor cycle. For small amplitude B_m, we can write

$$V_0\left(B_m, B_b\right) \approx V_0\left(B_m, B_b = 0\right) \frac{\left|\underline{\mu}\left(B_m, B_b = 0\right)\right|}{\left|\underline{\mu}\left(B_m, B_b\right)\right|} \tag{6.13}$$

and we can simply proceed to implement the loss separation procedure for symmetric minor loops. Figure 6.3 provides an example of PWM loss measurement at 1 kHz in the 0.194 mm thick non-oriented Fe–Si sheet. The major loop is described between ±1.3 T and the modulation index m_f is varied between

5 and 13. The experimental dependence of the PWM energy loss is predicted to good extent by the model.

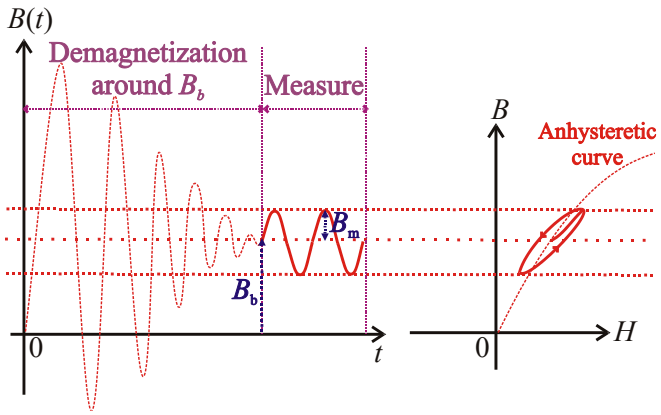

Figure 6.4: Acquisition method of the static complex permeability $\underline{\mu}(B_m, B_b)$ on the anhysteretic curve as a function of peak and bias induction pair (B_m, B_b). The bias value is generated by a third winding supplied by a stable constant current.

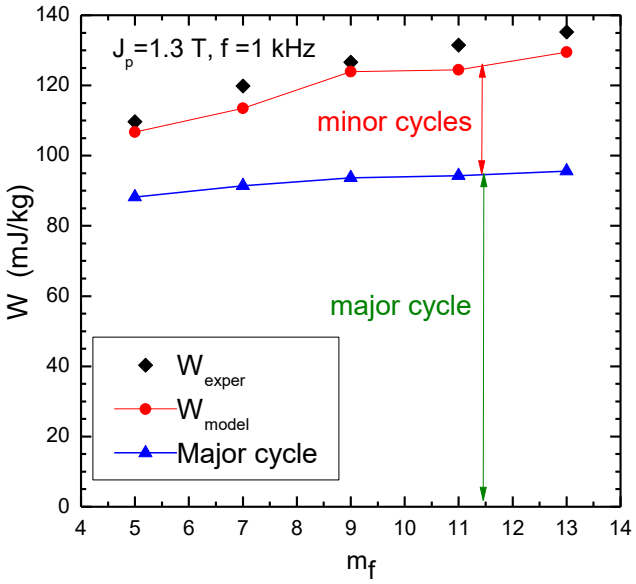

Figure 6.5: Non-oriented Fe-Si sheet of thickness 0.194 mm. Comparison of the energy losses measured at the peak polarization J_p = 1.3 T with PWM waveform as a function of the modulation index mf at the fundamental frequency f = 1 kHz with the prediction of the model.

Table 6.2: Parameters of the PWM induction regime

Symbol	Description
B_p	Peak value of the PWM induction waveform (or the major loop), assumed to be centered
$2 \cdot B_m$	Peak to peak value of a given minor loop
B_b	Mean value of the induction on a given minor loop (bias)
f	Frequency of the PWM waveform
F	Switching frequency of the PWM
m_f	Modulation index of the PWM, defined as $m_f = F/f$.
f_M	Equivalent frequency of the major loop, obtained as the inverse of the time spent on the major loop
f_m	Equivalent frequency on a given minor loop, obtained as the inverse of the duration of the minor loop

6.4 Conclusion and Discussion

It is shown that a simplified approach to the constitutive equation of a magnetic sheet at low induction values, expressed in terms of complex permeability, in combination with the STLs, makes it possible to account in analytical terms for the dependence of the energy loss of minor loops up to frequencies involving large skin effect. It is shown, in particular, that the case of the two-level PWM waveform with nested minor loops can be simply treated by the model, which permits one to attain good agreement with the experimental results.

Chapter 7

Energy loss in soft magnetic material under symmetric and asymmetric induction waveform

7.1 Introduction

Last Chapter I considering the minor loop hysteresis loss modelling. However, non-sinusoidal voltage waveforms are ubiquitously found in magnetic components employed in power electronics. Besides the distortion engendered by the non-linear response of the material, a variety of pulsed and rectangular voltages are imposed in electrical machine cores and in various types of inductive devices. In order to find the magnetic components and the design providing the best tradeoff between costs and performance, a method to predict the magnetic losses for realistic working conditions should therefore be devised. A case in point is one of symmetric and asymmetric triangular-trapezoidal induction waveforms, a typical regime imposed to the inductive components found in

Switch Mode Power Supplies, converters, and permanent magnet motors. The buck DC-DC converter working in continuous mode provides a fitting example [54]. This is a standard device used to supply a load R_{load} with a DC voltage V_{out} lower than the input DC voltage V_{dc}, where the employed inductor is excited by an asymmetric sawtooth current.

This part devoted to measurement and analytical prediction of the magnetic losses in different materials on a broad frequency range, under symmetric and asymmetric triangular induction waveforms.

Finding a way to calculate the magnetic losses under non-conventional operating modes starting from a minimum set of data, either measured directly or provided by the manufacturer, is an appealing objective, highly suitable for applications, where circuit designers still rely on empirical models. On the other hand, the broadband loss figures pertaining to such modes, namely the rectangular voltage waveforms, are much more difficult to achieve by measurements than in the usual case of sinusoidal voltage and are not available on the data sheets.

The standard approach of the literature is based on the Steinmetz equation and its many extended/improved versions, like the Modified Steinmetz Equation MSE, the Generalized Steinmetz Equation GSE, the Improved Generalized Steinmetz Equation iGSE, the Natural Steinmetz equation NSE, and the Waveform Coefficient Steinmetz Equation WcSE The standard Steinmetz equation for the power loss under sinusoidal induction at given frequency f and peak value B_p, is expressed as $P = kf^{\alpha} B_p^{\beta}$, where k, α, and β are adjustable parameters. In order to deal with non-sinusoidal induction, it is modified in the iGSE according to the equation

$$P = f \int_0^{1/f} k_i \left| \frac{dB}{dt} \right|^{\alpha} (\Delta B)^{\beta-\alpha} dt \tag{7.1}$$

for a peak-to-peak induction value ΔB. The parameter k_i is here a suitable combination of k, α, and β. This formulation aims at a more realistic account of the dependence, lumped in the exponent α, of the power loss on the induction derivative. However, despite the claimed successful comparison with the experiments, the empirical character of the Steinmetz approach is unsatisfactory from a scientific viewpoint and the source of practical limitations. The involved parameters are, for example, dependent on frequency and flux density [57] and the domain of application can be widened at the cost of an increasing number of pre-emptive measurements [58].

A certain difficulty in physically assessing the behavior of the magnetization process, its evolution with frequency and the related dissipation mechanisms [55] is one main reason for the persisting acceptance of the Steinmetz equation in the engineering milieu. Actually, the problem of predicting by analytical formulation the magnetic loss in soft magnetic sheets subjected to non-sinusoidal induction waveform has since long been posed, *in the absence of skin effect*, under the firm physical background offered by the Statistical Theory of Losses (STL) [33] and the related loss decomposition concept [60]. Trapezoidal and triangular induction waveforms have been treated in [61] and related applications have been reported, among others, in [62], [63], [64]. Further theoretical improvements, including loss prediction with minor loops, were obtained in [65] and pertaining concepts were later invoked in [66]. With the average energy loss at a given frequency $W(f) = P(f)/f$ composed of a frequency independent hysteresis (quasi-static) W_{hyst}, classical $W_{cl}(f) \propto f$, and excess $W_{exc}(f) \propto f^{1/2}$ contributions, according to $W(f) = W_{hyst} + W_{cl}(f) + W_{exc}(f)$, and with the instantaneous dynamic power loss values evolving in steel sheets as $P_{cl}(t) \propto (dB/dt)^2$ and $P_{exc}(t) \propto |dB/dt|^{3/2}$, the model can naturally incorporate the prediction for generic periodic $B(t)$. A recent application of this concept concerning the inductor loss (Sendust powder core) in a buck converter has been proposed, although on a restricted frequency range (40 kHz –

100 kHz) [67]. On the contrary, awkward adaptation of the Steinmetz parameters to any specific $B(t)$ law is imposed by the empirical character of the involved equations [68]. It is understood, for example, that defined single values for these parameters cannot comply with the obviously different frequency dependence of static and dynamic energy losses.

On the other hand, the STL-based model has been so far mostly applied for working regimes of electrotechnical interest, typically on steel sheets excited up to a few hundred Hz with symmetric $B(t)$ waveforms. With growing applications (e.g., in electric vehicles) of high-speed rotating machines and increasing working frequencies in power electronics, the need for broadband modelling of magnetic losses, including versatile treatment of non-sinusoidal regimes (e.g., triangular induction with symmetric/asymmetric duty cycles) has become apparent.

In this study, I investigate the energy loss versus frequency properties of thin (~ 0.20 mm) Fe-Si and Fe-Co steel sheets, measured up to a few kHz, of field-treated high-permeability nanocrystalline Finemet ribbons, and of Mn-Zn ferrite samples, up to the MHz range. Physical and geometrical parameters of the investigated samples are provided in Table 7.1. Sinusoidal, triangular symmetric and triangular asymmetric induction waveforms have been considered, with duty cycle a ranging between 0.5 (symmetric wave) and 0.1. Starting from the $W(f)$ behavior measured under sinusoidal induction, we retrieve the associated loss components and transform them into the corresponding components for symmetric triangular induction. Remarkably, the method permits one to identify, on the one hand, the critical frequency for the appearance of the skin effect in the steel sheets (f_c ~ 800 Hz in Fe-Co and f_c ~ 1500 Hz in Fe-Si) and, on the other hand, to correspondingly manage the loss decomposition upon the whole investigated DC – 5 kHz range. At the same time, it is applied up to the MHz range in the nanocrystalline and ferrite samples. In this case, a generalized classical loss component $W_{cl}(f)$ is

discussed and calculated. With the so predicted $W(f)$ for symmetric triangular induction, we can easily derive the $W(f)$ behavior for the asymmetric waveforms, combining the losses pertaining to the two different duty cycles, that is, the two different frequencies $f_1 = 1/(2aT)$ and $f_2 = 1/(2(1-a)T)$.

Table 7.3: Physical Parameters of the Investigated Material

Material	NO Fe-Si	Fe-Co	Mn-Zn ferrite N87	Nanocrystalline ribbon
Sample	Epstein	Epstein	Ring	Ring
Thickness d (mm)	0.194	0.201	5.09	$20.46 \cdot 10^{-3}$
Density δ (kg/m^3)	7650	8120	4850	7200
Resistivity ρ (Ω m)	$52.0 \cdot 10^{-8}$	$44.0 \cdot 10^{-8}$	9.4	$118.0 \cdot 10^{-8}$
Saturation polarization J_s (T)	2.00	2.35	0.50	1.25

Such a broad combination of different materials and frequency ranges is, to authors' knowledge, unique. The fact that high frequencies are involved in applications has prompted many literature investigations at such frequencies, generally upon a narrow band [67]. However, comprehensive modelling calls for wideband measurements.

We remark that the role of the DC bias, like the one imposed by the load in a buck converter, is not considered in the present treatment, for the sake of simplicity. It could be considered, at least in the absence of deep skin effect, by a pure phenomenological approach [16] or with the method introduced in [69],

leading to the prediction of the loss with sinusoidal induction and bias starting from the separation without bias (symmetric minor loops). This would require, however, the introduction of a hysteresis model (e.g., the Preisach model) and numerical calculations and would be at odds with our declared aim of developing a simple analytical approach. The presently discussed method can actually provide substantial prediction of the loss under square-wave voltage, even in the presence of a DC bias, if one can obtain this figure via the much simpler measurements under sinusoidal voltage. In such a case, we can again perform the loss separation, because the classical loss $W_{cl}(f)$ is independent of the bias, and simply retrieve the loss components for square-wave voltage. This will be further discussed in the following.

7.2 Experimental Method and Procedure

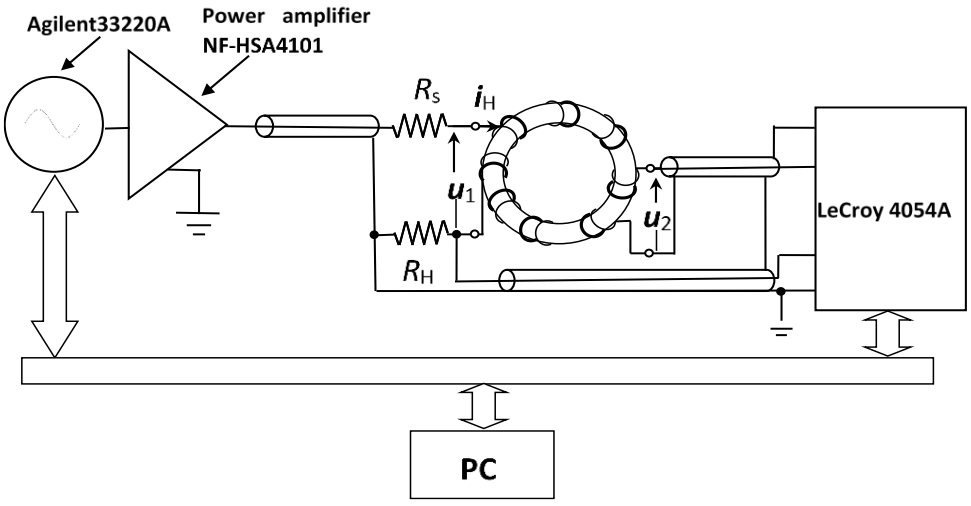

Figure 7.1: Hysteresisgraph-wattmeter used to measure the broadband magnetic losses of soft magnetic materials. The induction waveform is controlled regulating the supply current (measured via the voltage drop on the calibrated shunt R_H) by digital feedback. This setup has been used to characterize both the Fe-Si and Fe-Co Epstein strips up to 5

kHz and the Mn-Zn and nanocrystalline ring samples up to 4 MHz. The ring samples are eventually characterized up to 100 MHz by a transmission line method using a Vector Network Analyzer (VNA).

Non-oriented Fe-Si and Fe-Co steel sheets, 0.194 mm and 0.201 mm thick, respectively, have been characterized at peak induction B_p = 1.0 T up to a few kHz using a 200-turn Epstein magnetizer, according to the IEC 60404-10 Standard. A calibrated hysteresisgraph-wattmeter with digital control of the induction waveform, using an Agilent33220A arbitrary function generator and a DC-10 MHz NF-HSA4101 power amplifier for supplying the primary winding, was employed. Signal detection, conversion, and analysis were made through a 12-bit 500 MHz LeCroy4054A oscilloscope and software (Agilent VEE environment). The digital control of the induction waveform was carried out by means of recursive method, where the desired voltage output $u(t)$ is approached through an iterative procedure, by which the $(n + 1)$th periodic voltage input $e(t)$ is updated by addition of a term linearly dependent on the difference between the desired output and the one obtained at the nth iteration [20]. The scheme of the employed setup is shown in Figure 7.1. Besides the conventional characterization under sinusoidal induction, carried out up to f = 5 kHz, energy loss measurements were performed in the non-oriented steel sheets with square wave voltage and duty cycle a ranging between 0.5 and 0.1, as schematically illustrated in Figure 7.2. In this case, we start by generating a rectangular voltage with the function generator and we proceed with the recursive procedure till the desired rectangular voltage $V_2(t)$ is obtained on the secondary winding. The same setup was employed to measure nanocrystalline Finemet ribbons of thickness d = 20.46 μm and width w = 10 mm, tapewound as 20 mm diameter rings and annealed under a tranverse saturating field (induced transverse anisotropy $K_{\perp} \sim 25$ J/m^3) and commercial N87-type Mn-Zn ring samples (outside diameter 15 mm, thickness 5.09 mm). The measurements in these samples were performed up to 1 – 4 MHz at B_p = 100 mT. The primary and secondary windings, their layout, and the connecting cables

ensured minimum stray parameters. High-frequency measurements, from a few hundred kHz to 100 MHz, were covered by a transmission line method using an Agilent 8753A Vector Network Analyzer, as discussed in [21]. Such method provides the frequency behavior of the complex permeability $\underline{\mu} = \mu' - j\mu''$ and is obviously restricted to defined exciting power (10 mW in the present case) and sinusoidal signal. But the fluxmetric measurements show that, on approaching the MHz frequencies, μ' and μ'' become independent of B_p, at least below some 100 mT in the Mn-Zn ferrites and 500 mT in the transverse anisotropy nanocrystalline ribbons, and overlap with the VNA measured permeabilities. This occurs at frequencies high enough to induce full relaxation of the domain wall (dw) displacements, much more restrained than the rotations by the dissipative effects. On the other hand, the rotational permeability is relatively independent of B_p, up to about $0.1J_s$ – $0.2J_s$ in ferrites and $0.5J_s$ in the transverse anisotropy nanocrystalline ribbons. It is therefore found that, at sufficiently high frequencies (typically beyond a few hundred kHz), the energy loss fluxmetrically measured at given B_p value tends to coincide with the loss figure calculated from the measured μ' and μ'' through the equation

$$W(B_p, f) = \pi B_p^2 \frac{\mu''}{\mu'^2 + \mu''^2} \qquad [\mathrm{J/m^3}] \tag{7.2}$$

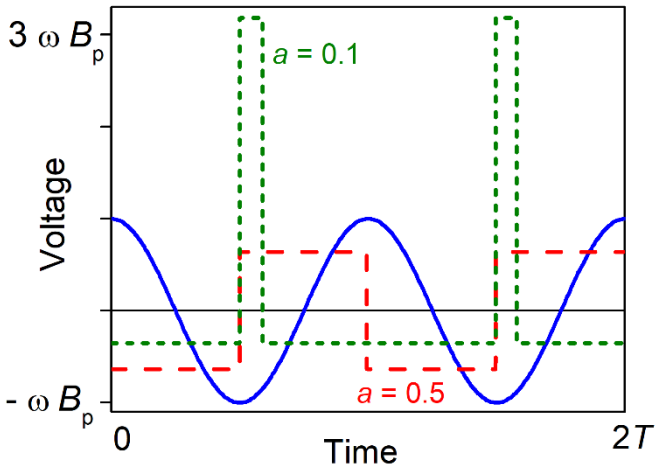

Figure 7.2: Example of investigated voltage waveforms for given peak induction B_p: sinusoidal, symmetric square, and asymmetric square with duty cyle a = 0.1.

This property is illustrated, together with the behavior of μ', in Figure 7. 3 for the investigated Mn-Zn ferrite and nanocrystalline samples at B_p = 100 mT. The upper frequency portion of the fluxmetrically obtained results (symbols) are shown to overlap with the lower frequency portion of the VNA determined permeability and loss values. μ' and μ'' suffice then to describe, for defined B_p value, shape and area of the hysteresis loop (quasi-linear response) .

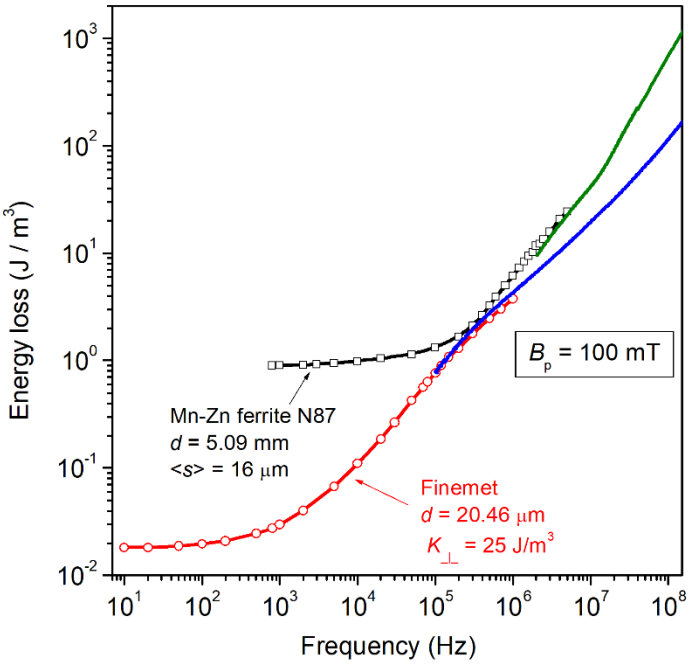

Figure 7.3: Broadband behavior of energy losses at B_p = 100 mT in the tapewound transverse anisotropy ($K_\perp$ = 25 J/m^3) Finemet-type nanocrystalline ribbon and in the N87 Mn-Zn ferrite. d ≡ thickness, <s> ≡ average grain size. Symbols: fluxmetric measurements. Solid lines: measurements by transmission line and VNA and use of (2). The inset shows the corresponding frequency dependence of the real relative permeability μ'_r.

7.3 From sinusoidal to triangular symmetric and asymmetric induction: energy loss prediction

In this Section we develop first a comprehensive approach to the prediction of magnetic losses under symmetric and asymmetric square-wave voltage in thin (d ~ 0.20 mm) non-oriented steel sheets, up to 5 kHz, in Mn-Zn ferrites and in transverse anisotropy ($K_\perp$ ~ 25 J/m^3) nanocrystalline ribbons up to a few MHz.

We verify that skin effect enters into play in the steel sheets around 800 Hz in the Fe-Co sheets and 1500 Hz in the Fe-Si sheets. In order to extend the analysis beyond such frequencies, we describe the magnetic constitutive equation of the material at low and intermediate inductions (B_p = 1.0 T in the present measurements) by an equivalent complex permeability. In this way, we can analytically solve the Maxwell's diffusion equation and proceed with the loss decomposition under sinusoidal induction. The Landau-Lifshitz equation is invoked for making explicit the constitutive equation of the Mn-Zn ferrite and nanocrystalline ring samples at high frequencies and for proceeding with loss decomposition. Examples of experimental and interpretative results obtained in these materials for B_p = 100 mT are given.

7.3.1 Losses in non-oriented Fe-Si and Fe-Co sheets

The energy losses under triangular induction waveform at power frequencies can be easily dealt with in magnetic steels sheets starting from standard measurements under sinusoidal induction, resorting to the STL, and formulating in a simple way the energy loss components W_{hyst}, $W_{cl}(f)$, and $W_{exc}(f)$ under generic induction waveform [10], [13]. The condition of negligible skin effect, implying relatively low working frequencies, is, however, required. We provide in Fig. 4 an example concerning the energy losses measured up to f = 800 Hz in the 0.201 mm thick $Fe_{49}Co_{49}V_2$ sheet. Following the loss decomposition method, we identify first the waveshape independent hysteresis component $W_{hyst}(B_p) = \lim_{f\to 0} W(B_p, f)$ and calculate the classical loss component

$$W_{cl}(B_p, f) = \frac{\sigma d^2}{12} \cdot \int_0^{1/f} \left(\frac{dB}{dt}\right)^2 dt \ \ [J/m^3] \tag{7.3}$$

in the sheet of thickness d and conductivity σ. The appraisal of the dynamics of the Magnetic Objects (mesoscopic regions where the dws move in a tightly

correlated fashion [9]), made according to the STL [15], leads to the following general formulation for the excess loss

$$W_{\mathrm{exc}}(B_{\mathrm{p}},f)=\sqrt{\sigma GSV_0(B_{\mathrm{p}})}\cdot\int_0^{1/f}\left|\frac{\mathrm{d}B}{\mathrm{d}t}\right|^{3/2}\mathrm{d}t,\ [\mathrm{J/m^3}] \tag{7.4}$$

where G = 0.1356, S is the sample cross-sectional area, and $V_0(B_{\mathrm{p}})$ is a statistical parameter, increasing with B_{p}. This parameter lumps the role of the microstructure [9]. We can easily specialize (7.4) to any kind of periodic induction waveform without local minima (i.e. without minor nested hysteresis loops). For sinusoidal $B(t)$ we obtain

$$W_{\mathrm{cl,SIN}}(B_{\mathrm{p}},f)=\frac{\pi^2}{6}\cdot\sigma d^2B_{\mathrm{p}}^2f \qquad [\mathrm{J/m^3}] \tag{7.5}$$

and

$$W_{\mathrm{exc,SIN}}(B_{\mathrm{p}},f)=8.76\sqrt{\sigma GSV_0(B_{\mathrm{p}})}\cdot B_{\mathrm{p}}^{3/2}f^{1/2}.\ [\mathrm{J/m^3}] \tag{7.6}$$

Using (7.3) and (7.4), we conclude that, once the energy loss for sinusoidal induction is known, we can predict the same quantity for triangular symmetric $B(t)$, according to

$$\begin{aligned}&W_{\mathrm{TRI05}}(B_{\mathrm{p}},f)=W_{\mathrm{hyst}}(B_{\mathrm{p}})+W_{\mathrm{cl,TRI05}}(B_{\mathrm{p}},f)+W_{\mathrm{exc,TRI05}}(B_{\mathrm{p}},f)=\\&=W_{\mathrm{hyst}}(B_{\mathrm{p}})+\frac{8}{\pi^2}\cdot W_{\mathrm{cl,SIN}}(B_{\mathrm{p}},f)+k_{\mathrm{exc}}\cdot W_{\mathrm{exc,SIN}}(B_{\mathrm{p}},f)\end{aligned}, \tag{7.7}$$

with $W_{\mathrm{hyst}}(B_{\mathrm{p}})$ independent of the $B(t)$ law and the constant k_{exc} = 8/8.76. In some circumstances, as shown in the following, the excess loss is found to follow the power law $W_{\mathrm{exc,SIN}}(f) \propto f^{\,p}$, with $p > 0.5$ [22]. In this case, the general relationship for W_{exc} applies

$$W_{\mathrm{exc,TRI05}}(B_\mathrm{p}, f) = k_\mathrm{exc} \cdot W_{\mathrm{exc,SIN}}(B_\mathrm{p}, f) \tag{7.8}$$

where $k_\mathrm{exc} = 4^{(1+p)}/[(2\pi)^p \cdot \int_0^{2\pi} |\cos\alpha|^{(1+p)}\,\mathrm{d}\alpha]$ and $\alpha = \omega t$. It is remarked that *a couple of measurements, for given* B_p, *of* $W_\mathrm{SIN}(B_\mathrm{p}, f)$ *at two frequencies* suffice in principle to make the loss decomposition and apply (7.7). The ensuing prediction is shown, as an example, in Figure 7. 4a (0.201 mm thick Fe-Co sheet, dashed line), compared with the experimental $W_\mathrm{TRI05}(f)$ at B_p = 1.0 T (open symbols) up to the maximum frequency f = 800 Hz. Fig. 4b shows, in particular, the measured excess losses $W_\mathrm{exc,SIN}(f)$ and $W_\mathrm{exc,TRI05}(f)$, both following the $f^{1/2}$ law. The latter is compared with the predicted quantity $(8/8.76)\cdot W_\mathrm{exc,SIN}(f)$. It is a result easily extrapolated to the case of asymmetric triangular $B(t)$. It suffices to apply (7) twice, for the frequencies $f_1 = 1/(2aT)$ and $f_2 = 1/(2(1\text{-}a)T)$, respectively, and average the resulting loss figures. Fig. 4a also shows the measured (symbols) and predicted by (7) (dashed-dotted line) loss $W_\mathrm{TRI01}(f)$ (symbols), for the asymmetric $B(t)$ with duty cycle a = 0.1.

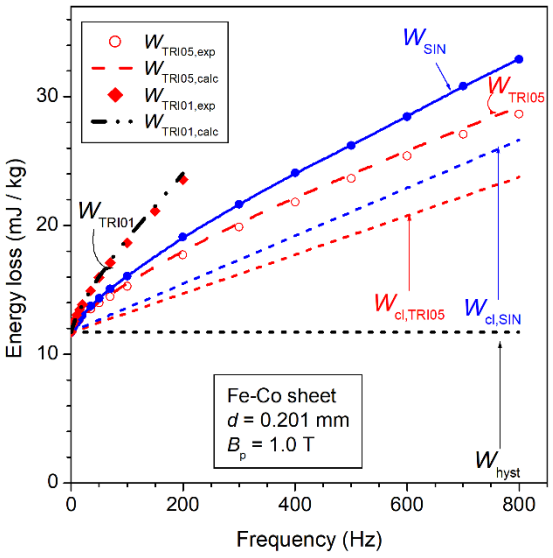

(a)

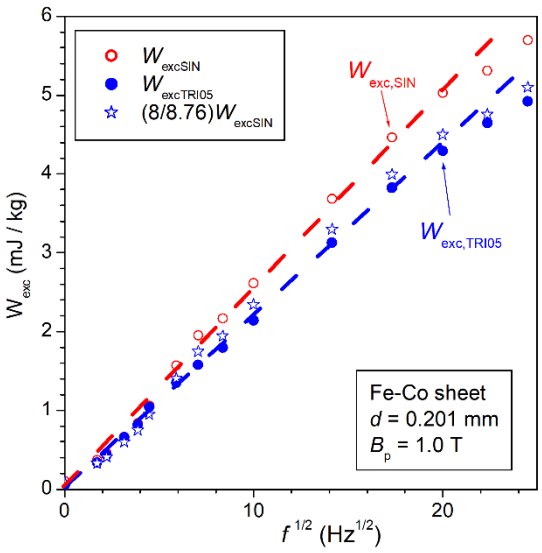

(b)

Figure 7.4: a) Energy loss in the 0.201 mm thick Fe-Co sheets up to 800 Hz (i.e., up to incipient skin effect) measured under sinusoidal (W_{SIN}) and triangular symmetric (W_{TRI05}) induction (symbols) of peak value B_p = 1.0 T. The loss components $W_{cl,TRI05}$ and $W_{exc,TRI05}$ are obtained from the corresponding quantities $W_{cl,SIN}$ and $W_{exc,SIN}$ according to (7.3) and (7.4) and $W_{TRI05}(f)$ is consequently calculated by (7.7) (dashed line). The loss figure W_{TRI01} (symbols) measured with asymmetric triangular $B(t)$ and duty cycle a = 0.1, and its prediction (dash-dot line) are also shown up to 200 Hz. b) Excess loss components $W_{exc,SIN}$ and $W_{exc,TRI05}$ versus $f^{1/2}$. They both follow the $f^{1/2}$ law below about 600 Hz. The experimental $W_{exc,TRI05}$ (full symbols) is compared with the predicted quantity $(8/8.76)W_{exc,SIN}$ (open symbols). The dashed lines are a guide to the eye.

It is apparent here, besides our capability of transposing in a simple way the theoretical assessment of $W_{SIN}(f)$ into a good prediction of $W_{TRI01}(f)$ by (7.7), the relatively restricted frequency range of our prediction. This descends from the limitation posed by the appearance of the skin effect above a certain critical frequency f_0 (~ 800 Hz and ~ 1.5 kHz in the Fe-Co and Fe-Si sheets, respectively), with the ensuing deviations of the predictions by (7.5) and (7.6) from the actual

behaviors of $W_{cl,SIN}(f)$ and $W_{exc,SIN}(f)$. The loss decomposition procedure is indeed affected by the establishment of a non-uniform induction profile across the sheet thickness, a condition whose full treatment requires, because of the non-linear hysteretic constitutive magnetic equation of the material, hysteresis modelling (for example, the Dynamic Preisach modelling) and numerical methods [23]. It is a cumbersome procedure, of little practical appeal, and it might be appropriate to look for a much simpler approach, if worth the price to pay in terms of predicting accuracy. The conventional approach to the eddy current losses in a magnetic sheet of thickness d ($-d/2 \le z \le d/2$) with AC field applied along the y-direction consists in solving, with appropriate boundary conditions, the Maxwell's diffusion equation

$$\frac{\partial^2 H_y(z)}{\partial z^2} = \sigma\mu \frac{\partial H_y(z)}{\partial t} \tag{7.9}$$

in a hypothetical structureless material with linear DC constitutive equation $B = \mu H$. The classical loss is obtained as

$$W_{cl,SIN}(B_p, f) = \frac{\pi}{2} \cdot \frac{\lambda B_p^2}{\mu} \cdot \frac{\sinh \lambda - \sin \lambda}{\cosh \lambda - \cos \lambda}, \text{ [J/m}^3\text{]} \tag{7.10}$$

where $\lambda = \sqrt{\pi\sigma\mu d^2 f}$ [9]. The gross approximation involved with a linear constitutive equation leads, however, to poor prediction of $W_{SIN}(B_p, f)$ at high frequencies. Aiming thus at a realistic analytical formulation approximately accounting for hysteresis, we emulate the constitutive magnetic equation, as given by the quasi-static hysteresis loop of peak induction B_p, by an equivalent complex permeability, that is, an elliptical loop of identical area $W_{hyst}(B_p) = \pi B_p^2 (\mu''/(\mu'^2 + \mu''^2))$ and same B_p value. With $B_p = \sqrt{\mu'^2 + \mu''^2}\, H_p$, we can also write $W_{hyst}(H_p) = \pi H_p^2 \mu''$. With these two independent conditions, we

obtain the real and imaginary permeability components as $\mu' = 0.0159$ $TA^{-1}m^{-1}$ and $\mu'' = 0.0121$ $TA^{-1}m^{-1}$ in the Fe-Co sheets, $\mu'=0.0100$ $TA^{-1}m^{-1}$ and $\mu'' = 0.0078$ $TA^{-1}m^{-1}$ in the Fe-Si ones. Under quasi-static conditions, we assign these relationships both local and macroscopic character. The local static relationships are defined, over the here investigated frequency range, once and for all. The macroscopic ones, involving the applied field and the induction averaged over the sample cross-section, evolve with frequency. I am interested in predicting such an evolution. The involved approximations are obviously expected to apply better at low inductions and to comply with the frequency response of the material up to relatively mild non-uniform induction profiles. By introducing the previously defined complex $\underline{\mu}$ in the diffusion equation (7.9), now written as

$$\frac{\partial^2 \underline{H}_{\mathrm{y}}(z)}{\partial z^2} = j\omega\sigma\underline{\mu}\,\underline{H}_{\mathrm{y}}(z), \tag{7.11}$$

with the appropriate boundary conditions, we eventually arrive at the following analytical formulations for the frequency dependence of hysteresis and classical losses in the presence of skin effect

$$W_{\mathrm{hyst}}(B_{\mathrm{p}}, f) == \frac{\pi B_{\mathrm{p}}^{\,2}}{2|\underline{\mu}|}\frac{\mu''}{\mu'}\frac{(\lambda'+\lambda'')\sinh(\lambda'-\lambda'')+(\lambda'-\lambda'')\sin(\lambda'+\lambda'')}{\cosh(\lambda'-\lambda'')-\cos(\lambda'+\lambda'')}. \tag{7.12}$$

$$W_{\mathrm{cl,SIN}}(B_{\mathrm{p}}, f) == \frac{\pi}{2}\frac{B_{\mathrm{p}}^{\,2}}{\mu'}\cdot\frac{(\lambda'+\lambda'')\sinh(\lambda'-\lambda'')-(\lambda'-\lambda'')\sin(\lambda'+\lambda'')}{\cosh(\lambda'-\lambda'')-\cos(\lambda'+\lambda'')}, \tag{7.13}$$

where the complex quantity $\lambda = \lambda' + j\lambda''$ is related to the complex permeability through to the equation

$$\lambda = \sqrt{\frac{\omega\sigma|\underline{\mu}|d^2}{2}}\cdot\left(\sqrt{\frac{1+\mu'/|\underline{\mu}|}{2}} - j\cdot\sqrt{\frac{1-\mu'/|\underline{\mu}|}{2}}\right). \tag{7.14}$$

Equations (7.12) and (7.13) reduce to $W_{hyst}(B_p) = \lim_{f\to 0} W(B_p, f)$ and (7.5), respectively, for $f < \sim 5/(\pi\sigma|\mu|d^2)$. The full procedure by which the diffusion equation (7.11) leads to (7.12) and (7.13) is discussed in the Appendix. We have no equivalent formulation for the excess loss component $W_{exc}(B_p, f)$, which can only be obtained by making the difference between the experimental loss $W(f)$ and the sum $W_{hyst}(B_p, f) + W_{cl,SIN}(B_p, f)$. An example of the so obtained loss decomposition is shown, for the Fe-Co and Fe-Si sheets measured at $B_p = 1.0$ T up to 5 kHz, in Figure 7.5 and 7.6, respectively. Under increasing frequencies, the sample falls into a condition of non-uniform induction profile. By the previous equations we obtain, in particular, that W_{hyst} starts to increase and $W_{cl,SIN}(f)$ attains a less than linear increase with f beyond about 800 Hz in Fe-Co and 1500 Hz in Fe-Si. This contrasts with the behaviors predicted for these quantities by the conventional equation (7.5) (dashed lines).

We connect now the so-defined broadband loss components $W_{hyst}(f)$, $W_{cl,SIN}(f)$, and $W_{exc,SIN}(f)$ with the same quantities associated with the symmetric and asymmetric triangular induction. We calculate $W_{TRI05}(f)$ with (7.7), by posing $W_{cl,TRI05}(f) = (8/\pi^2)\cdot W_{cl,SIN}(f)$ and $W_{exc,TRI05}(f) = (8/8.76)\cdot W_{exc,SIN}(f)$ over the full frequency range. The total loss for triangular $B(t)$ is thus predicted, as previously discussed, as shown in Figure 7.7 and Figure 7.8 for the Fe-Co and Fe-Si sheets, respectively. Here, in particular, the experimental broadband energy losses $W_{TRI}(f)$ associated with the duty cycles $a = 0.5$, 0.2, and 0.1 (symbols) are shown to compare well with the prediction made by (7.7), starting from the calculated sinusoidal components $W_{hyst}(f)$, $W_{cl,SIN}(f)$, and $W_{exc,SIN}(f)$.

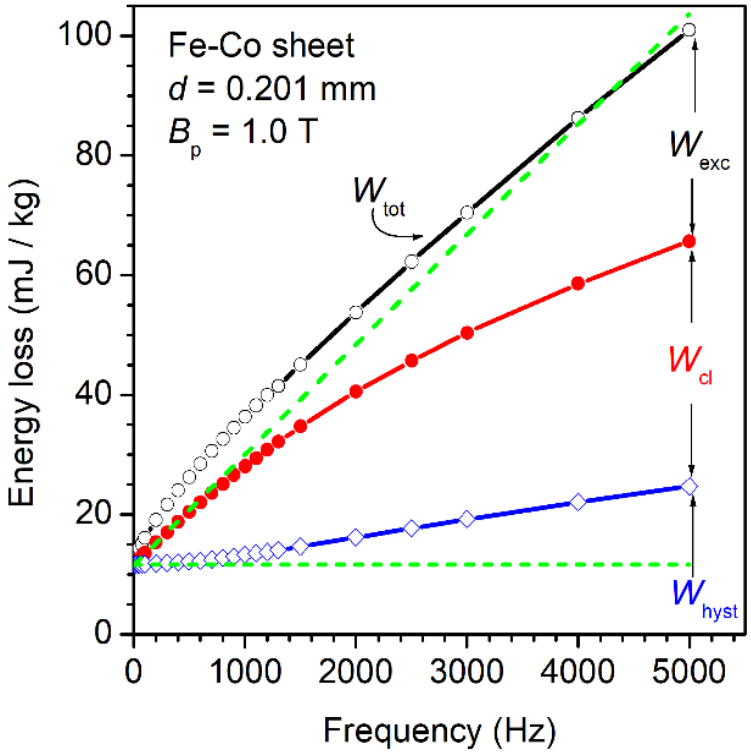

Figure 7.5: Broadband loss analysis in the 0.201 mm thick Fe-Co sheets of Figure 7.4, carried out under sinusoidal induction of peak value B_p = 1.0 T up to 5 kHz. $W_{hyst}(f)$ and $W_{cl,SIN}(f)$ are calculated using (7.12) and (7.13), based on the assumption of a constitutive $B(H)$ equation defined in terms of complex permeability. To note the increase of W_{hyst} and the non-linear behavior of $W_{cl,SIN}$ versus frequency. The dashed lines show the frequency dependence of $W_{hyst}(f)$ and $W_{cl,SIN}(f)$ predicted disregarding the skin effect. This actually starts to affect the magnetization process beyond about 800 Hz.

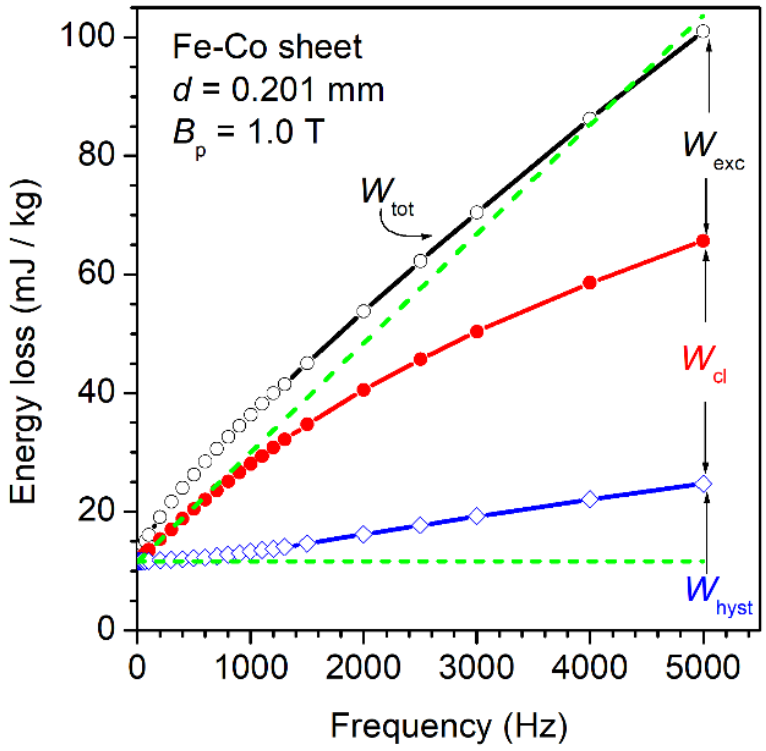

Figure 7.6: As in Figure 7.5 for the 0.194 mm thick non-oriented Fe-Si sheets. The components $W_{hyst}(f)$ and $W_{cl,SIN}(f)$ are calculated using (7.12) and (7.13). The effect of the frequency dependent non-uniform induction profile becomes apparent beyond about 1500 Hz, where the conventional prediction disregarding the skin effect (dashed lines) departs from the abovementioned calculation.

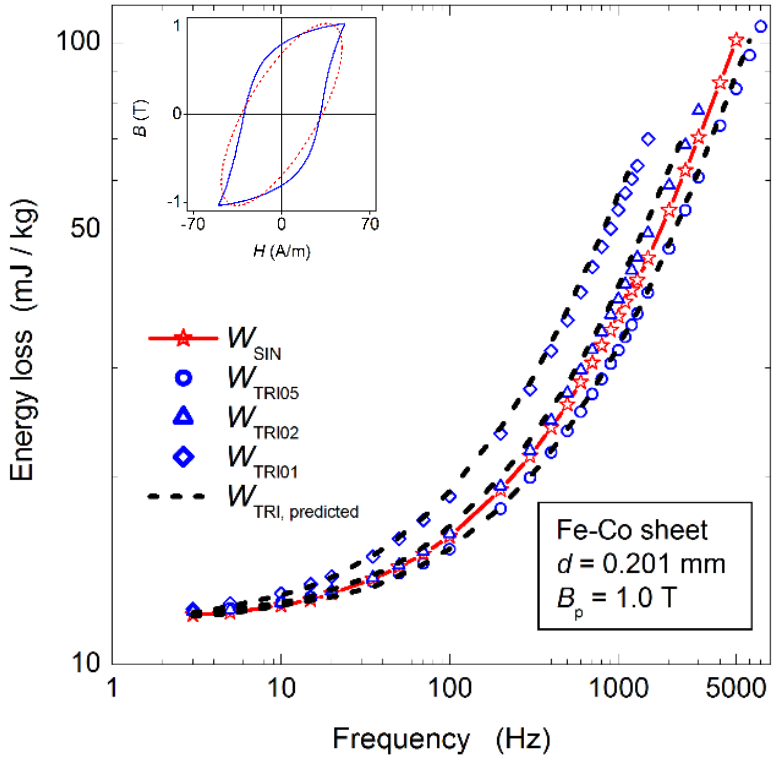

Figure 7.7: The energy loss $W_{SIN}(f)$ measured in the Fe-Co sheets under sinusoidal $B((t)$ for B_p = 1.0 T is compared, up to 5 kHz, with the same quantity, measured at the same B_p value under symmetric triangular ($W_{TRI05}(f)$), and asymmetric triangular $B((t)$, with duty cycles $0.2T$ ($W_{TRI02}(f)$ and $0.1T$ ($W_{TRI01}(f)$ (symbols). The dashed fitting lines ($W_{TRI,predicted}$) are obtained starting from the decomposition of $W_{SIN}(f)$, made according to (7.12) and (7.13), and applying (7.7) twice, for the frequencies $f_1 = 1/(2aT)$ and $f_2 = 1/(2(1-a)T)$, respectively. The inset compares the experimental quasi-static hysteresis loop at B_p = 1.0 T with the equivalent elliptical loop (same B_p value and area), analytically defined through the real μ' and imaginary μ" permeability components.

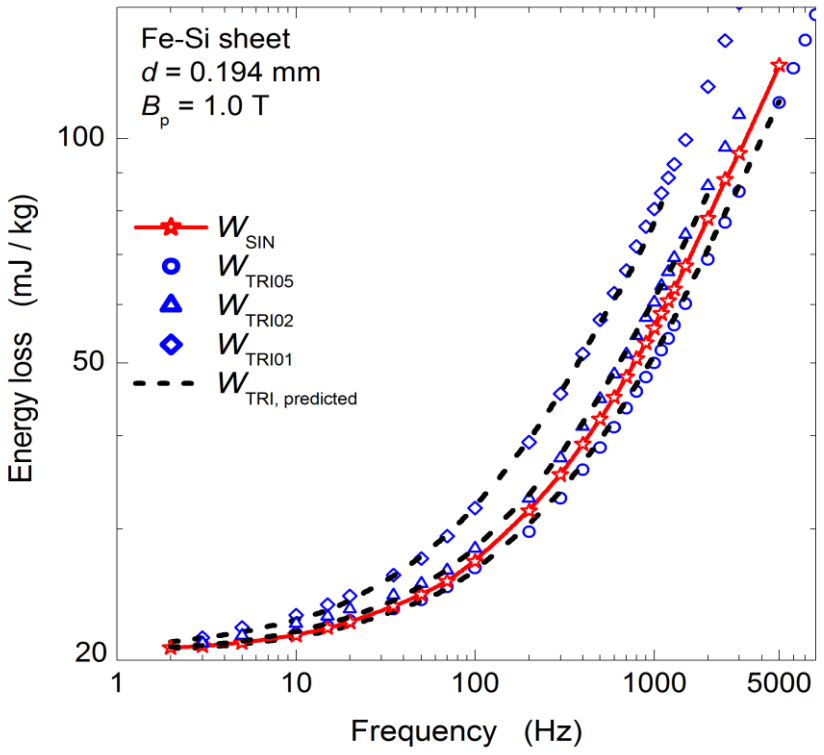

Figure 7.8: The energy loss $W_{SIN}(f)$ measured in the Fe-Si sheets under sinusoidal $B((t)$ for B_p = 1.0 T is compared, up to 5 kHz, with the same quantity, measured at the same B_p value under symmetric triangular ($W_{TRI05}(f)$), and asymmetric triangular $B((t)$, with duty cycles $0.2T$ ($W_{TRI02}(f)$ and $0.1T$ ($W_{TRI01}(f)$ (symbols). The dashed fitting lines ($W_{TRI,predicted}$) are obtained starting from the decomposition of $W_{SIN}(f)$, made according to (7.12) and (7.13), and applying (7.7) twice, for the frequencies $f_1 = 1/(2aT)$ and $f_2 = 1/(2(1-a)T)$, respectively. The inset compares the experimental quasi-static hysteresis loop at B_p = 1.0 T with the equivalent elliptical loop (same B_p value and area), analytically defined through the real μ' and imaginary μ" permeability components.

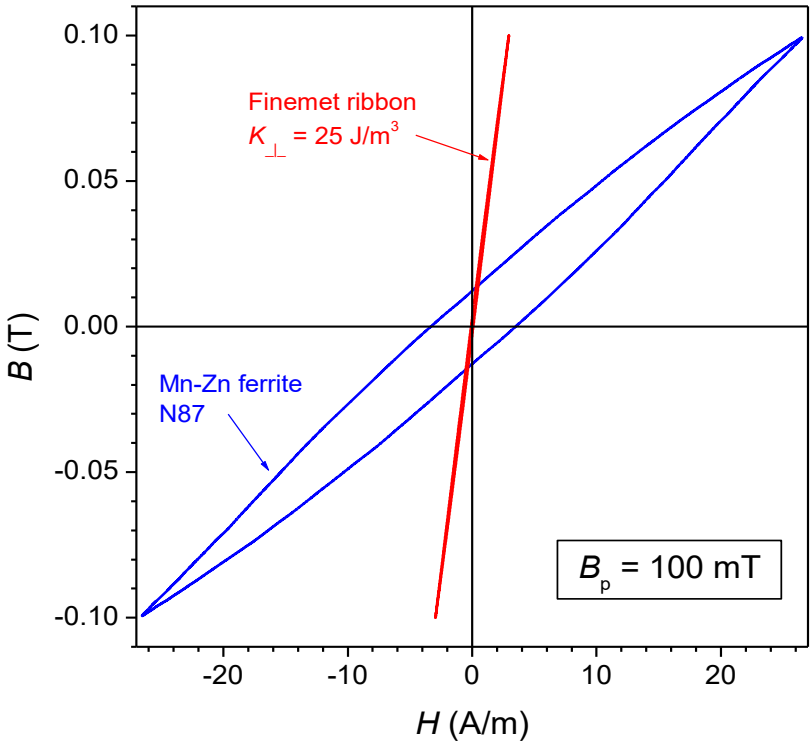

Figure 7.9: DC hysteresis loops of the investigated Mn-Zn ferrites and transverse anisotropy nanocrystalline Finemet ribbons at B_p = 0.1 T. We describe their evolution with frequency in terms of complex permeability, so that the energy loss $W(B_p, f)$ can, in particular, be expressed by (7.2).

7.3.2 Nanocrystalline ribbon and Mn-Zn ferrite Broadband analysis

anisotropy nanocrystalline ribbons and the Mn-Zn ferrites extend deeply in the MHz region, as shown in Figure 7.3. Here, in particular, one can appreciate the excellent frequency response of the nanocrystalline samples, which combine high Snoek's product with low losses at all frequencies. The low value of the anisotropy constant and the ensuing prominent role of magnetization rotations are indeed instrumental in promoting such behavior of Mn-Zn ferrites and nanocrystalline alloys. However, the quantitative assessment of the loss properties over the many-decade frequency range useful for applications reveals a complex task. To simplify the matter, quasi-linear DC constitutive equation is therefore assumed, so that the concept of complex permeability and related energy loss, according to (7.2), applies [70], [71], [72]. The shape of the actually measured DC hysteresis loops (B_p = 0.1 T), shown Figure 7.10, ensures that the description of their frequency evolution in terms of complex permeability provides a good approximation.

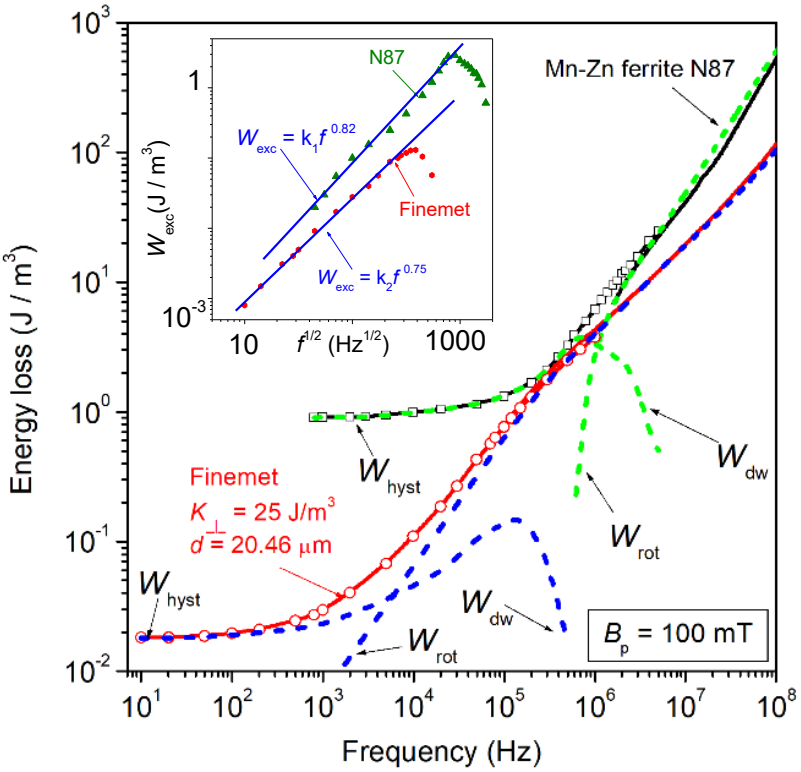

Figure 7.10: Loss decomposition up to 100MHz in the N87 Mn-Zn ferrite and in the transverse anisotropy ($K_\perp$ = 25 J/m^3) nanocrystalline Finemet ribbon (sinusoidal $B(t)$). The experimental $W(f)$ is shown by symbols (fluxmetric) and solid lines (VNA). The rotational loss component W_{rot}, which plays the role of classical loss W_{cl}, is theoretically predicted and separated from the domain wall contribution $W_{dw} = W_{hyst} + W_{exc}$. W_{dw} is bound to decrease and eventually disappear at high frequencies, following the relaxation of the domain wall displacements. The excess loss $W_{exc} = W_{dw} - W_{hyst}$., shown in the inset, displays a power law dependence on frequency $W_{exc} \propto f^n$, with $n > 0.5$.

Fast stroboscopic Kerr observations performed on the transverse anisotropy nanocrystalline ribbons show a relatively sharp transverse domain structure and both rotational and dw processes in response to an applied longitudinal AC field [73]. The activity by the transverse dws is caused by magnetostatic conditions at the ribbon edges evolving with the field amplitude. The dw displacements, which do not contribute to net sample magnetization, are observed to progressively relax under increasing frequency, eventually coming to a halt on approaching the MHz range. Here, only the rotations survive. Consequently, the loss phenomenology attains a classical character, the one pertaining to a quasi-homogeneous rotational process. We note, however, that the slope of the $W(f)$ curve in the MHz range (Figure 7.3) is higher than the $f^{1/2}$ law predicted by the Maxwell's equations for the investigated metallic ribbons . Such a power law would be in fact expected to hold beyond about 1 MHz, where the skin effect is predicted to appear, according to (7.9) and the value of the DC permeability $\mu_{r,DC} = 27 \cdot 10^3$. Actually, we know that the magnetic constitutive equation pertaining to the rotations evolves at high frequencies in obedience to the Landau-Lifshitz (LL) equation [74]. By introducing then the solution of the LL equation, expressed in terms of complex permeability, in the Maxwell's diffusion equation (7.11), we can eventually derive an analytical expression for the rotational classical loss $W_{rot}(B_p, f)$. This approach is fully discussed in [71]. It leads to the loss decomposition procedure for sinusoidal induction, shown up to 100 MHz in Figure 7.10, where we separate $W_{rot}(f)$ from the d.w. contribution $W_{dw}(f)$ by subtracting it from the measured loss $W_{dw}(f) = W(f) - W_{rot}(f)$. We note in Figure 7.10 the drop of $W_{dw}(f)$ beyond a few hundred kHz, following the relaxation of the dw processes. We can further subdivide $W_{dw}(f)$ into the static and dynamic loss components $W_{dw}(f) = W_{hyst} + W_{exc}(f)$. The latter is shown in the inset of Fig. 10. It exhibits a power law dependence on frequency $W_{exc}(f) \propto f^{0.75}$, against the typical $W_{exc}(f) \propto f^{0.50}$ displayed by the steel sheets in the absence of skin effect (see Figure 7. 4b).

There are good phenomenological similarities between the magnetic loss behavior of the transverse anisotropy nanocrystalline ribbons and the sintered Mn-Zn ferrites, because of a similarly important role of the moment rotations. In ferrites, rotations are favored by the intrinsically low value of the magnetocrystalline anisotropy, ensuing from the phenomenon of anisotropy compensation [75]. But the major dissipation mechanism in ferrites is related to the spin damping and the eddy currents play a role only at very high frequencies in sufficiently large samples [70]. Again, the LL equation is invoked for dealing with the rotational processes. Real and imaginary rotational permeabilities are calculated as solutions of the LL equation by assuming distributed effective anisotropy fields, that is, ferromagnetic resonance frequencies changing from grain to grain. The rotational (classical) loss $W_{\mathrm{rot}}(B_{\mathrm{p}}, f)$ is then obtained with (7.2), after suitable integration over the distribution functions for amplitude and orientation of the anisotropy fields. A detailed discussion on the physical assumptions and the performed calculations, including the possible contribution by eddy currents in sufficiently thick specimens, is given in [70] [72]. Figure 7.10 shows the so-obtained loss decomposition in the N87 Mn-Zn ring samples. $W_{\mathrm{dw}}(f)$ drops beyond a few MHz, denoting full relaxation of the dw processes. It is also noted that $W_{\mathrm{exc}}(f) \propto f^{0.82}$.

With the so-calculated loss components W_{hyst}, $W_{\mathrm{rot,SIN}}(f)$ (i.e. $W_{\mathrm{cl,SIN}}(f)$), and $W_{\mathrm{exc,SIN}}(f)$, we apply again (7.7), in order to predict $W(f)$ in the nanocrystalline and ferrite samples under triangular symmetric and asymmetric $B(t)$. W_{hyst} is independent of frequency and $B(t)$ waveshape. Non-uniform induction profile due to the skin effect can in fact be safely excluded, at least in the frequency range where the contribution by W_{hyst} is not negligible . Eddy current losses are actually shown to play a role in the 5 mm thick N87 ferrite samples only beyond a few MHz. At the same time, the skin effect in the nanocrystalline ribbon is restrained by the exchange field [76]. In order to derive $W_{\mathrm{TRI}}(f)$ from the decomposed $W_{\mathrm{SIN}}(f)$

we start by posing $W_{rot,TRI}(f) = (8/\pi^2)\cdot W_{rot,SIN}(f)$, a simplifying and relatively crude approximation for the Mn-Zn ferrite, where the slope of the predicted $W_{rot,SIN}(f)$ undergoes a rapid change around 1-2MHz. We take then k_{exc} according to (7.8) and the obtained power law $W_{exc,SIN}(f) \propto f^{p}$ (inset in Fig. 10), to find $k_{exc} = 0.86$ and $k_{exc} = 0.84$ for the nanocrystalline and Mn-Zn samples, respectively. The losses for triangular symmetric and asymmetric induction are finally calculated through (7.7) and compared with the experimental $W_{TRI05}(f)$, $W_{TRI02}(f)$, and $W_{TRI01}(f)$ behaviors, as shown in Figure 7.11 and Figure 7.12 for the nanocrystalline and the Mn-Zn samples, respectively.

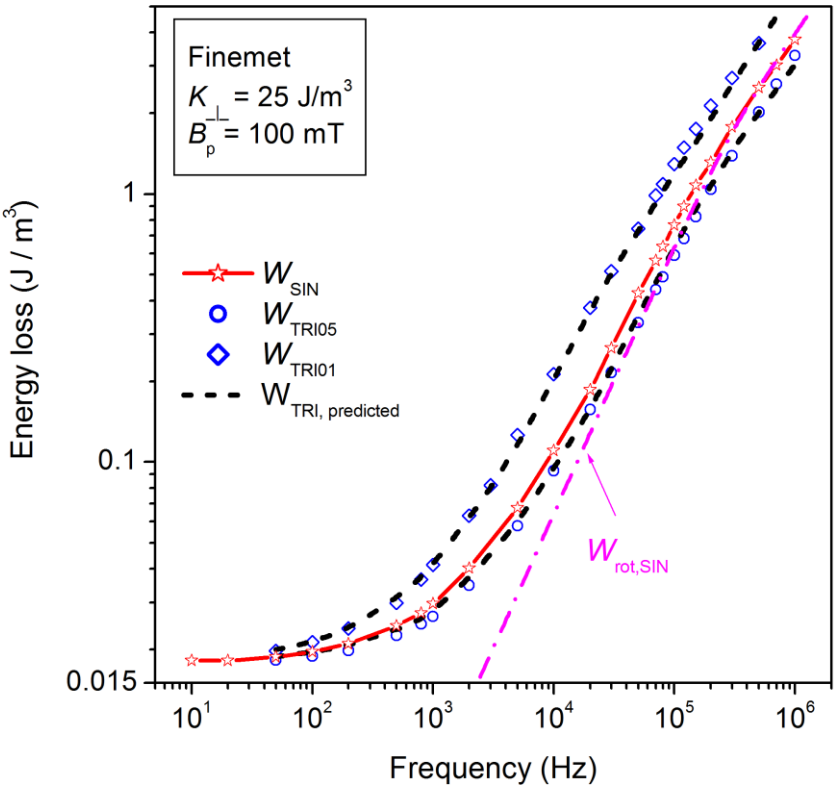

Figure 7.11: The broadband (DC - 1 MHz) energy loss behavior at B_p = 100 mT under triangular symmetric (W_{TRI05}) and asymmetric (W_{TRI01}, duty cycle a = 0.1) induction, measured in the nanocrystalline Finemet transverse anisotropy tapewound ring sample (symbols), is compared with the same quantity $W_{SIN}(f)$ (line and symbols) measured with sinusoidal induction. By making the loss decomposition of $W_{SIN}(f)$, illustrated in Figure 7.10, and applying (7.7), $W_{TRI05}(f)$ and $W_{TRI01}(f)$ are predicted (dashed lines).

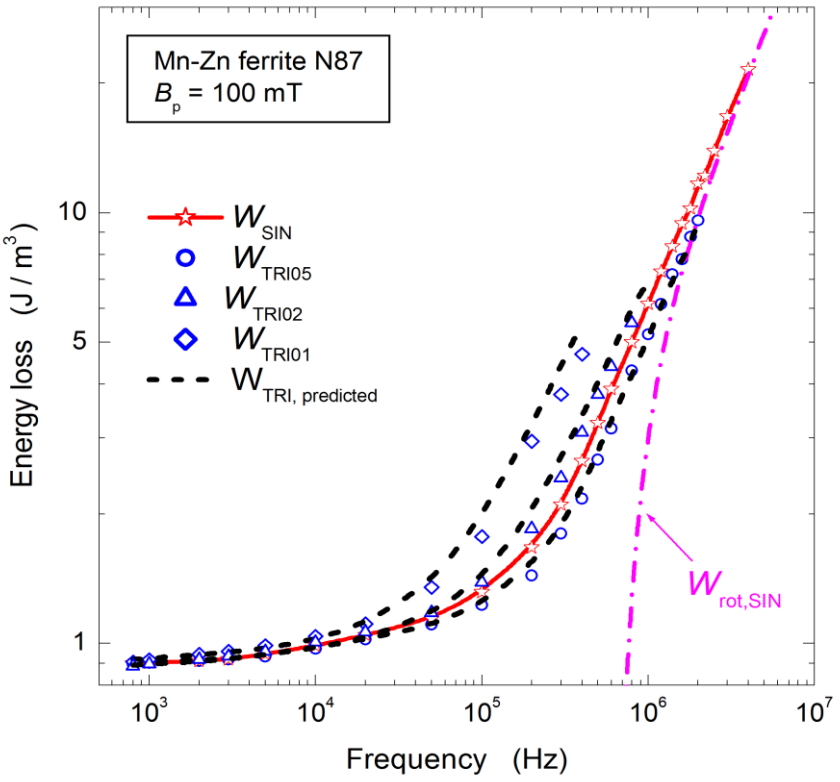

Figure 7.12: Same as Fig. 11 for the Mn-Zn ferrite. Besides the loss under triangular symmetric induction $W_{TRI05}(f)$, the same quantity for asymmetric induction, with duty cycles a = 0.2 ($W_{TRI02}(f)$) and a = 0.1 ($W_{TRI01}(f)$) is measured (symbols) and predicted (dashed lines), starting from the loss components of $W_{SIN}(f)$ and applying (7).

It might be argued that the here proposed method would not fully cover the case where a DC field bias is applied to the magnetic core. However, this problem can be mitigated to some extent. Regarding the Fe-Si sheets, we can estimate, based on the study reported in [19], which shows that the bias mainly affects W_{hyst}, that at intermediate frequencies (say around 2 kHz) and J_{bias} = 0.75 T, we can expect an increase of the loss of the order of 5 % for $J_p = \pm$ 1.0 T. In the Fe-Co the

increase should be lower, of the order of 2 %, for a same J_p swing and J_{bias} = 1.5 T. Negligible variation is expected in the nanocrystalline ribbons, because of their extended $J(H)$ linearity, while a substantial effect might be appreciated in the Mn-Zn ferrites. It is nevertheless important to stress that the classical loss component $W_{cl}(J_p, f)$, (be it due to eddy currents or spin damping) is quite independent of the field bias. Consequently, it suffices to measure $W(f)$ under DC bias and sinusoidal induction and calculate $W_{rot,SIN}(J_p, f)$, as previously discussed, to achieve loss separation. It is then an easy matter to pass, according to (7), to the symmetric/asymmetric square voltage regime. Such a regime, with its extended harmonics spectrum, would prove quite challenging for direct measurements. Good practical advantage is thus achieved by relying on the much more affordable sinusoidal induction measurement.

7.4 Conclusion

Symmetric and asymmetric squared voltage waveforms are frequently imposed on inductive components for power electronics. The usual approach to the prediction of the magnetic losses under such working conditions is based on a suitable generalization of the Steinmetz's equation. The fully empirical character of such equation calls, however, for the introduction of a range of fitting parameters, depending on peak induction level, frequency, and duty cycle. Besides bearing undistinguished scientific value, this method results into somewhat restricted domain of application under a reasonably restricted range of parameters. In this work, we demonstrate that, starting from the physical background provided by the Statistical Theory of Losses and the associated concept of loss decomposition, we can provide a good predicting approach to the frequency dependence of the magnetic losses under symmetric and asymmetric triangular induction, upon a remarkably broad range of frequencies and with different types of soft magnetic materials. We show, in particular, that this is

achieved using only basic knowledge of the material response under sinusoidal flux (i.e. voltage), by which the loss components (hysteresis, classical, and excess) are derived. Such a response is, in turn, predictable with minimum information on the Fe-Si and Fe-Co sheets (conventional measurement of the quasi-static hysteresis loop and the energy loss at 50 Hz), while broadband fitting for sinusoidal flux is desirable in the Mn-Zn samples and the nanocrystalline alloy. The fundamental step, in any case, is the derivation of the classical loss, for which analytical formulation is provided.

Fe-Si and Fe-Co non-oriented sheets have been characterized up to about 5 kHz at peak induction B_p = 1.0 T. By entering the kHz range, skin effect takes place in these sheets. Consequently, modelling is performed exploiting the additional knowledge of the DC hysteresis loop and the best fitting of it using the complex permeability. This plays the role of constitutive magnetic equation, to be used in the calculation of the classical loss $W_{cl,SIN}(f)$ by the Maxwell's diffusion equation.

Transverse anisotropy nanocrystalline ribbons and Mn-Zn ferrite samples have been measured at B_p = 100 mT up to about 1 MHz. Again, loss decomposition for sinusoidal $B(t)$ is performed, but the calculation of $W_{cl,SIN}(f)$ upon the involved high-frequency range calls for the calculation of the dynamic constitutive equation of the material. This concerns, in particular, the rotational processes, largely prevailing on the domain wall displacements. We thus obtain the complex permeability versus frequency as a solution of the Landau-Lifshitz equation. This provides a frequency dependent magnetic constitutive equation. With the loss components for sinusoidal voltage at our disposal, the response of the material to imposed symmetric and asymmetric square-wave voltage can thus be predicted, making use of a couple of known constants. The role of the DC field bias, though not explicitly accounted for, is predictably decreasing with increasing frequencies and can be approximately estimated relying on the determination of

the bias-independent classical loss under sinusoidal voltage and the ensuing loss separation.

Chapter 8

Effect of punching and water-jet cutting methods on magnetization curve and energy losses of non-oriented magnetic steel sheets

8.1 Introduction

Non-oriented fully processed magnetic steel sheets are assembled to form the core of the rotating machines after a cutting operation, without intervening stress-relief annealing. The degradation of the magnetic properties introduced by cutting, especially important across the stator teeth [77], is well recognized and is empirically accounted for in the machine design by introducing a building factor. The direct detrimental consequence of cutting is the relevant magnetic hardening of the region close to the cutting line, which propagates in the sheet through residual stresses up to a few millimeters from the cutting edge [78-81]. This

additionally imposes, especially at low inductions, a non-uniform magnetization profile across the width of the cut strip.

The complex problem of modelling the effect of cutting on the magnetic losses is tackled in general by numerical methods [77] [81-83], focusing on the induction profile and the retrieval of the loss contributions from the damaged and the undamaged regions. Little or no attempt is made to separately determine and physically assess the loss components [83-85].

We have measured the magnetic properties of two different types of non-oriented Fe-Si sheets, where strip samples of widths ranging between 5 mm and 30 mm have been obtained either by conventional guillotine punching or abrasive water-jet cutting. DC magnetization curves and energy losses at peak polarization values 1.0 T and 1.5 T up to 400 Hz have been determined versus strip width and analyzed according to the statistical theory of losses (STL). It is shown that a simple inverse dependence on the strip width can fully describe the behavior of normal magnetization curve and hysteresis loss, whatever the cutting method. One can predict in this way, from a minimum set of measurements, how these quantities evolve from pristine conditions to full material degradation in narrow cut strips. The dynamic loss behavior is in turn interpreted, following the STL, in terms of distribution of the local coercive fields [86].

8.2 Experimental Results and Discussion

8.2.1 Sample preparation and loss measurements.

Non-oriented Fe-(3 wt%)Si 0.638 mm thick (M400-65A) and 0.470 mm thick (M400-50A) magnetic sheets were cut as 300 mm long strips using either an in-house guillotine or an abrasive water- jet machine (MAXIEM 1530, 0.2 mm diameter garnet particles). 300 mm long strips of width w = 30, 15, 10, 7.5, and 5 mm were prepared. They were measured using a single strip tester, where a 300

mm long 30 mm wide sample, made placing side-by-side the appropriate number of strips, according to their width, was inserted between the pole faces of a flux-closing double-C laminated yoke, built of 0.30 mm thick grain-oriented Fe-Si sheets. The magnetic field, supplied by a 173-turn solenoid, was associated with a 150 mm magnetic path length, equal to the distance between the pole faces of the yoke. The secondary voltage was detected by a 20 mm long 101-turn pickup coil placed at the center of the strip under test. Hysteresis loops and losses were measured under sinusoidal induction in the frequency range 2 Hz – 400 Hz by means of a calibrated hysteresisgraph-wattmeter, endowed with digital control of the induction waveform [87] and using a 12-bit 500 MHz HDO4054 LeCroy oscilloscope for signal acquisition. Energy loss $W(f)$ versus frequency behaviors were obtained at the peak polarization values J_p = 1.0 T and 1.5 T.

By cutting the strip samples at decreasing widths, increase of the energy loss, ensuing from a correspondingly higher proportion of strain-hardened material, is always observed upon the whole frequency range, as shown in the example of Figure 8.1, concerning the guillotine punched M400-50A sheet. Stronger relative deterioration is observed for J_p = 1.0 T. Quite similar behaviors are displayed by the losses measured on the punched M400-65A sheet, while in all cases milder magnetic hardening is demonstrated upon cutting by the water-jet method. The lowest-lying $W(f)$ curves (strip width w = 30 mm) are subjected in Figure 8.1 to a decomposition procedure, where it is posed $W(f) = W_h + W_{cl}(f) + W_{exc}(f)$, with W_h, $W_{cl}(f)$, and $W_{exc}(f)$ the hysteresis (quasi-static), classical, and excess loss components, respectively. Here the classical loss is calculated according to the following standard formula, assuming uniform induction across the sample cross-section [84], then

$$W_{cl}(f) = (\pi^2/6)\cdot(\sigma d^2 J_p^2 f/\delta), \qquad \text{[J/kg]} \tag{8.1}$$

where d is the sheet thickness, δ is the density of the material, and σ is the conductivity. These quantities are all unaffected by cutting (see Table 8.1). Equation (8.1) requires some comments. First, it is noted that, with the field

strengths involved in the present experiments, the induction B_p, usually appearing in this equation, coincide with the polarization J_p. It is also remarked that Eq. (8.1) calls for uniform induction across the sample cross-section and cannot be applied beyond a critical frequency f_s, where the skin effect cannot be neglected. f_s is identified by analyzing the frequency dependence of $W_{exc}(f)$ according to the STL [33]. It is f_s slightly larger than 300 Hz for the measurements shown in Fig. 1. It is finally stressed that the approximation of indefinitely extended sheet, required for formulating Eq. (8.1), generally applies [13], because the strip width is always $w >> d$. This condition also justifies the use of the measured J_p in Eq. (8.1), neglecting the decrease of the local polarization value at the cold-worked strip edges. In fact $W_{cl}(f)$ chiefly relates to the dissipation by the surface eddy currents, which depend on the total measured flux rate of change throughout the whole sample cross-section.

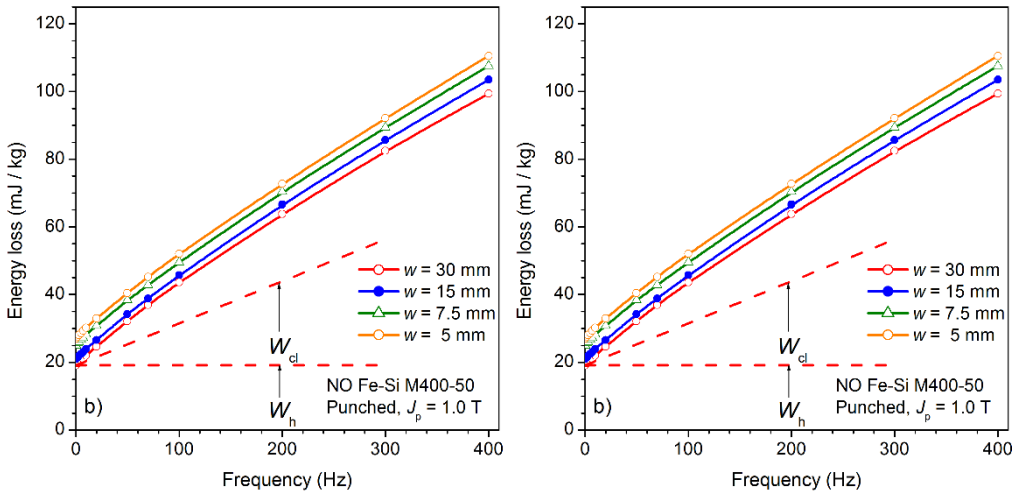

Figure 8.1:Non-oriented M400-50A NO Fe-Si sheets. Energy loss versus frequency measured at peak polarization J_p = 1.5 T (a) and J_p = 1.0 T (b) on strip samples cut by guillotine punching. The strip widths w range between 5 mm and 30 mm. The inset provides a magnified view of the low frequency results. Loss decomposition is sketched for the 30 mm wide strip.

Table 8.4: Physical parameters of the investigated non-oriented steel sheets

Non-oriented Fe-(3 wt%)Si steel sheet	Thickness d (mm)	Density δ (kg/m^3)	Resistivity ρ (Ω m)	Grain size $\langle s \rangle$ (μm)
M400-65A	0.638	7650	$44.0 \cdot 10^{-8}$	97
M400-50A	0.470	7700	$42.0 \cdot 10^{-8}$	127

8.2.2 Quasi-static magnetic behavior

The detrimental effect of cutting on the magnetic properties of the Fe-Si sheets is apparent in the evolution of the measured normal magnetization curves versus strip width shown in Figure 8.2a (M400-65A sheet, symbols). Progressive deterioration of the magnetic permeability upon decreasing width is in fact observed, consistent with the increase of the hysteresis loss W_h (i.e. coercive field) shown in Figure 8.1. Such evolution can be quantitatively understood by schematically assuming that cutting generates two narrow bands of strain-hardened material at the strip edges (see inset of Figure 8.2b) [78,81,83]. By approximating the decline of the magnetization across such bands with a step-like function, we identify, for any given field H, the magnetization values J_{pc} in the hardened side bands of width L_c and J_{p0}, with $J_{p0} > J_{pc}$, across the inner unscathed region of width $w_0 = w - 2L_c$. The measured magnetization J_p, obtained as the weighted sum of J_{p0} and J_{pc}, follows then an inverse dependence on w

$$J_p = J_{p0} - (J_{p0} - J_{pc}) \cdot \frac{2L_c}{w} \quad , \tag{8.2}$$

under the condition $w \geq 2L_c$, where $J_p = J_{pc}$ for $w \leq 2L_c$. Consequently, by measuring the magnetization curve at two generic strip widths, one can calculate the quantities J_{p0} and $(J_{p0} - J_{pc})\cdot L_c$ as a function of H for any width and trace the fitting curves given by Eq. (2). They are shown in the examples provided in Figure 8.2b, corresponding to different H values. The J_p values measured on the experimental $J(H)$ curves for the different widths w (symbols) are here observed to follow to very good extent the hyperbolic function (8.2). We then see how, for $w >> 30$ mm, the limiting normal magnetization curve $J_{p0}(H)$ associated with the pristine material (upper dashed curve in Figure 8.2a) can be retrieved. The width $2L_c$ at which the strip becomes fully degraded can also be approximately predicted, as sketched in Figure 8.2b. We estimate $2L_c \sim 4.2$ mm for the punched M400-65A sheets. The lowest lying magnetization curve in Figure 8.2a (dashed line) is correspondingly calculated with Eq. (2) ($w = 2L_c = 4.2$ mm). Pretty similar results are obtained in the punched sheet M440-50A. Figure 8.3 shows that an identical interpretative scheme applies to the effect of abrasive water-jet cutting. It points to reduced magnetic hardening and degraded width $2L_c = 3.2$ mm, compared to punched strips

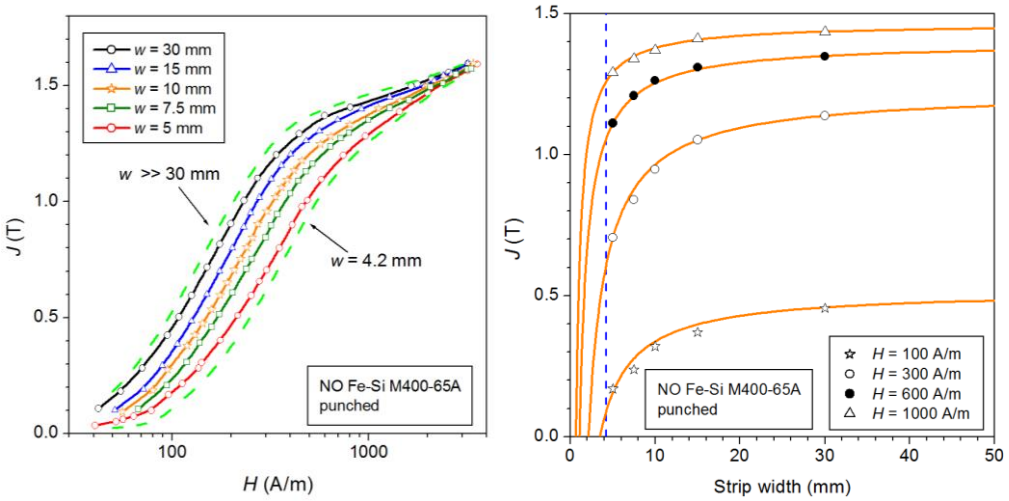

Figure 8.2: a) DC normal magnetization curves measured versus width w of the punched strips in the NO Fe-Si M400-65A sheets (transverse direction, symbols). b) The polarization values (symbols) measured under defined field strengths H decrease with decreasing strip width w according to the hyperbolic law (8.2) (solid lines). This law is obtained assuming the simplified scheme shown in the inset, where the damaged region of the strip is confined to the two lateral bands of width L_c, where $J_{pc} < J_{p0}$. The dashed lines in a) are the magnetization curves predicted by Eq. (8.2) for undamaged ($w >> 30$ mm) and fully damaged ($w = 4.2$ mm) cut strips.

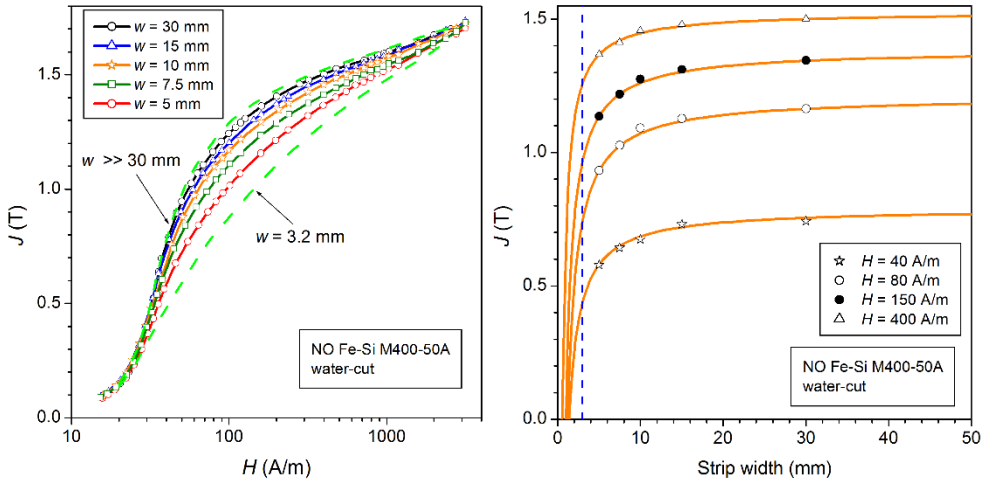

Figure 8.3: Normal magnetization curves obtained in the NO Fe-Si M400-50A sheets subjected to abrasive water-jet cutting (rolling direction). a) Measured DC normal magnetization curves and their limiting behaviors ($w >> 30$ mm and $w = 2L_c = 3.2$ mm, dashed lines). b) Symbols: polarization values measured under given field strengths. Solid lines: evolution of the polarization with the strip width w under defined field H predicted by Eq. (8.2).

A same conclusion is drawn from the behavior of the hysteresis (quasi-static) loss W_h, a quantity directly connected with the coercive field. It is obtained by extrapolating the $W(f)$ curves to $f \rightarrow 0$. Using again the simplifying scheme previously adopted for predicting J_p versus w, according to Eq. (8.2), we relate the measured loss density W_h to the contributions W_{h0} and W_{hc} pertaining to the unscathed and damaged regions, respectively

$$W_h = W_{h0} + (W_{hc} - W_{h0}) \cdot \frac{2L_c}{w}, \tag{8.3}$$

for $w \geq 2L_c$. The overall dependence of W_h on w, measured upon both punching and water-jet cutting at J_p = 1.5 T and 1.0 T in the M440-65A and M440-50A

sheets, is shown in Figure 8.4. The experimental normalized value $W_{h,norm} = W_h/W_{h0}$ is in particular represented here (symbols). It follows the hyperbolic dependence on w predicted by (8.3) using the previously estimated width L_c (Figure 8.2 and 8.3) of the strain-hardened band. The upper limit W_{hc} predicted for the fully damaged strip is then obtained as shown in Figure 8.4a and 8.4b. One can remark the lower magnetic deterioration brought about by water-jet cutting with respect to punching and, consistent with the behavior of the magnetization curves (Figure 8.2a and 8.3a), the larger relative increase occurring at $J_p = 1.0$ T. We observe indeed that the normal curves tend to coalesce around and beyond $J_p = 1.5$ T, revealing the participation at high inductions of the upper tail of the distribution of the local coercive fields and the nascent role of the magnetization rotations. Both phenomena are negligibly affected by strain hardening.

8.2.3 Excess losses

Having clarified the role of the classical loss component, basically unaffected by the cutting operation, we analyze the effect of cutting on the dynamic losses by focusing on the excess loss $W_{exc}(f) = W(f) - W_{cl}(f) - W_h$, where $W_{cl}(f)$ is given, at frequencies lower than the threshold for the occurrence of the skin effect, by Eq. (8.1). The general outcome of the experiments is that also $W_{exc}(f)$ tends to increase upon sheet cutting, again to a larger relative extent at $J_p = 1.0$ T. The excess loss descends from the discrete nature of the magnetization process, which is theoretically incorporated in the concept of “magnetic objects” (MO) and the distribution of their local coercivities [86]. Figure 8.5 provides examples of the evolution of $W_{exc}(f)$ versus strip width in the punched M440-65A and M440-50A sheets (symbols), The dashed fitting lines are calculated, according to Ref. [33], by the equation

$$W_{\mathrm{exc}}(f) = 2n_0 V_0 J_{\mathrm{p}} \cdot \int_0^{\pi/2} \left(\sqrt{1 + \frac{8\sigma G S V_0}{n_0^2 V_0^2} \pi f J_{\mathrm{p}} \cos\phi} - 1 \right) \cos\phi \, \mathrm{d}\phi \ , \tag{8.4}$$

where n_0 is the number of MOs simultaneously active in the sample cross-sectional area S in the limit $f \to 0$ and $G = 0.1356$. V_0 is a statistical parameter associated with the distribution of the local coercive fields for the MOs. n_0 and V_0 are experimentally identified by finding $W_{\mathrm{exc}}(f)$ as $W_{\mathrm{exc}}(f) = W(f) - W_{\mathrm{h}} - W_{\mathrm{cl}}(f)$ and plotting the number n of MOs, obtained as $n = 4\sigma G S J_{\mathrm{p}} / H_{\mathrm{exc}}$, where $H_{\mathrm{exc}} = W_{\mathrm{exc}}(f) / 4J_{\mathrm{p}}$, versus H_{exc} [10]. At frequencies lower than the threshold for the skin effect, $n(H_{\mathrm{exc}})$ satisfies the linear relationship $n(H_{\mathrm{exc}}) = n_0 + H_{\mathrm{exc}} / V_0$ and from intercept and slope of this straight line we obtain the values of the parameters n_0 and V_0. Examples of this procedure are discussed in Refs. [33]. V_0 depends on the coercivity of the material and the character of the domain structure, the wider the domain wall spacing the larger V_0. The effect of strain hardening by cutting is likely one of increasing, on the average, the parameter V_0, following the increase of the coercive field, that is, of W_{h} (Figure 8.4). This is what fitting of $W_{\mathrm{exc}}(f)$ by Eq. (8.4) reveals. For example V_0 increases from $V_0 \cong 0.2$ A/m to $V_0 \cong 1.8$ A/m in the punched M400-65A sheets on passing from $w = 30$ mm to $w = 5$ mm. It is observed in Figure 8.5 that Eq. (8.4) provides excellent fitting of $W_{\mathrm{exc}}(f)$ up to a limiting frequency, where the skin effect is appreciated and the Eq. (8.1) for the classical loss component becomes inaccurate. Fitting of $W_{\mathrm{exc}}(f)$ by Eq. (8.4), while expectedly affected by earlier deviation in the thicker sheets (Figure 8.a), provides a simple tool for detecting the appearance of the skin effect.

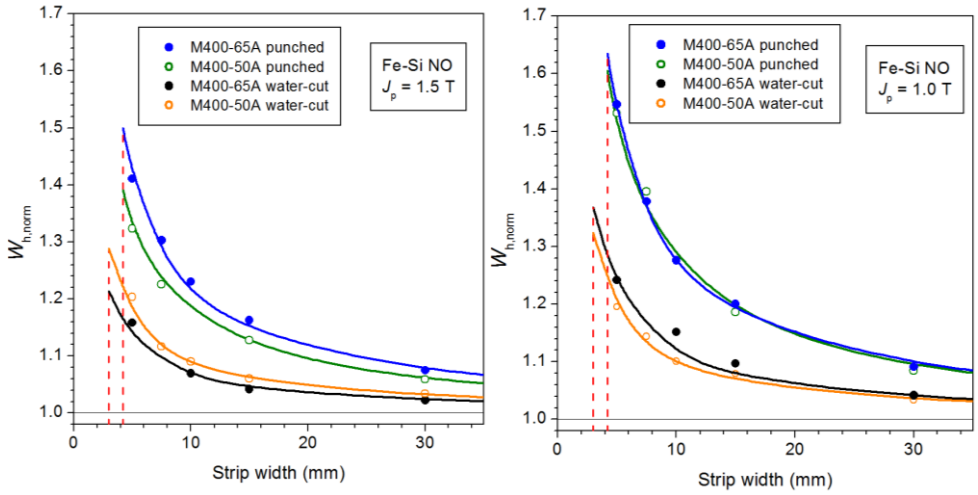

Figure 8.4: Measured hysteresis loss $W_{h,norm} = W_h / W_{h0}$ (symbols), normalized to the loss value predicted for the pristine sheet, versus strip width. Both punched and water-jet cut sheets are considered at J_p = 1.5 T and 1.0 T. The continuous lines are predicted by Eq. (3). The vertical dashed lines identify the upper loss limit, which corresponds to the fully damaged strip of width $2L_c$.

8.3 Conclusions

The detrimental effect of strip cutting by guillotine punching and water jet abrasion on the magnetization curve and energy losses in non-oriented Fe-Si sheets can be assessed by a simple interpretative scheme, where these quantities evolve as weighted contributions of the damaged bands at the strip edges and the undamaged material portion. A hyperbolic dependence on the strip width of the magnetization at given applied field and of the hysteresis loss (i.e. coercive field) at given peak polarization value is therefore predicted and shown to excellently comply with the experimental results. It is shown, in particular, that the limiting magnetization curves and hysteresis (quasi-static) losses for the fully damaged and the pristine sheets can be retrieved from knowledge of the behavior of these quantities at two generic strip widths. The role of cutting on the dynamic energy losses, measured up to 400 Hz, is assessed by formulating the frequency dependence of the excess loss component according to the statistical theory of losses. This shows that strain hardening by cutting reflects into the statistics of the local coercive fields, eventually leading to increased excess losses.

Chapter 9

Conclusions and Future Research

9.1 Summary

In this thesis, the magnetic materials properties and broadband magnetic loss of traditional non-oriented silicon steel sheets, iron-cobalt-vanadium alloy sheets, Mn-Zn ferrite and nanocrystalline strips are systematically studied. The research results obtained in the thesis are as follows:

(1) In this part, the one-dimensional magnetic characteristics of broadband non-oriented silicon steel sheets and low carbon steels are measured, and the magnetic losses of the two materials under high and low magnetic induction are analyzed. It is proved by experiments that the saturated wave model in the classical loss calculation model is not suitable for predicting the classical loss of these two materials under high magnetic induction intensity, but the statistical loss theory has applicability.

(2) This part discusses the characteristics of pulse width modulation waveform excitation and the method of small hysteresis loop loss prediction, and applies the small hysteresis loop loss prediction method to the total loss prediction

under PWM excitation, using two-stage pulse. The PWM experiment verifies the calculation model of the total loss with nested small hysteresis loops, and the prediction results are in agreement with the experimental results.

(3) The theoretical modelling and experimental verification of the broadband loss of non-oriented silicon steel sheets, iron-cobalt-vanadium alloy sheets, manganese-zinc ferrite and ultra-microcrystalline strips excited by symmetric and asymmetric voltage rectangular waves are presented. A simple method for predicting the magnetic loss under the excitation of symmetric and asymmetric waveforms using the basic data of material response under sinusoidal magnetic induction waveform excitation.

(4) From quasi-static to 400Hz frequency range, the magnetization curve and the loss of non-oriented silicon steel sheets with different cutting widths (5mm~30mm) were measured. The relationship between the magnetization curve, and thus the relationship between the hysteresis loss and the width of the sample is established, and the magnetization curve and hysteresis loss of the same width sample are predicted by less measurement data in consideration of the influence of the cutting on the magnetic properties of the material.

9.2 The main innovations

(1) The systematic and in-depth quantitative research on the statistical loss theory and loss separation is carried out. Through a large number of experiments, the applicability of the loss separation method of the statistical loss theory under high and low magnetic induction is verified. However, some literature stated that the saturation wave model is more suitable for classical loss calculation under high magnetic induction excitation cannot be proved by experiments.

(2) For the loss of soft magnetic materials under the excitation of unconventional magnetic induction intensity waveform (such as PWM wave,

symmetrical triangular wave, asymmetric triangular wave), a calculation model of minor loop considering skin effect is proposed. At the same time, how to derive the broadband loss under asymmetric and symmetric triangular magnetic induction wave excitation is directly derived from the result of standard sinusoidal excitation.

(3) Aiming at quantifying the influence of cutting on material loss, a simplified model is proposed, which the sample is divided into the affected area and the unaffected area by cutting. The relationship between hysteresis loss and sample width under a given applied magnetic field is predicted, and quantitative analysis is also carried out. The effect of different cutting processes on the magnetic properties of non-oriented silicon steel sheets are analyzed.

9.3 Future research

(1) In this thesis, measurement and loss analysis are carried out for non-oriented silicon steel sheets, Fe-Co alloys, nanocrystalline strips and Mn-Zn ferrites, but the types of materials are still needed.

(2) This thesis only focus on one-dimensional magnetic property measurement and loss analysis. The subsequent work should further research on two-dimensional broadband loss modelling.

References

[1] https://climate.nasa.gov/evidence/

[2] International energy outlook 2016. https://www.eia.gov/forecasts/ieo/emissions.cfm. Accessed: 2016-10-04.

[3] Energy-effciency policy opportunities for electric motor-driven systems. http://www19.iadb.org/intal/intalcdi/PE/2011/08825.pdf. Accessed: 2016-09-04.

[4] B.Cullity, C.Graham. Introduction to Magnetic Materials[M] Addison-Wesley. 1972. 11-14.

[5] E.Snelling. Soft Ferrites: Properties and Applications [M]. London: Butter worth and Co. Ltd. 1988. 10-20.

[6] 严密,彭晓领.磁学基础与磁性材料 [M].杭州:浙江大学出版社. 2006. 12-17.

[7] https://www.sciencedirect.com/topics/chemistry/ferromagnetic-material

[8] AJ.Moulson, JM.Herbert. Dielectrics and Insulators[M]. Electroceramics: Materials, Properties, Applications, Second Edition. John Wiley & Sons, Ltd, 2003.

[9] https://www.britannica.com/science/ferrimagnetism

[10] F. Fiorillo, G. Bertotti, C. Appino, M. Pasquale. Soft Magnetic Materials, WILEY ENCYCLOPEDIA OF ELECTRICAL AND ELECTRONICS ENGINEERING, pp. 1-42,M. Peterca Editor,Hoboken, New Jersey:John Wiley & Sons, Inc. (2016)

[11] F. Fiorillo, C. Appino, M. Pasquale. Hysteresis in Magnetic Materials.THE SCIENCE OF HYSTERESIS,Vol. III, Chap. 1, pp. 1-190,Elsevier (Academic Press) Publisher; Amsterdam, Netherlands (2006)

[12] P.Bloch. Zur Theorie des Austauschproblems und der Remanenzerscheinung der Ferromagnetika [M]. Springer Berlin Heidelberg. 1932. 295-335.

[13] L.Néel. Anisotropie magnétique superficielle et surstructures d'orientation [J]. Journal De Physique, 1954, 15(4):225-239.

[14] JF.Dillon, HE.Earl. Domain wall motion and ferrimagnetic resonance in a Manganese ferrite[J]. Journal of Applied Physics, 1959, 30(2): 202-213.

[15] C.Serpico, ID.Mayergoyz, G.Bertotti. Analysis of eddy currents with Landau-Lifshitz equation as a constitutive relation[J]. IEEE Transactions on Magnetics, 2001, 37(5): 3546-3549.

[16] C.Steinmetz. On the law of hysteresis [J]. Transactions of the American Institute of Electrical Engineers, 1892, 9(1): 1-64.

[17] J.Reinert, A.Brockmeyer, and R.De Doncker. Calculation of losses in ferro- and ferromagnetic materials based on the modified Steinmetz equation [J]. IEEE Transactions on Industy Applications, 2001, 37: 1055–1061.

[18] J Mülethaler, J Biela, J Kolar, et all. Improved core loss calculation for magnetic components employed in power electronic systems [J]. IEEE Transactions on Power Electronics, 2012, 27(2): 964–973, 2012.

[19] Preisach F. Über die magnetische Nachwirkung [J]. Zeitschrift fürPhysik, 1935(94): 277-302.

[20] Bernard Y, Mendes E, Bouillault F, et al. Dynamic hysteresis modeling based on Preisach model [J]. IEEE Transactions on Magnetics, 2002, 38(2): 885-888.

[21] Liorzou F, Phelps B, Atherton D. Macroscopic models of Magnetization [J]. IEEE Transactions on Magnetics, 2000, 36(2): 418-428.

[22] Bertotti G. General properties of power losses in soft ferromagnetic materials [J]. IEEE Transactions on Magnetics, 1988, 24(1): 621-630.

[23] Globus A, Monjaras R. Influence of the deviation from stoichiometry on the magnetic properties of Zn-rich NiZn ferrites [J]. IEEE Transactions on Magnetics, 1975, 11(5):1300-1302.

[24] Stoner E, Wohlfarth E. A Mechanism of Magnetic Hysteresis in Heterogeneous Alloys [J]. Philosophical Transactions of the Royal Society of London A: Mathematical, Physical and Engineering Sciences, 1948, 240(826): 599-642.

[25] Jiles DC, Atherton DL. Theory of ferromagnetic hysteresis [J]. Journal of Magnetism and Magnetic Materials, 1986, 61(1): 48-60.

[26] Jiles DC, Thoelke JB, Devine MK. Numerical determination of hysteresis parameters for the modeling of magnetic properties using the theory of ferromagnetic hysteresis [J]. IEEE Transactions on Magnetics, 1992, 28(1): 27-35.

[27] Brockmeyer A. Dimensionierungswerkzeug für magnetische Bauelemente in Stromrichteranwendungen [M]. Verlag der Augustinus-Buchh. 1997.12-20.

[28] Li Jieli, Abdallah Tarek, and Sullivan Charles R. Improved calculation of core loss with nonsinusoidal waveforms [C]. In Industry Applications Conference. Thirty-Sixth IAS Annual Meeting. Conference Record of the 2001 IEEE, 2001. 4: 2203–221.

[29] D. C. Jiles and D. L. Athenon, “Ferromagnetic hysteresis,’’ IEEE Trans. Magn., vol. MAG-19, pp. 2183-2185, Sept. 1983.

[30] F. Preisach, Z. Phys. 94., p. 277 (1935).

[31] D. Everett, “A general approach to hysteresis—Part 4. An alternative formulation of the domain model,” Trans. Faraday Society, vol. 51, pp. 1551–1557, 1955

[32] G. Bertotti, “Dynamic generalization of the scalar Preisach model of hysteresis,” IEEE Trans. Magn., vol. 28, pp. 2599–2601, 1992.

[33] Giorgio Bertotti. Hysteresis in magnetism: for physicists, materials scientists,and engineers. [M]Academic press, 1998.

[34] Pierre Weiss. L’hypothèse du champ moléculaire et la propriété ferromagné-Tique [J]. Journal of Theoretical and Applied Physics, 1907, 6(1):661–690.

[35] Vincent Del Toro. Electric machines and power systems [M]. Prentice Hall Inc., Old Tappan, NJ.1985.0-699.

[36] Williams HJ, Shockley W, and Kittel Ch. Studies of the propagation velocity of a ferromagnetic domain boundary [J]. Physical Review, 1950, 80(6):1090.

[37] Pry R H, Bean C P. Calculation of the Energy Loss in Magnetic Sheet Materials Using a Domain Model [J]. Journal of Applied Physics, 1958, 29(3):532-533.

[38] G.Bertotti. A general statistical approach to the problem of eddy current losses [J]. Journal of magnetism and Magnetic Materials, 1984, 41(1):253–260.

[39] E.Barbisio, F.Fiorillo, C.Ragusa. Influence of phase magnetic couplings on phase current characteristics of multiphase BLDC machines with overlapping phase windings [J]. IEEE Transactions on Magnetics, 2015, 51(9):1-13.

[40] Fiorillo F, Measurements of magnetic materials [J]. Metrologia, 2010.

[41] Methods of measurement of the magnetic properties of electrical steel sheet and strip by means of an epstein frame. IEC Standard Publication 60404-2,1996.

[42] Methods of measurement of magnetic properties of electrical steel strip and sheet at medium frequencies. IEC Standard Publication 60404-10,2016.

[43] Methods of measurement of the magnetic properties of electrical steel strip and sheet by means of a single sheet tester, IEC Standard Publication 60404-3,2009.

[44] Methods of measurement of the magnetic properties of magnetically soft metallic and powder materials at frequencies in the range 20 Hz to 100 kHz by the use of ring specimens, IEC Standard Publication 60404-6,2018.

[45] Zirka S E, Moroz Y I, Steentjes S, et all. Dynamic magnetization models for soft ferromagnetic materials with coarse and fine domain structures [J]. Journal of Magnetism and Magnetic Materials, 2015, 394:229–236.

[46] Wolman W, Kaden H. On the eddy current delay of magnetic switching (in German) [J]. Z. Tech. Phys., 1932, 13:330–345.

[47] Mayergoyz I, Serpico C, “Nonlinear diffusion of electromagnetic fields and excess eddy current”, J. Appl. Phys., vol 85, pp. 4910–4912, 1999.

[48] Fakam M, Hecquet M, Lanfranchi V, et all. Design and magnetic noise reduction of the surface permanent magnet synchronous machine using complex air-gap permeance [J]. IEEE Transactions on Magnetics, 2015, 51(4):1-9.

[49] Takeda Y, Takahashi Y, Fujiwara K, et all. Iron loss estimation method for rotating machines taking account of hysteretic property [J]. IEEE Transactions on Magnetics, 2015, 51(3):7300504.

[50] Jumayev S, Merdzan M, Boynov K, et all. The effect of PWM on rotor eddy-current losses in high-speed permanent magnet machines [J]. IEEE Transactions on Magnetics, 2015, 51(11):8109204.

[51] Gong X and Ferreira J. A. Comparison and reduction of conducted EMI in SiC JFET and Si IGBT-based motor drives [J]. IEEE Transactions on Power Electronics, 2014, 29(4):1757–1767.

[52] X. Yongxiang, Y. Qingbing, Z. Jibin, et all. Periodic carrier frequency modulation in reducing low-frequency electromagnetic interference of permanent magnet synchronous motor drive system [J]. IEEE Transactions on Magnetics, 2015, 51(11):8109604.

[53] C. Beatrice, C. Appino, O. de la Barrière, F. Fiorillo, and C. Ragusa, "Broadband magnetic losses in Fe-Si and Fe-Co laminations," IEEE Trans. Magn., vol. 50, no. 4, Apr. 2014, Art. no. 6300504, doi: 10.1109/TMAG.2013.2286923

[54] Di Capua G and Femia N. A novel method to predict the real operation of ferrite Inductors with moderate saturation in switching power supply [J]. IEEE Transactions on Power Electronics, 2016, 31 (3):2456-2564.

[55] Li J, Abdallah T, and Sullivan C. Improved calculation of core loss with nonsinusoidal waveforms [C]. Industry Applications Conference, 2001, 4:2203-2210.

[56] Venkatachalam K, Sullivan C R, Abdallah T, et all, Accurate prediction of ferrite core losses with nonsinusoidal waveforms using only Steinmetz parameters[C]. Proceeding 8th IEEE Workshop Computor Power Electronic, 2002, 36-41.

[57] Van den Bossche A P, Van de Sype D M, and Valchev V C. Ferrite loss measurement and models in half bridge and full bridge waveforms[C]. Proc. IEEE PESC, 2005, 1535–1539.

[58] Shen W, Wang F, Boroyevic D, et all. IV, Loss characterization and calculation of nanocrystalline cores for high-frequency applications [J]. IEEE Transactions on Power Electronics, 2008, 23(1):475–484.

[59] Barg S, Ammous K, Mejibri H, et all. An improved empirical formulation for magnetic core losses estimation under nonsinusoidal induction [J]. IEEE Transactions on Power Electronics, 2017, 32(3): 2146-2154.

[60] Fiorillo F and Novikov A. An improved approach to power losses in magnetic laminations under nonsinusoidal induction waveform [J]. IEEE Transactions on Magnetics, 1990, 26(5):2904-2910.

[61] Fiorillo F, Appino C and Barisoni M. Power losses in magnetic laminations with trapezoidal induction waveform [J]. Anales de Fisica, 1990, 86: 238-240.

[62] Atallah K, Zhu Z Q, and Howe D. An improved method for predicting iron losses in brushless permanent magnet DC drives [J]. IEEE Transactions on Magnetics, 1992, 28(5):2997-2999.

[63] Amar M and Protat F. A simple method for estimation of power losses in silicon iron sheets under alternating pulse voltage excitation [J]. IEEE Transactions on Magnetics, 1994, 30(2):942- 944.

[64] Kaczmarek R, Amar M and Protat F. Iron loss under PWM voltage supply on Epstein frame and in induction motor core [J]. IEEE Transactions on Magnetics, 1996, 32(1):189-194.

[65] Roshen W. A practical, accurate and very general core loss model for nonsinusoidal waveforms [J]. IEEE Transactions on Power Electronics, 2007, 22(1):30-40.

[66] Hilal A, Raulet M A., Martin C, et all. Power loss prediction and precise modeling of magnetic powder components in DC-DC power converter application [J]. IEEE Transactions on Power Electronics, 2015, 30(4): 2232-2237.

[67] Van den Bossche A P, Valchev V C, Van de Sype D, et all. Ferrite losses with square wave voltage and dc bias [J]. Journal of Applied Physics, 2006,99:08M908.

[68] Basso V, Bertotti G, Bottauscio O, et all. Power losses in magnetic laminations with hysteresis: finite element modeling and experimental validation [J]. Journal of Applied Physics, 1997, 81(8):5606-5608.

[69] Ragusa C and Fiorillo F. A three-phase single sheet tester with digital control of flux loci based on the contraction mapping principle [J]. Journal of Magnetism and Magnetic Materials, 2006, 304: e568-e570.

[70] Fiorillo F, Beatrice C, Bottauscio O, et all. Eddy current losses in Mn-Zn ferrites [J]. IEEE Transactions on Magnetics, 2014, 50(1): 6300109.

[71] Beatrice C, Dobák S, Ferrara E, et all. Broadband magnetic losses of nanocrystalline ribbons and powder cores [J]. Journal of Magnetism and Magnetic Materials, 2016, 420:317-323.

[72] Beatrice C, Tsakaloudi V, Dobák S, et all, Magnetic losses versus sintering treatment in Mn-Zn ferrites [J]. Journal of Magnetism and Magnetic Materials, 2017, 429:129-137.

[73] Magni A, Beatrice C, Bottauuscio O, et all. Magnetization process in thin laminations up to 1 GHz [J]. IEEE Transactions on Magnetics, 2012, 48(4):1363-1366.

[74] Seemann K, Leiste H, and Bekker V. New theoretical approach to the RF-dynamics of soft magnetic FeTaN films for CMOS components [J]. Journal of Magnetism and Magnetic Materials, 2004, 278:200-207.

[75] Bottauscio O, Fiorillo F, Beatrice C, et all. Modeling high-frequency magnetic losses in transverse anisotropy amorphous ribbons [J]. IEEE Transactions on Magnetics, 2015, 51(3):2800304.

[76] O. de la Barrière, C. Ragusa, C. Appino, and F. Fiorillo, "Prediction of energy losses in soft magnetic materials under arbitrary Induction waveforms and DC bias," IEEE Trans. Ind. Electron., vol. 64, no. 3, pp. 2522-2529, March 2017. doi: 10.1109/TIE.2016.2608886.

[77] Ossart F, Hug E, Hubert O, et all. Effect of punching on electrical steels: experimental andnumerical coupled analysis [J]. IEEE Transactions on Magnetics, 2000, 36:3137–3140.

[78] Nakata T, Nakano M and Kawahara K. Effects of stress due to cutting on magnetic characteristics of silicon steels [J]. IEEE Translation Journal on Magnetics in Japan, 1992, 7:1453–457.

[79] Baudouin P, De Wulf M, Kestens L and et all. The effect of guillotine clearance on the magnetic properties ofelectrical steels [J]. Journal of Magnetism and Magnetic Materials, 2003, 256:32–40

[80] Maurel V, Ossart F and Billardon R. Residual stress in punched laminations: phenomenological analysis and influenceon the magnetic behavior of electrical steels [J]. Journal of Applied Physics, 2003, 93: 7106–7108.

[81] Gmyrek Z, Cavagnino A and Ferraris L. Estimation of the magnetic properties of the damaged area resulting fromthe punching process: experimental research and FEM modeling [J]. IEEE Transactions on Industry Applications, 2013, 49:2069–207.

[82] Hofman M, Naumoski H, Herr U and et all. Magnetic properties of electrical steel sheets in respect of cutting: micromagnetic analysis and macromagnetic modeling [J]. IEEE Transactions on Magnetics, 2016, 52:2000114.

[83]蔡祖光. 磨料水射流切割技术及其应用[J]. 液压与气动, 2000, 02:5-8.

[84] Petrun M, Steentjes S, Hameyer K and et all. Modeling the influence of varying magnetic properties in softmagnetic materials on the hysteresis shape using the flux tube approach [J]. Journal of Applied Physics, 2015, 117:17A708.

[85] Steentjes S, von Pfingsten G and Hameyer K. An application-oriented approach for consideration of material degradation effects due to cutting on iron losses and magnetizability [J]. IEEE Transactions on Magnetics, 2014, 50:027804.

[86] Kedous-Lebouc A, Messal O and Youmssi A. Joint punching and frequency effects on practical magnetic characteristics of electrical steels for high-speed machines [J]. Journal of Magnetism and Magnetic Materials, 2017, 426 : 658–665.